NOTE TO USERS

This reproduction is the best copy available.

UMI®

AN INTERFEROMETRIC STUDY OF FREE CONVECTIVE HEAT TRANSFER IN A DOUBLE GLAZED WINDOW WITH A BETWEEN-PANES VENETIAN BLIND

by

Bertha Lai

B.Eng., Ryerson University, 2002

A thesis

presented to Ryerson University

in partial fulfillment of the

requirements for the degree of

Master of Applied Science

in the Program of

Mechanical Engineering

Toronto, Ontario, Canada, 2004

Borrower

Ryerson University requires the signatures of all persons using or photocopying this thesis. Please sign below, and give address and date.

Abstract

AN INTERFEROMETRIC STUDY OF FREE CONVECTIVE HEAT TRANSFER IN A DOUBLE GLAZED WINDOW WITH A BETWEEN-PANES VENETIAN BLIND

Bertha Lai

Master of Applied Science, 2004
Program of Mechanical Engineering, Ryerson University

The free convective heat transfer in a double-glazed window with between-panes Venetian blinds was measured using a Mach-Zehnder interferometer. A vertical cavity with differentially heated/cooled flat plates was set up with an internal blind at slat angles of $\phi = 0°$, $\phi = 45°$, and $\phi = 90°$ from the horizontal and tip-to-plate spacings of $s = 2$mm, $s = 4$mm, and $s = 8$mm. Heat transfer measurements were taken with air as the test fluid and at Rayleigh numbers of $Ra \approx 4.5\times10^4$, $Ra \approx 6.7\times10^4$, and $Ra \approx 13.1\times10^4$, based on cavity widths of $W = 28.7$mm, $W = 32.7$mm, and $W = 40.7$mm, respectively. Finite fringe interferograms were used to obtain local and average heat transfer data. Infinite fringe interferograms were taken to visualize the temperature field within the cavity. A preliminary numerical study of the experimental geometry was also conducted. The results show that there was substantial variation in local heat transfer rates caused by the presence of the between-panes blind inside the window cavity. In general, experimental average Nusselt numbers were found to be lower than those of a cavity without blinds.

Acknowledgements

The author would like to acknowledge Dr. D. Naylor for his invaluable advice and continuous guidance throughout the project that showed the way to its successful completion.

The author would also like to acknowledge the support of the Natural Sciences and Engineering Research Council of Canada.

The author is most grateful to Alan Machin for his time and assistance in building the experimental model and setting up equipment for the Laser Interferometry lab. The wonderful help provided by the Engineering Support staff, especially Joseph Amenkrah, is also greatly appreciated.

Last but not least, the author wishes to thank her family and friends who have given ongoing support and encouragement. The author especially thanks Karlick for his love and understanding during the course of this thesis.

Table of Contents

List of Tables

List of Figures

Nomenclature

A	aspect ratio
a	amplitude of light [m]
b	nominal blind-to-plate spacing
c	speed of light [m/s]
C_p	specific heat [J/kg·K]
d	pin and gauge block distance [mm]
g	gravitational acceleration [m/s^2]
G	Gladstone-Dale constant [m^3/kg]
Gr	Grashof number
h_y	local convective coefficient [W/m^2·K]
k	thermal conductivity [W/m·K]
L	vertical height of the cavity [m]
n	index of refraction
Nu_{avg}	average Nusselt number
Nu_y	local Nusselt number
p	pressure [Pa]
Pr	Prandtl number
R	ideal gas constant [J/kg·K]
Ra	Rayleigh number based on cavity width
s	blind tip-to-plate spacing
SF	scale factor
T	temperature [K]
u, v	velocity components [m/s]
U, V	dimensionless velocity components
W	width of the cavity [m]
x	fringe distance [mm]
X, Y	dimensionless co-ordinates
Z	optical length of plate [m]

Greek

α	thermal diffusivity [m^2/s]
β	volumetric expansion coefficient [K^{-1}]
ε	fringe shift order
ε_p	surface paint emissivity
$\Delta\varepsilon$	fringe shift [mm]

θ	dimensionless temperature
λ	wavelength [m]
μ	dynamic viscosity [N·s/m^2]
v	kinematic viscosity [m^2/s]
ρ	density [kg/m^3]
ϕ	blind slat angle

Subscripts

actual	actual value
c	value for cold plate
f	value evaluated at film temperature
h	value for hot plate
o	initial value
photo	value taken from interferogram
pin	value for the pin
ref	value for the reference beam
s	value for the surface of the plate
test	value for the test beam
∞	value for the ambient

Abbreviations

BS	beam splitter
CFD	computational fluid dynamics
CSA	Canadian Standards Association
DA	data acquisition
FEHT	Finite Element Heat Transfer
IGU	insulated glazing unit
LTP	linear temperature profile
M	flat mirror
MZI	Mach-Zehnder interferometer
NFRC	National Fenestration Rating Council
SHG	solar heat gain
ZHF	zero heat flux

Chapter 1

GENERAL REVIEW

1.1 Introduction

Heat transfer through windows and other fenestration systems is receiving escalating attention from researchers as people become increasingly aware of the importance of energy efficiency. In most building structures, substantial amounts of heat gain in the summer and heat loss in the winter through windows add to energy consumption and undesirable costs. For this reason, the double-glazed window has been used extensively for the insulating effects provided by its air-filled cavity.

The design of windows is aided by the wide use of commercial simulation software in North America. VISION [1] is used by the Canadian Standards Association (CSA), while WINDOW [2] is used by the National Fenestration Rating Council (NFRC). These programs have been developed to examine one-dimensional heat transfer for a variety of glazing systems and environmental conditions, and provide users with the centre-glass U-value and solar heat gain (SHG) coefficient.

Shading devices, such as Venetian blinds, are commonly placed near windows to act as a screen from direct sunlight, improve thermal performance, provide privacy, as well as for aesthetics and other benefits. Although the effect of these shading devices on a window performance is a subject of interest for many researchers, no correlations are currently available to predict the heat transfer results for these problems. Consequently, neither VISION nor WINDOW is able to include shading devices in their calculations.

The current study is part of an ongoing effort to understand the thermal interaction between a window and a blind. The focus of the present work is on a between-panes louvered blind. Several window companies offer this contemporary design in which the blind is located between the glass panes inside the enclosed cavity of a double-glazed window. This conveniently keeps the blind away from tampering and dust, and with the control mechanism hidden in the frame, eliminates the unwanted strings and cords for a more pleasing appearance.

One particular company claims these between-panes blinds can significantly improve the thermal performance of a window by lowering its U-value and SHG coefficient. However, the company states that this is only for the case when the blind is in the closed position, based on the fact that solar transmission is reduced. Nonetheless, to understand the overall effect of between-panes blind on the thermal performance of a double-glazed window, it is necessary to also consider the conductive characteristic of the blind when it is fully open, and variations it may cause to the convective flow inside the air space.

The current study is an experimental analysis of the natural convective heat transfer within a double-glazed window containing a set of internal Venetian blinds. Classical interferometry is used to visualize and measure the variations in the thermal field across the window cavity in the presence of between-panes blind. A preliminary numerical study is also presented, which is used to aid in the design of the experimental model and interpretation of the results.

1.2 Literature Review

The geometry of a double-glazed window is essentially a vertical cavity. The heat transfer problem of free convection in a vertical cavity forms the basis for the present study, and a brief summary of related literature is given. A review of the published investigations involving Venetian blinds is also provided.

1.2.1 Free Convection in Vertical Cavity

The typical double-glazed window consists of two panes of glass separated by an edge-spacer at the top and bottom. The sealed slot is usually filled with air or other types of gases and acts as an insulating layer between the indoor and outdoor surfaces. The difference in temperature between the glazings drives the fluid into a circulating flow. The thermal performance of a double-glazed window is strongly dependent on the convective heat transfer inside the enclosure. This phenomenon may be reduced to the simplified model of free convection in a vertical cavity.

The topic of natural convection in tall, rectangular cavities has been extensively researched for the past century. As shown in Figure 1.1, the geometry in these studies assumes uniform temperatures on the vertical walls, and the horizontal end walls are treated as having either a zero heat flux (ZHF) or a linear temperature profile (LTP). The convection of fluid inside the cavity is driven by buoyancy, which causes an upward flow near the hot wall and a downward flow near the cold wall. This heat transfer problem has

many practical applications, including insulating cavity walls and double-glazed windows.

Clearly, the classical cavity model cannot perfectly mimic the complexity of a commercial double-glazed window, as there are temperature variations on the glazings especially in the edge-glass region, as well as end losses that occur at the edge-spacers. Nevertheless, it is worthwhile to go through the major theoretical, experimental, and numerical studies and note the fundamental findings pertaining to this topic. For more detailed reviews, the reader is referred to Ostrach [3], and Wright and Sullivan [4].

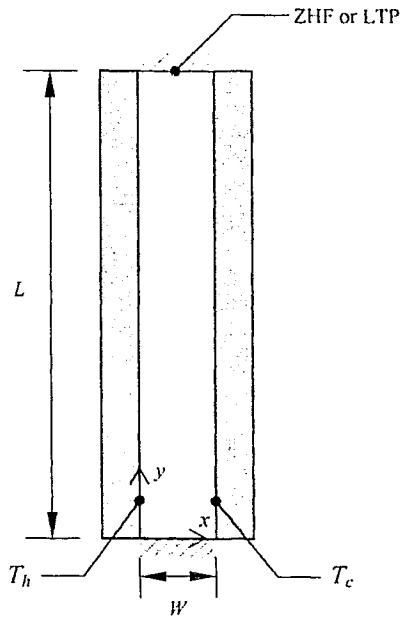

Figure 1.1 Tall rectangular cavity geometry

It has been found that the solution to this heat transfer problem, the Nusselt number ($Nu = hW/k$), is a function of the Rayleigh number ($Ra = Pr \cdot g\beta\Delta TW^3\rho^2/\mu^2$) and the aspect ratio ($A = L/W$) of the cavity. Of course, these parameters are directly related to variables such as length (L) and width (W) of the cavity, temperature difference across the cavity ($\Delta T = T_h - T_c$), and Prandtl number ($Pr = \mu C_p/k$) of the fluid, that affect the type of flow, flow regimes, and instability in the flow. Heat transfer correlations that are found in the literature were often given in the form of:

$$Nu = cRa^m A^n \tag{1.1}$$

The laminar free convection was first defined separately into conduction and boundary layer regimes by Batchelor [5]. Using a Mach-Zehnder interferometer (MZI) to obtain local heat transfer results, Eckert and Carlson [6] refined Batchelor's work by proposing conduction, transition, and boundary layer regimes. The conduction regime occurs when the temperature difference is small ($Ra < 10^3$). A weak unicellular flow of fluid traveling up the hot wall and down the cold wall exists, and heat transfer across the cavity is primarily due to conduction between the counter-flowing streams, resulting in a linear temperature profile ($Nu = 1$). As the temperature difference increases ($10^4 < Ra < 10^5$), the flow strengthens and develops into boundary layers on the vertical walls, separated by a core region. Higher horizontal temperature gradients exist at the walls due to the convection in the boundary layers than in the core region, where only a small degree of conduction takes place. This is the boundary layer regime, with higher heat transfer rates ($Nu > 1$). In-between the conduction and boundary layer regimes is the transition regime. Heat transfer is the combination of convection in the boundary layers and conduction across the core region. The critical value of Ra at which flow leaves the

conduction regime is a function of the enclosure aspect ratio, A. It is noted that a vertical temperature gradient in the core region was also observed once the flow leaves the conduction regime.

In addition to the interferometric work by Eckert and Carlson [6], numerous experimental studies have been conducted to obtain visualization and heat transfer data, which were used to gain insight on the fluid flows. Elder took streak photographs using particles suspended in water to observe streamlines of laminar [7] and turbulent [8] flows. He discovered a multicellular flow pattern in the core region. This secondary flow created instability in the conduction and boundary layer regimes which was observed in the streak photographs by Vest and Arpaci [9] and Seki et al. [10]. Yin et al. [11] made temperature profile measurements for a wide range of Ra and further define the flow regimes.

Other experimental studies, like Randall et al. [13], ElSherbiny et al. [14, 15], Shewen et al. [16], have included heat transfer correlations. In particular, ElSherbiny et al. [14] proposed the following well-established correlation:

$$Nu_1 = 0.0605 Ra^{1/3} \tag{1.2.1}$$

$$Nu_2 = \left[1 + \left(\frac{0.104 Ra^{0.293}}{1 + \left(\frac{6310}{Ra}\right)^{1.36}}\right)^3\right]^{1/3} \tag{1.2.2}$$

$$Nu_3 = 0.242\left(\frac{Ra}{A}\right)^{0.272} \tag{1.2.3}$$

$$Nu = \mathrm{Max}\left(Nu_1, Nu_2, Nu_3\right) \tag{1.2.4}$$

The correlation is based on experiments carried out over wide ranges of Ra and A.

Earlier theoretical study was performed by Gill [17], who obtained an approximate solution for the boundary layer flow that agreed with Elder's experimental results. Improvements on Gill's theory were later made by Bejan [18]. The work of Raithby et al. [19] produced solutions for various flow regimes and found even better agreement with existing experimental data. More recent analysis of Zenouzi and Yener [20] included the effect of radiation on the natural convection problem.

An abundance of numerical studies exists in the literature, modeling fluid motion inside a cavity with either ZHF or LTP boundary conditions. Amongst them are the papers by Newell and Schmidt [21], Bergholz [22], Jones [23], Raithby and Wong [24], Lee and Korpela [25], Chait and Korpela [26], Ramanan and Korpela [27], and Jin and Chen [28, 29]. The numerical solutions were able to compute instability in the flow, and streamline plots of the multicellular flow pattern were generated. Attempts were made to predict the onset of secondary cells at differing critical Rayleigh numbers (Ra_c).

Few studies are available which are directly related to the heat transfer through a double-glazed window. Korpela et al. [30] used the finite difference method to calculate average and local Nusselt numbers and suggested a formula for window spacings. A finite element model was used by Curcija and Goss [31] to study the natural convection in an insulated glazing unit (IGU) coupled with radiative and conductive heat transfer. Window U-values were calculated. Wright and Sullivan [32, 33] developed a numerical model to examine natural convection in a window cavity, which formed the basic model for many subsequent window studies. Finally, Wright [34] developed a new correlation based on the ones presented by ElSherbiny et al. [14] and Shewen et al. [16] that is valid for a variety of window applications.

1.2.2 Venetian Blind Studies

In recent years, many research studies have emerged regarding the effect of Venetian blinds on window performance. Some important experimental and numerical investigations were carried out as part of a collaborative effort to generate valuable information that will be used to develop VISION, so that Venetian blinds and other shading devices can be modeled in the code. The major works are discussed below.

The first and most prominent work is the experimental study by Machin [35]. He used an MZI to obtain interferograms and heat transfer data for an isothermal heated flat plate adjacent to a Venetian blind, and took flow visualization photographs as well. The geometry and procedure of this experiment [36] became the standard for other interferometric studies, including the present one. Following Machin's experimental work, Ye [37] worked on a finite element solution to numerically study the effect of Venetian blinds on heat transfer in various glazing units, such as internal blind in an IGU. Later, Phillips [38] developed a full-scaled finite element model to solve Machin's heat transfer problem. The numerical results were in close agreement with the experimental data. Originally, Phillips et al. [39] used a conjugate conduction/convection model and found that radiation is a significant factor. Based on this finding, a conjugate conduction/ convection/radiation model was created [40]. Again, using the MZI, Duarte [41] performed an experimental study of free convection from a heated vertical plate in the presence of heated Venetian blind to simulate solar irradiance. As part of this experiment, Naylor and Duarte [42] formulated the direct temperature gradient method to measure low convective heat transfer rates using interferometry.

Other works are the ones by Collins et al. [43, 44, 45] where they conducted an interferometric study [43] of convective heat transfer from an isothermal surface adjacent to a heated Venetian blind, carried out a numerical analysis [44] on the experimental problem and then validated the results [45] against the experimental data. Oosthuizen et al. [46, 47] examined the effect of vertical blind on heat transfer from a window in a numerical study. In the most recent studies by Shahid and Naylor [48, 49], the work of Phillips was extended and a conjugate conduction/convection/radiation finite volume model of a complete fenestration, i.e., single-glazed and double-glazed windows with horizontal Venetian blinds, was developed. The numerical model was validated with the results from Machin [35] and Phillips [38].

Several studies are found to be somewhat related to the current research, and shall be mentioned here. The numerical studies by Kelkar and Patankar [50] and Mezrhab and Bchir [51] both addressed the natural convection in partitioned cavities. Smith et al. [52] presented a numerical model that simulates a double-glazed window with various features, including between-panes vertical and horizontal partitions. Fang [53] experimentally studied the U-value of single-glazed and double-glazed windows with a long-wave high-reflectivity Venetian blind.

Surprisingly, more than a few papers were discovered in the literature to have studied the effect of between-panes Venetian blinds. Using a guarded-heater-plate apparatus, Garnet et al. [54] performed an experiment to determine centre-glass U-values of a window with internal blind, with attention on the effect of blade angle. Rheault and Bilgen [55] theoretically studied the automated Venetian blind window system. With the louvers modeled as rotating flat surfaces with no curvature, a detailed radiative exchange

analysis was carried out. They found a significant reduction in solar heat load at optimal louver angles. The numerical study by Zhang et al. [56] focused on the insulating effect of the cavity with the blind at the closed position. The slats were modeled as overlaying strips, again with no curvature, with a small spacing between overlaps for air leakage. It was determined that this permeable screen improves the insulating capability of the cavity by inhibiting the convective heat transfer rate. In Korea, Cho et al. [57] conducted a study on the heating and cooling loads of a typical building. Similar to Rheault and Bilgen's conclusion, they reported that, by varying the slat angle, the use of between-panes Venetian blinds helps control solar gains. Using a goniospectrometer, Breitenbach et al. [58] measured the solar energy transmittance for a range of incidence angles at different blind slat angles. After neglecting to model slat curvature, they realized that the spatial distribution of light is strongly influenced by the shape of the slats.

The latest study was by Naylor and Collins [59], who developed a two-dimensional finite volume model to calculate heat transfer in a window with between-panes Venetian blind. A "Simplified Model", which combines the data from a conjugate conduction/convection CFD model with a simple radiation model, was evaluated against a conjugate conduction/convection/radiation "Full CFD Model". The "Simplified Model" closely predicted the window U-value predicted by the "Full CFD Model". This study shows that, for most purposes, thermal radiation can be decoupled from the CFD calculations. The "Simplified Model" may be used to estimate U-value with less computational requirements, while still accounting the effect of radiation.

1.3 Scope of Research

As the development of more sophisticated analysis programs for fenestration systems continues, researchers need to carry out a variety of experimental and numerical heat transfer studies. Some integral topics include, for example, complex glazing configurations and the influence of adjacent shading devices. There is a call for future software releases to incorporate shading devices like the Venetian blind when calculating window performance. With increasing popularity of the between-panes Venetian blinds, the thermal performance of this geometry is of major engineering interest.

The objective of the present research is to determine the effect of blind slat angle (ϕ) and blind tip to window surface spacing (s) on the free convective heat transfer in a double-glazed window with a between-panes Venetian blind. A sketch of the test geometry is shown in Figure 1.2. A Mach-Zehnder interferometer will be used to visualize the natural convection flow inside the window cavity and to measure the heat transfer rates on the hot and cold surfaces. The experimental results are intended to be used primarily for the validation of future numerical models being developed in a joint project by Ryerson University, Queen's University, and the University of Waterloo.

As part of a preliminary study, a basic numerical solution will be obtained for the free convection in the test geometry. The numerical results are intended to simulate the conditions of the present experiment and provide an estimation of the heat transfer results.

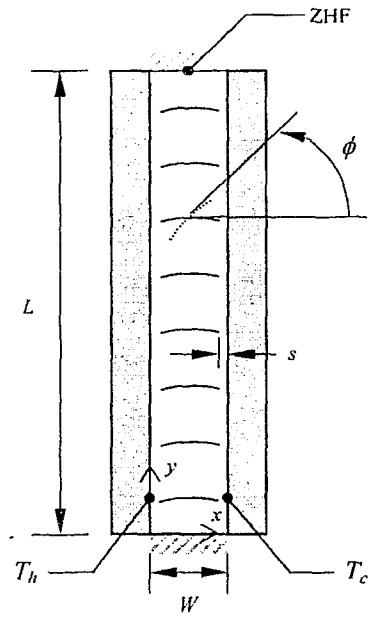

Figure 1.2 Experimental test geometry

Chapter 2

EXPERIMENTAL APPARATUS

2.1 Introduction

There are many types of optical techniques used for heat transfer studies [60]. The present experiment was carried out with a Mach-Zehnder interferometer (MZI). The method of laser interferometry provided visualization of the temperature field from which local temperature measurements and heat transfer data could be obtained.

The theory and technique of classical interferometry using a Mach-Zehnder interferometer has been described in reference [61]. This system is particularly advantageous because of the large displacement of the test beam from the reference beam, allowing for high quality and accurate interference. It is non-intrusive to either the temperature or the flow, giving full-field measurements with no disturbance. There is no thermal inertia, permitting real time visualization and measurements.

There are some limitations with the MZI. Interferometry is ideal for measurements of two-dimensional temperature fields, and is difficult to apply to turbulent flow. The test fluid must be transparent to laser light, which is air in this case. Because of the sensitivity of the system, the working environment has to be clean and have very low vibration levels. The interferometer consists of expensive and extremely delicate optics, which requires careful handling and proper set up by a skilled operator.

The reader is referred to more comprehensive studies on the theory of interferometry [60] and other optical techniques [62].

2.2 Interferometer

The Mach-Zehnder interferometer is used to measure and visualize the free convective temperature field of the window cavity. The test fluid in the study is air, which is suitable for this application since it is homogeneous and transparent to radiation so that only the convective heat transfer component is measured. Air can also be considered as an ideal gas, relating the temperature field directly to the density field.

The Ryerson Mach-Zehnder interferometer was constructed by Von Bistram in 1994, based on Tarasuk's design [63] and the interferometer at the University of Western Ontario. Further details can be found in Von Bistram's thesis [64] at Ryerson University.

The schematic diagram in Figure 2.1 shows the typical layout of the Ryerson Mach-Zehnder interferometer. The light source is a 15 mW Helium-Neon laser, which produces monochromatic light at a wavelength of $\lambda = 6.328\times10^{-7}$ m. The beam first passes through a spatial filter that filters and expands the beam onto a parabolic mirror, generating a collimated beam with a diameter of about 20 cm. It then strikes the first beam splitter (BS1), where it is separated into the reference beam and test beam. These two beams are perfectly in phase and have approximately the same intensity. The test beam and reference beam are reflected off two flat mirrors (M1 and M2, respectively). The reference beam travels through ambient air at room temperature, while the test beam passes through the experimental model, in this case the window cavity. The air in the cavity is at various temperatures different than the ambient air temperature, which changes its index of refraction. This causes the light passing through ambient air and the light passing by the model to travel at different speeds. The two beams, which are now

out of phase with each other, are recombined at the second beam splitter (BS2). The output beam shows the pattern of constructive and destructive interference and can be recorded as interferograms. A spherical mirror focuses the beam onto a small mirror which reflects the image back for recording by a camera.

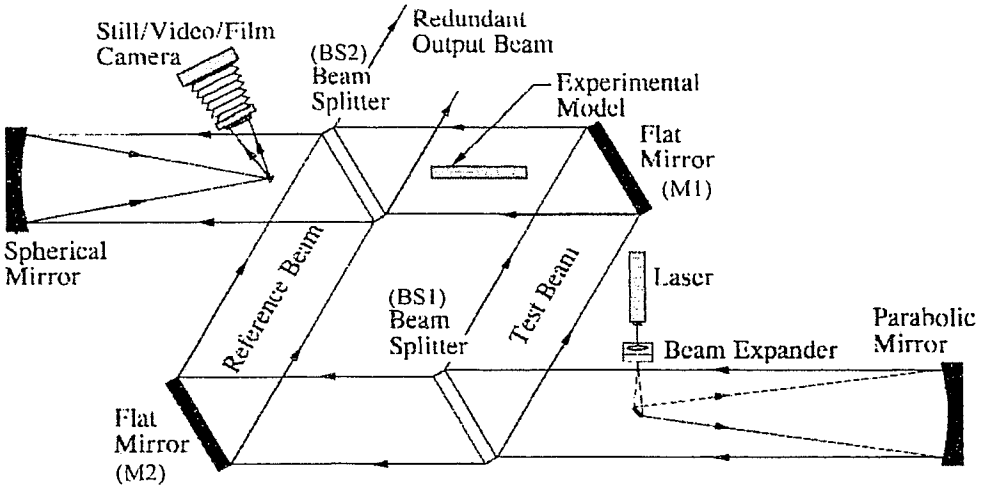

Figure 2.1 Typical layout of the Ryerson Mach-Zehnder interferometer

The interferometer was mounted on an optical bench manufactured by Newport Corporation, 1.205m × 3.03m (4' × 10') with 1/4-20 NC tapped holes equally spaced on 25.4mm (1") centres. The bench was placed on eight inner tubes to reduce vibrations. Some of the optics were cantilevered on 9.525mm (3/8") steel plates off one side of the bench in order to accommodate the experimental model. The apparatus was put inside a 3.66m × 6.10m × 2.44m (12' × 20' × 8') enclosure to reduce air currents and exterior light.

2.3 Test Section

The test section was a vertical cavity consisting of two isothermal flat plates separated by spacers at the top and bottom ends. A set of seventeen blind slats were situated at the centre of the cavity on support posts that were mounted onto the spacers. The entire model had an overall height, width, and depth of 393.7mm × 215.9mm × 355.6mm (15-1/2" × 8-1/2" × 14"), respectively. A photo of the test model with the Ryerson Mach-Zehnder interferometer is given in Figure 2.2.

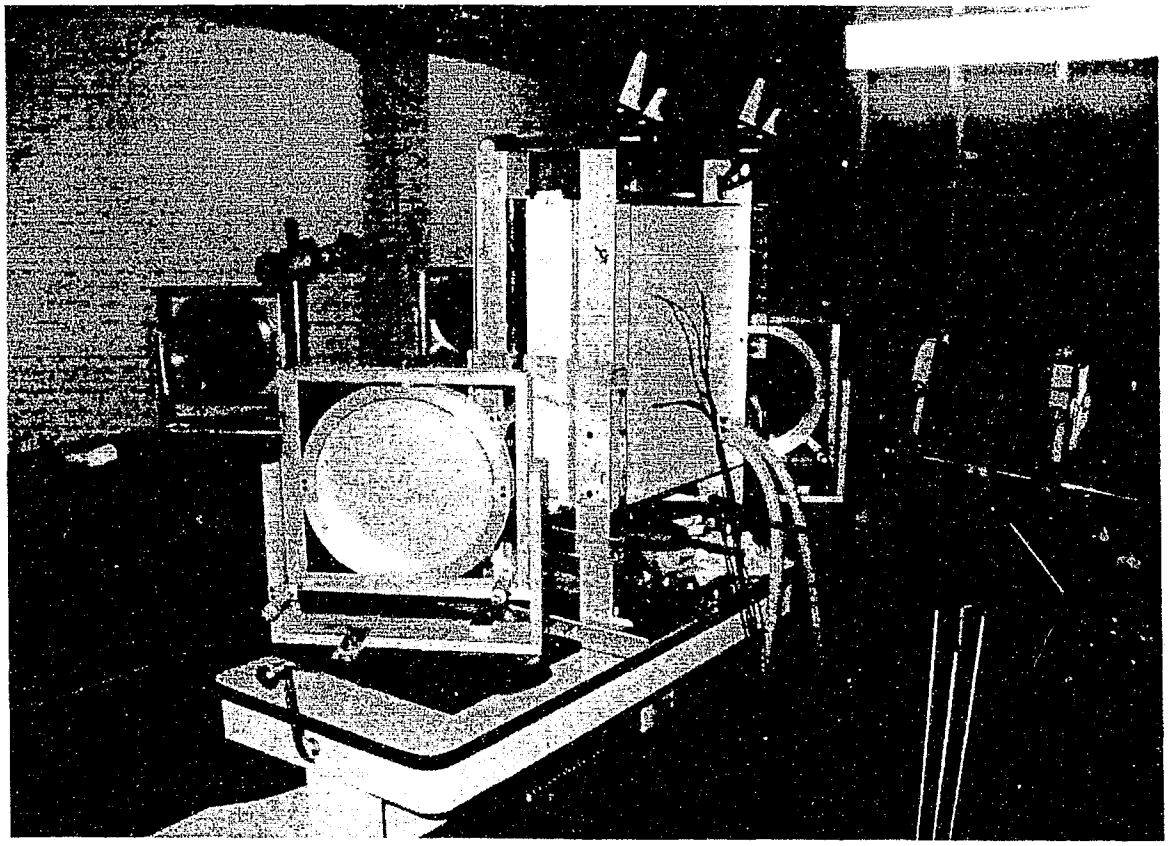

Figure 2.2 Photograph of Test Model with Ryerson MZI

2.3.1 Hot Isothermal Flat Plate

Figure 2.3 shows a mechanical drawing of the hot plate. The size of the plate was chosen based on the considerations discussed in Machin's thesis [35]. The 12.7mm (1/2″) thick aluminum plate had a width of 355.6mm (14″), corresponding to approximately nine fringes in the infinite fringe mode for a 20°C temperature difference across the cavity (2.2°C per fringe).

The height of the plate was 393.7mm (15-1/2″), which was based on the original height of 380mm (15″) selected by Machin [35]. The extra height was added to fit the end spacers while still holding the same number of blind slats as Machin's model. It was decided that three composite interferograms would be necessary in order the study the entire cavity from top to bottom.

The aluminum plate was machined to its exact dimensions on the Ryerson CNC milling machine. The front surface of the plate was milled in the beam direction to a flatness of within ±0.12mm. The improved flatness makes the alignment of the test beam with the model more accurate, hence yielding better results. Also for alignment purposes, twelve holes were drilled at precise locations for dowel pins (Spaenaur Inc. 238-277). The surface was then spray-painted with an enamel paint that has a known emissivity of $\varepsilon_p = 0.81 \pm 0.02$, measured at the University of Waterloo using an infrared reflectometer. This is close to the emissivity of untreated window glass.

The hot plate had to be heated to temperature T_s above the ambient temperature T_∞. This was done by six electric strip heaters adhered to the back surface to deliver the desired amount of heat evenly throughout the front surface. Based on the plate

configuration and the heat loss calculations according to manufacturing specifications, it was determined that a total power of 14.8W was required. The chosen heaters (Minco Products Inc. model HK 5426 R8.3 L36 B) were Kapton insulated self-adhesive heaters in the size of 51mm × 178mm (2" × 7") with a resistance of 8.3Ω, accurate to ±10%. The heaters were arranged in three rows with two heaters side by side covering the entire width of the plate in each row. The three heaters on each side were connected in series and the two sides connected in parallel, with a total resistance of 12.45Ω.

The temperature of the plate was measured by eight thermocouples strategically placed at various locations on the back of the plate. Holes were drilled into the back surface of the plate such that the thermocouple tips were within 2mm below the front surface. The type of thermocouple used (Omega Engineering Inc. type TT-T-24-SLE) was high performance Teflon-coated 24 gauge type T (copper-constantan), which has a deviation of 0.4°F at 200.2°F. The thermocouples were calibrated in an isothermal bath against a precision thermometer calibrated against national standards (see Appendix B). The thermocouples were connected to a data acquisition (DA) system where the ambient and plate temperatures were monitored. For all experiments, the plate was isothermal to within 0.6 °C, which was 3% of the overall temperature difference ($\Delta T \approx 20$°C).

On the back surface of the plate, there were sixteen 1/4-20 blind tapped holes for mounting. The back side of the plate was insulated by a layer of 25.4mm (1") thick polystyrene and 12.7mm (1/2") thick plywood, secured into these holes with nylon threaded rods and nuts. The plate assembly was supported on aluminum angle brackets and mounted onto the base plate. The complete model assembly shall be discussed in Section 2.3.4.

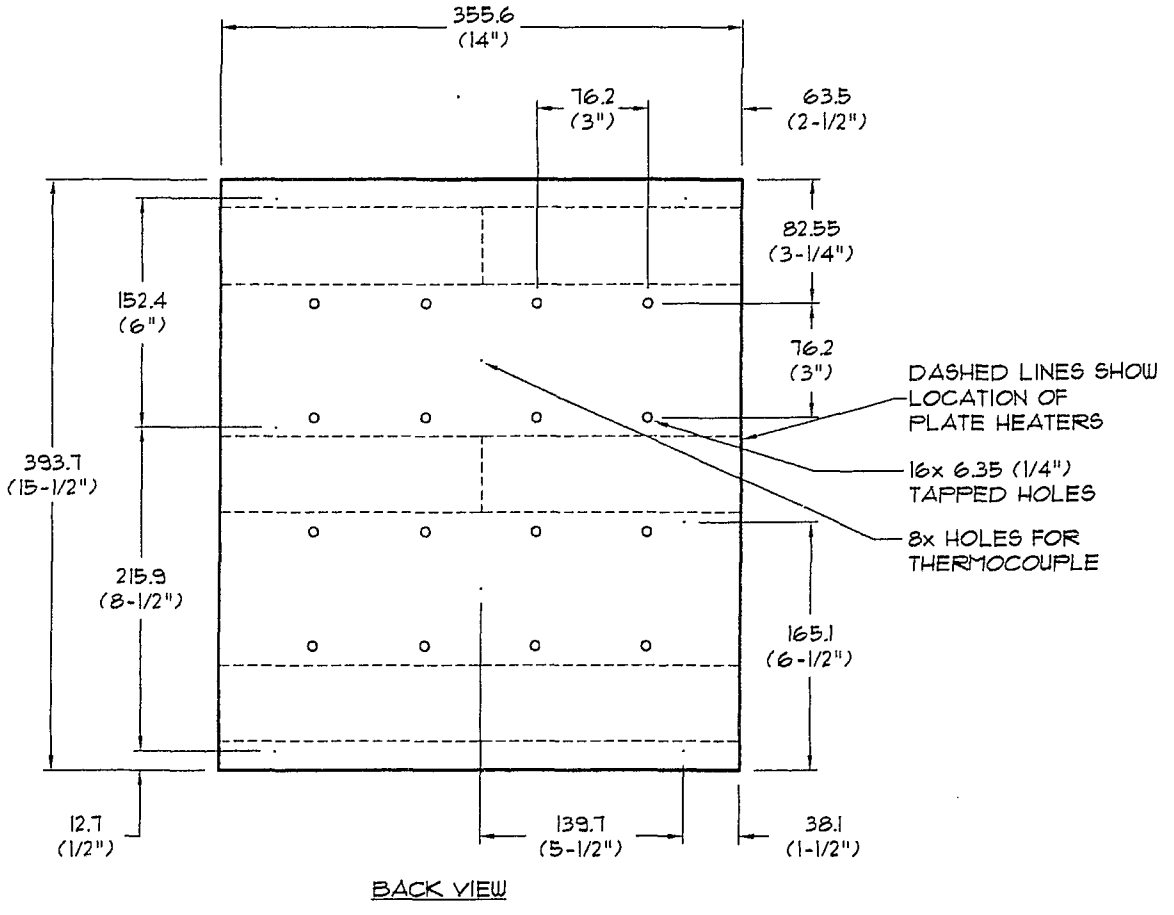

NOTE:

1. ALUMINUM PLATE SHALL BE 12.7 (1/2") THICK.

Figure 2.3 Mechanical drawing of the hot plate

2.3.2 Cold Isothermal Flat Plate

The cold plate used in the test section was manufactured from two different sheets of aluminum. The top sheet had a thickness of 19.05mm (3/4″), with flow channels milled into its back surface. The 6.35mm (1/4″) thick backing sheet served to close the flow channels. Mechanical drawings of the top and backing sheets are shown in Figures 2.4 and 2.5. The size of the assembled cold plate was 25.4mm (1″) thick, with the same height and width as the hot plate of 393.7mm × 355.6mm (15-1/2″ × 14").

The cold plate was cooled to a constant temperature using a precision temperature bath. Cold water was pumped through a 12.7mm (1/2") flow channel milled into the back surface of the top sheet at a depth of 6.35mm (1/4"). The path of the flow channel was designed such that the inlet coils alongside the outlet towards the centre of the plate. This design promotes isothermal conditions within the plate. The front surface of the top sheet was treated the same way as the front surface hot plate described in Section 2.3.1.

A separate backing sheet was machined to seal the flow channel. A 3.5mm (0.139") diameter O-ring gasket was added to stop water leakage (Spaenaur Inc. 825-175). The backing sheet was fastened to the top sheet using thirty-two 5-40 screws around the perimeter of the plate. Since additional mounting holes cannot be drilled as they would interfere with the flow channel, the plate had to be mounted on the aluminum angle brackets with these same screws. The small size of these fasteners limited the weight of the plate assembly that can be supported, so it was decided that the polystyrene insulation and the plywood would not be attached on the back of the cold plate. A study was performed using the heat transfer software FEHT [65] to calculate the amount of heat

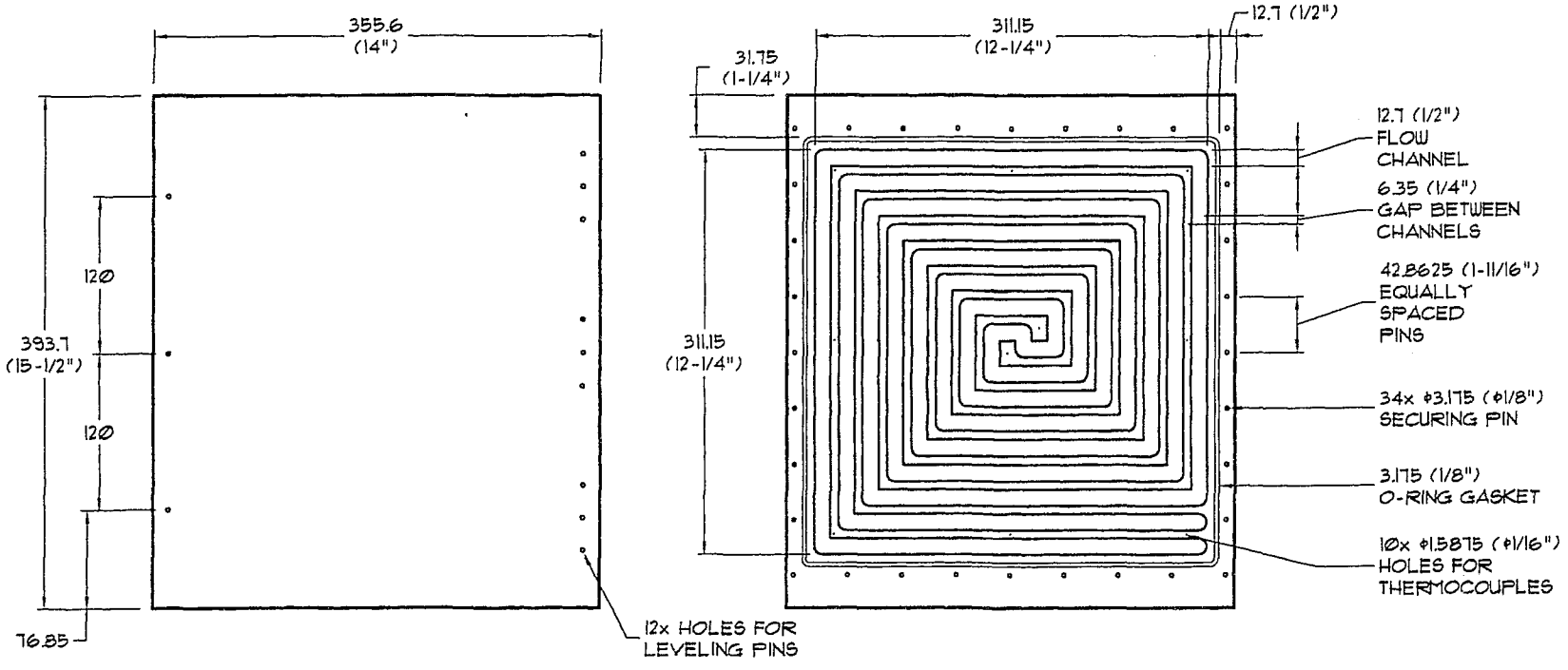

NOTE:

1. ALUMINUM PLATE SHALL BE 19.05 (3/4") THICK.
2. FRONT SURFACE OF PLATE SHALL BE PRECISION FLAT MILLED.
3. FLOW CHANNELS SHALL BE MILLED INTO BACK SURFACE AT DEPTH OF 6.35 (1/4").
4. HOLES FOR THERMOCOUPLES SHALL BE DRILLED INTO BACK SURFACE OF PLATE AT LOCATIONS INDICATED ON DRAWING #02. DEPTH OF HOLES SHALL BE 17.4625 (11/16").

Figure 2.4 Mechanical drawing of the cold plate's top sheet

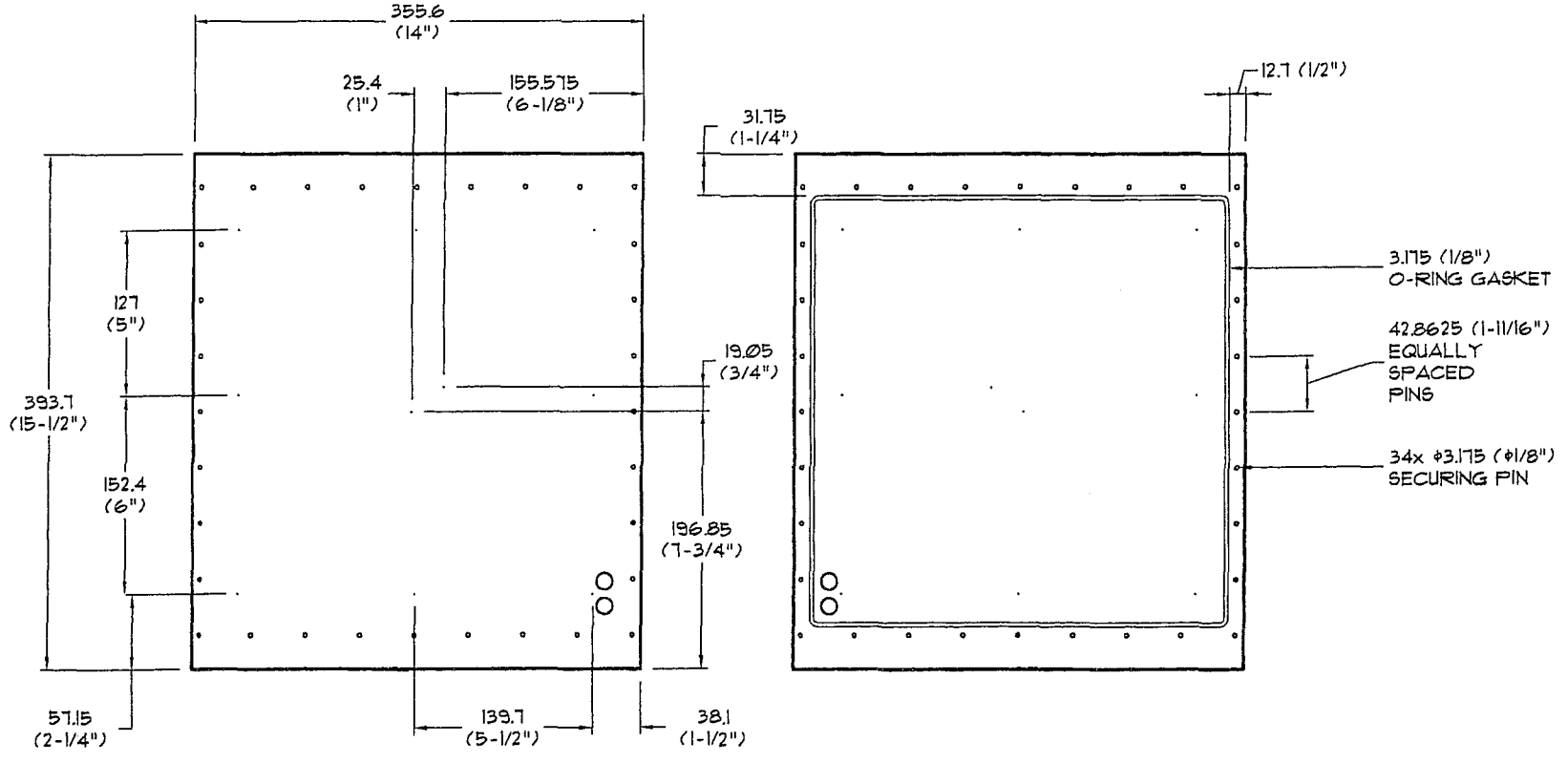

NOTE:

1. ALUMINUM BACKING PLATE SHALL BE 6.35 (1/4") THICK.

Figure 2.5 Mechanical drawing of the cold plate's backing sheet

gain from the ambient without the use of any insulation. The results confirmed that the lack of insulation causes a temperature change throughout the plate surface of less than ±0.02°C.

The temperature of the plate was measured by nine thermocouples inserted into holes precisely drilled all the way through the backing sheet to within 2mm of the front surface of the top sheet. The thermocouples, which were of the same type used in the hot plate, were connected to the same DA system as the hot plate.

2.3.3 Venetian Blind

The blind slats used in the experiment were taken from commercially available horizontal 1-inch aluminum Venetian blinds. The blind slat had a curved width of 25mm, a thickness of 0.16mm, and a radius of curvature of 50mm. Each of the seventeen slats was cut to the precise length of 342.9mm (13-1/2″) to fit the depth of the window cavity. The surfaces of all slats were painted with the same emissivity paint as the plate surfaces. The holding strings normally used for commercial louvers were eliminated as they would intrude into the interferometric output. Instead, they were replaced by a more precise and rigid support system, which is shown in Figure 2.6. The support posts were two 4.76mm (3/16″) square steel tubes precision machined with equally spaced holes to set the blind pitch at 22.2mm (7/8″). Each blind slat had a notch cut on either end with a custom-made jig. The slat were secured on nylon slotted set screws (Spaenaur Inc. 477-017) at the notches and mounted onto the posts with the screws, allowing the slat to pivot freely on its centerline. The use of this simple support system provided an easy yet accurate way

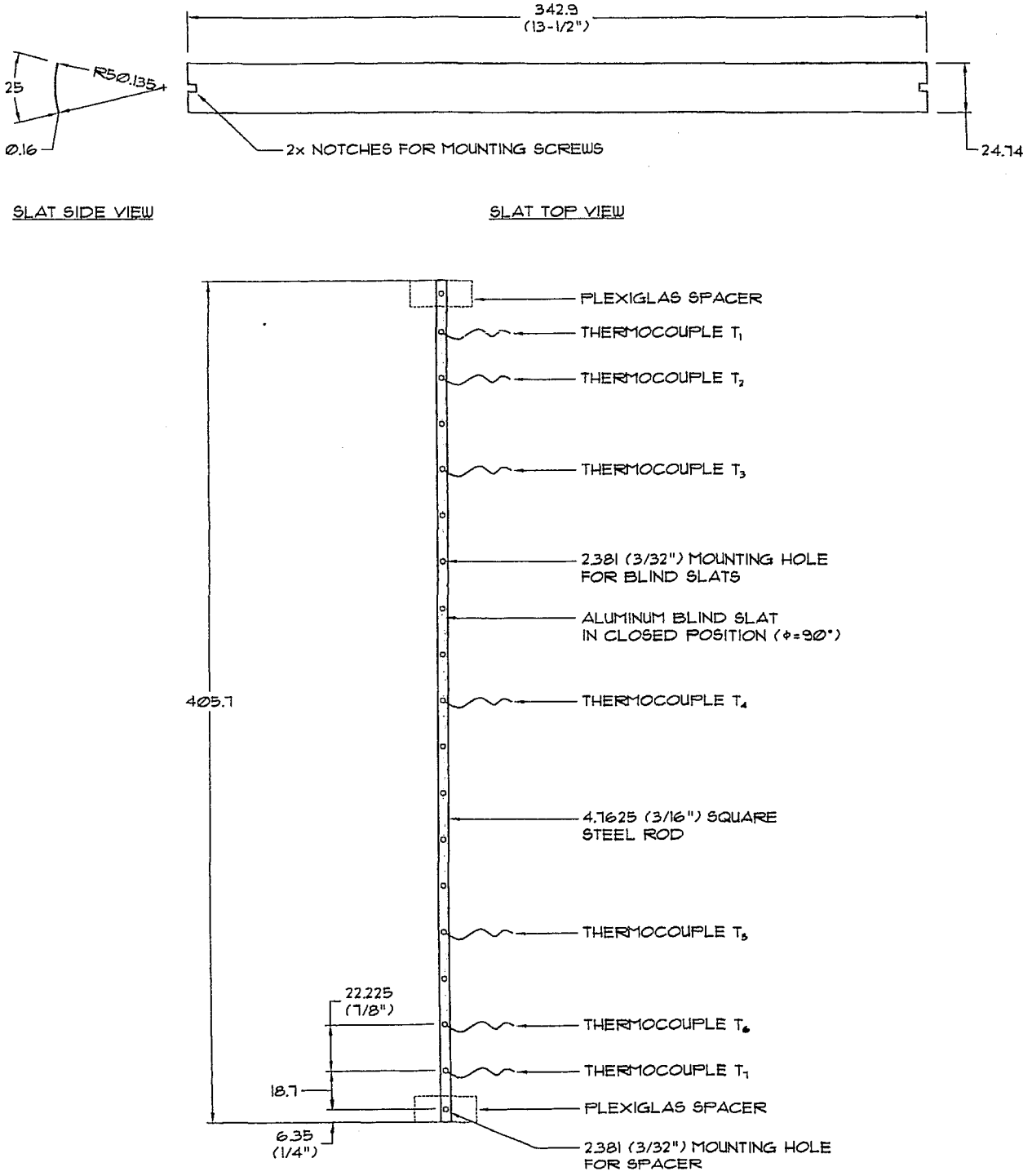

Figure 2.6 Venetian blind slat and support system

to adjust the angle of the slats. Fine 40 gauge thermocouple wires (Omega Engineering Inc. type TT-T-40-SLE) were attached to the underside of some blades, and their temperatures were monitored by the DA system.

2.3.4 Model Assembly

An exploded view of the assembled model is illustrated in Figure 2.7, using the 3D modeling application SolidWorks [66]. Both the hot and cold plates were supported on 50.8mm × 50.8mm (2" × 2") aluminum angle brackets and mounted onto a 9.5mm (3/8") thick aluminum plate. Since the cold plate was to have 12.7mm (1/2") hoses attached to its back for cooling fluid from the temperature bath, it was determined that it shall be fixed to the base plate to prevent the hoses from coming loose due to extensive movement. The hot plate, therefore, was mounted on slotted tracks to permit movement in the x-direction for changing cavity widths. The position of the hot plate was readily adjustable with the use of wing nut fasteners. The base plate was equipped with adjustable legs for leveling of the entire model.

The width of the cavity was controlled by precision machined plexiglas spacers at the top and bottom. Mechanical drawing for these spacers is given in Figure 2.8. The grooves on the spacers served as the centerline location where the support posts for the blind were mounted. The complete blind and spacer assembly rested on the top surface of the plates on four screws attached to an aluminum plate affixed to the top spacer. These screws allowed for easy alignment of the blind in the beam direction. In addition, clamps were used to hold the plate surface firmly against the spacers.

Using FEHT [65] again, the heat transfer through the plexiglas spacers was checked. It was verified that the heat transmission across the spacers between the hot and cold plates did not alter the plate surface temperatures. To ensure minimal heat loss through the spacers to the ambient, the surface temperatures of the hot plate ($T_{s,h} \approx 35°C$) and cold plate ($T_{s,c} \approx 15°C$) were set such that the average temperature in the cavity would be near the ambient temperature ($T_\infty \approx 25°C$).

In order to create a quiescent test environment, the interferometer was located inside an unventilated enclosure. To isolate the cavity from ambient air, which simulates the condition of an actual double-glazed window, an optical window assembly was placed on both sides of the cavity. A pair of existing 15.2cm diameter optical windows mounted in a plexiglas frame were used in a modified assembly. New plexiglas sheets with dimensions as shown in Figure 2.9 were made that can be added to the existing frame. The different sizes were designed such that the assembled optical window would cover the whole cavity when taking photograph of the three individual sections. The optical window assemblies were attached to the side of the aluminum angles supporting the plates at the slots, which allowed for adjustment in cavity width. Foam weather-stripping was used on all sides to further seal the cavity.

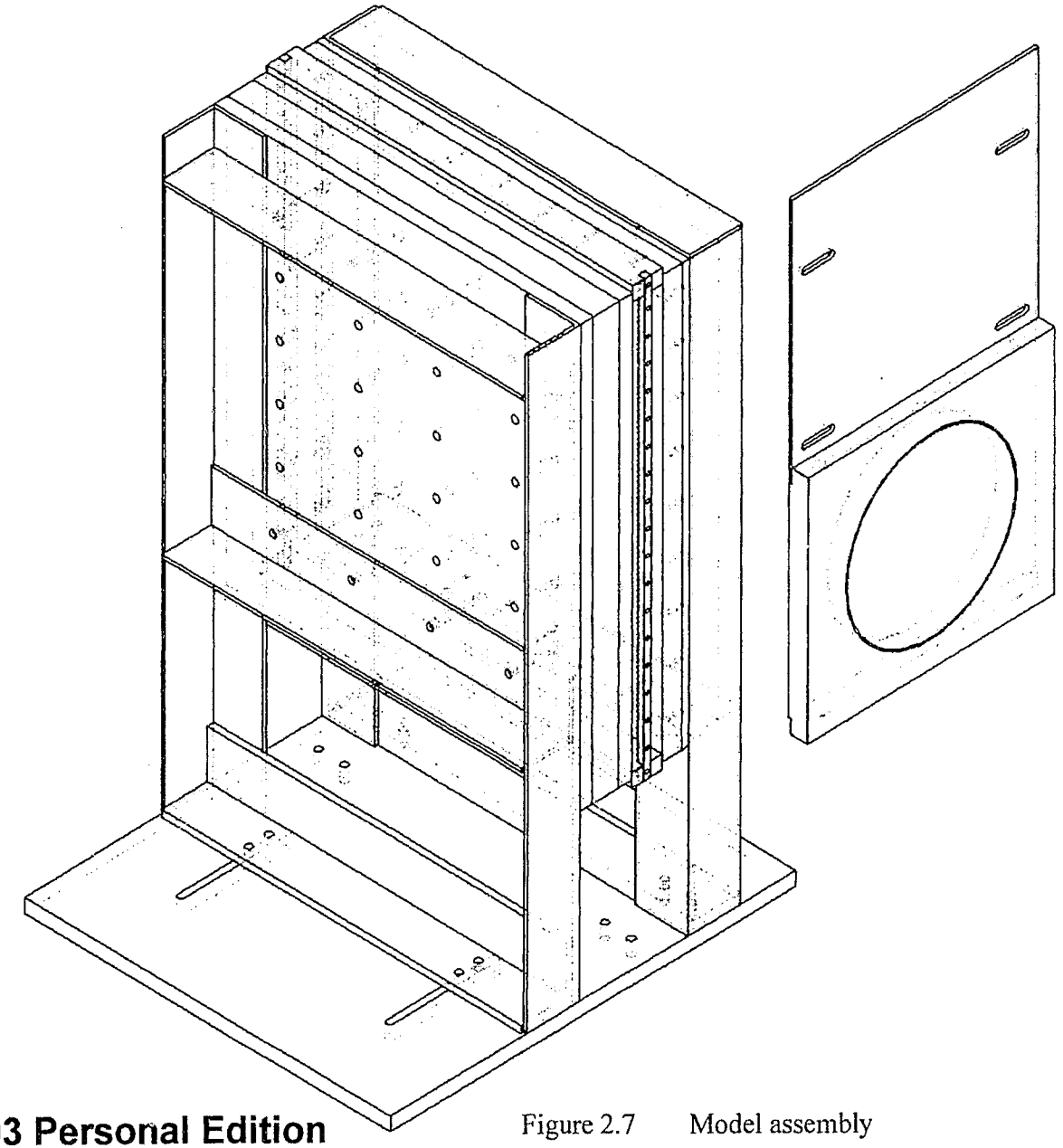

Figure 2.7 Model assembly

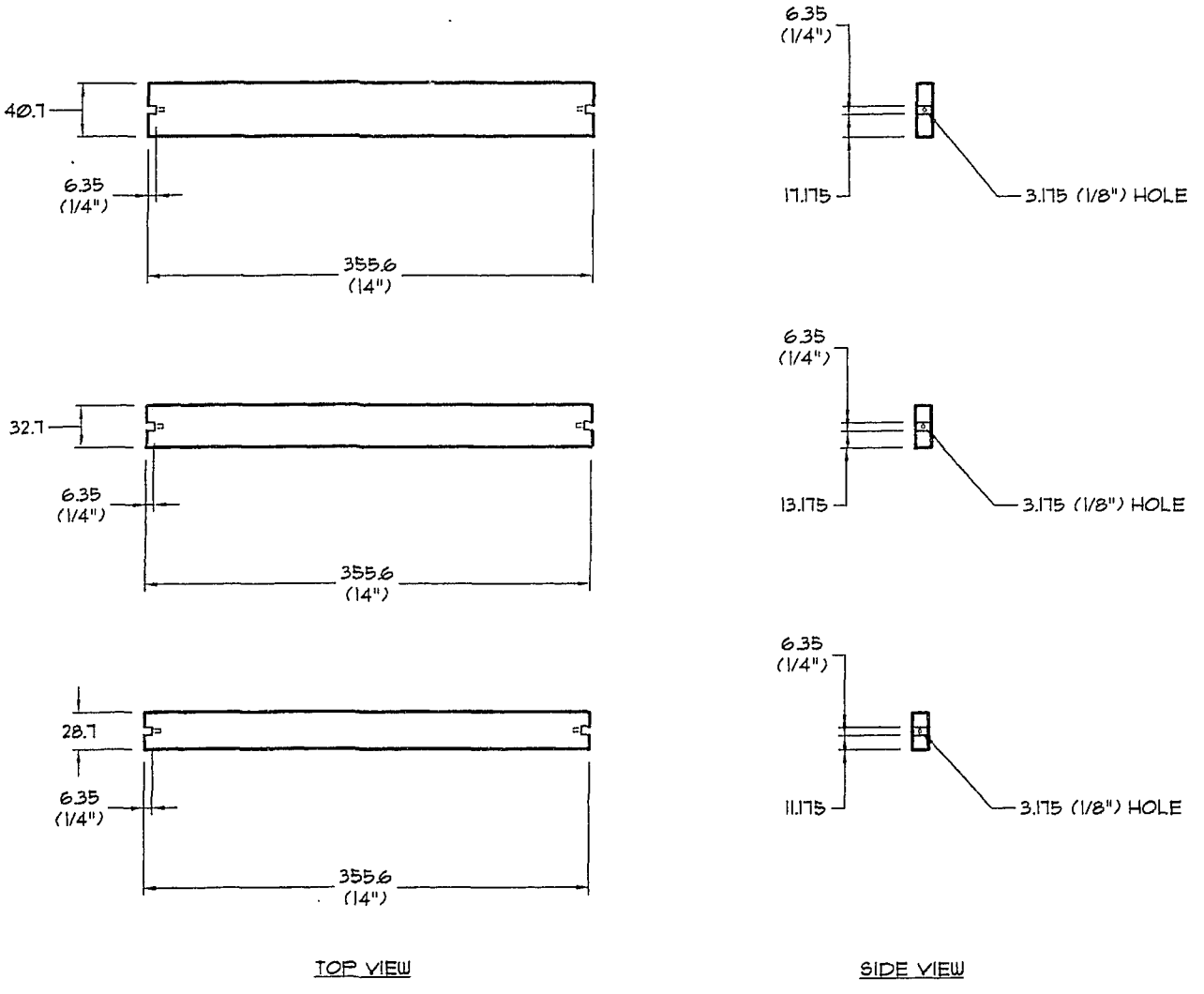

NOTE:

1. PLEXIGLAS SHALL BE 12.7 (1/2") THICK.

Figure 2.8 Mechanical drawing of the plexiglas spacers

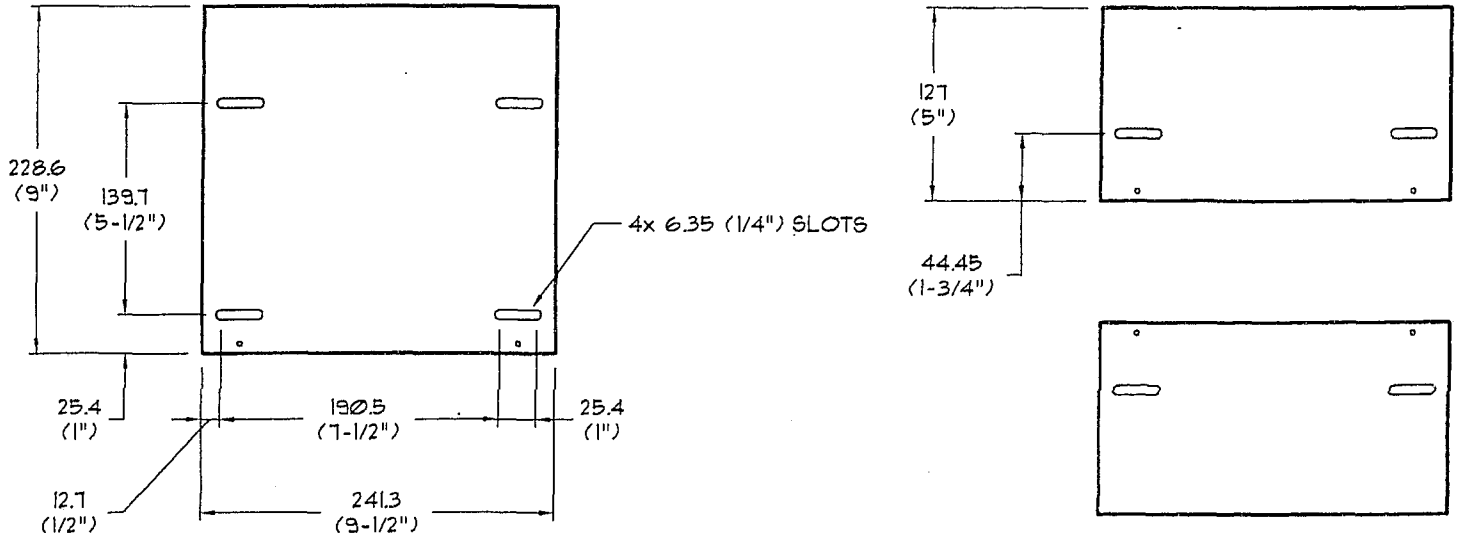

NOTE:

1. PLEXIGLAS SHALL BE 3.175 (1/8") THICK.

Figure 2.9 Mechanical drawing of the plexiglas sheets

2.4 Scanning Apparatus

Finite and infinite fringe interferograms were captured on Polaroid film (type 55 positive-negative 4" × 5" instant sheet film) using a Calumet view camera with the lens removed. The interferograms were analyzed with a manual scanning system consisting of a microscope with a precision traversing and rotating stage that displayed a magnified image on a television monitor. The output of the interferograms was enlarged 160 times to help ease the task of measuring the fringe shifts.

A photograph of the scanning apparatus is shown in Figure 2.10. More detailed information on the scanning apparatus components can be found in Machin's thesis [35].

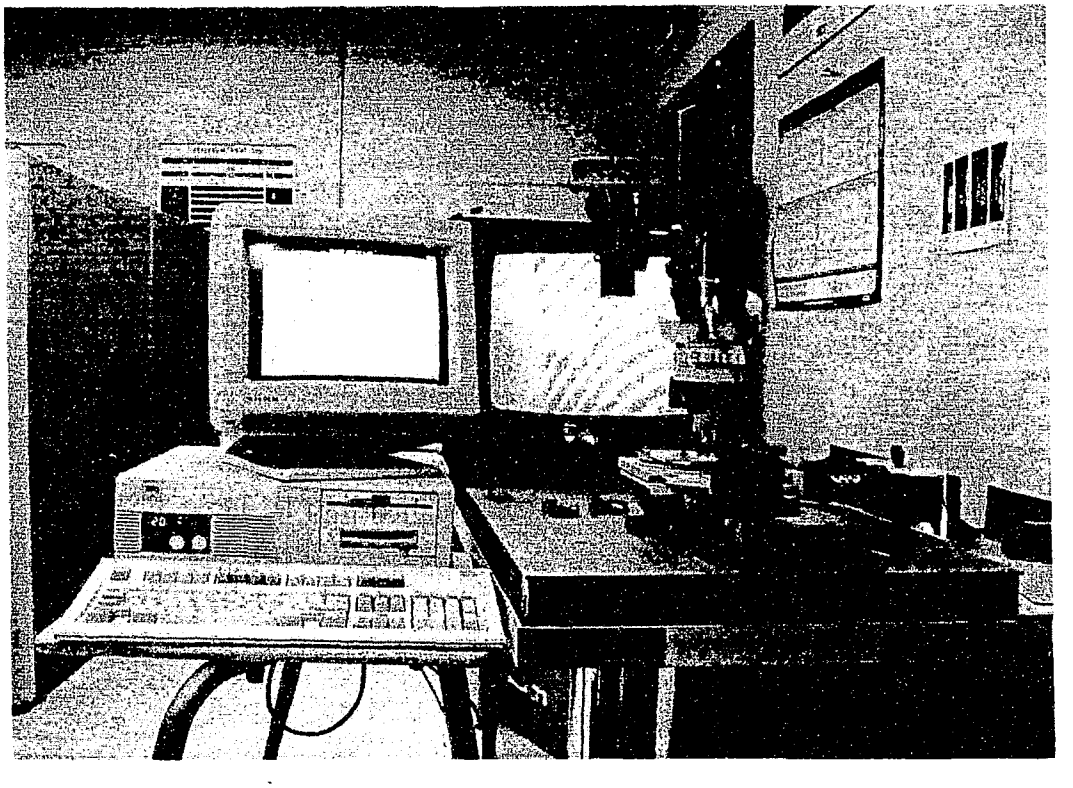

Figure 2.10 Scanning apparatus

Chapter 3

EXPERIMENTAL PROCEDURE AND ANALYSIS

3.1 Introduction

A total of fifty-four photographs were taken under different experimental conditions. Some preliminary pictures were taken to determine the optimal vertical fringe spacing in the finite fringe mode that would generate measurements with the least uncertainty. The range of variables studied with the experimental model was:

s = 2mm, 4mm, and 8mm

ϕ = 0°, 45°, and 90°

where s is the blind tip-to-plate spacing and ϕ is the blind slat angle.

For each experiment, both finite and infinite fringe interferograms were obtained. Infinite fringe setting is when the test beam and reference beam are almost perfectly parallel upon recombination at the second beam splitter; finite fringe setting is when the reference and test beams are purposely misaligned by a small angle upon recombination. It was decided that finite fringe interferograms would be used for heat transfer analysis because a finite fringe pattern can be readily obtained for the cavity problem (see Section 4.2 for more explanation). For comparison, fringe shift measurements were made for both the hot plate and the cold plate. Examples of interferograms of the working experimental model in both the finite and infinite fringe modes are shown in Figure 3.1.

In this chapter, the experimental procedure is outlined, and the analysis of the interferograms, along with the computation of heat transfer results, is explained in detail.

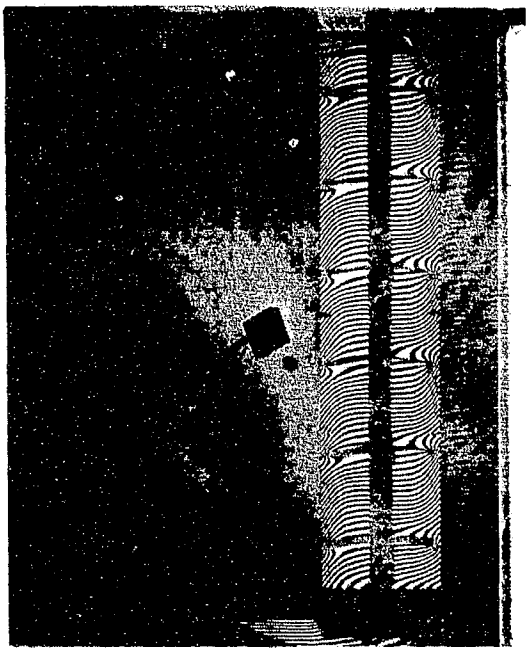

(a) Finite fringe

(b) Infinite fringe

Figure 3.1 Interferograms of working experimental model

3.2 Experimental Procedure

Before proceeding with the experiment, the interferometer must be carefully aligned. A detailed procedure on the alignment of the Ryerson Mach-Zehnder interferometer can be found in Machin's thesis [35].

Initially, before carrying out any alignment, all the thermocouples were plugged into a panel that was hooked up to the DA system just outside the interferometer enclosure. The plate heaters were also plugged into an outlet which was connected to a DC power supply. The hot plate was heated by setting the power supply to the maximum until it approached the desired temperature and the voltage was then set accordingly. A temperature controller was used to regulate the power supply such that the plate remained at the required surface temperature T_s. The hoses were hooked up to the back of the cold plate for circulation from the constant temperature bath.

The ambient pressure was measured using a mercury barometer with a calibration traceable to national standards. It was corrected based on room temperature and gravity according to manufacturer's specifications. For all experiments, a temperature difference between the hot and cold plates of $\Delta T \approx 20°C$ was maintained for the Rayleigh numbers of $Ra \approx 4.5\times10^4$, $Ra \approx 6.7\times10^4$, and $Ra \approx 13.1\times10^4$, based on the cavity widths of $W =$ 28.7mm, $W =$ 32.7mm, and $W =$ 40.7mm, respectively. The Rayleigh number was calculated as follows:

$$Ra = \frac{g\beta(T_s - T_\infty)W^3\rho^2 C_p}{\mu k} \tag{3.1}$$

where g is gravitational acceleration, β the volumetric expansion coefficient, ρ the density of air, C_p the specific heat, μ the dynamic viscosity, and k the thermal

conductivity. All air properties are evaluated at the film temperature (see Appendix A). Since there is no ambient air present in the experiment, the film temperature is taken as the mean cavity temperature. Also, the temperature difference ($T_s - T_\infty$) in the above equation is calculated as the temperature difference across the cavity ($\Delta T = T_{s,h} - T_{s,c}$), with the value for ambient temperature (T_∞) replaced by the average surface temperature of the opposite plate. Thus, equation (3.1) is redefined as:

$$Ra = \frac{g\beta(T_{s,h} - T_{s,c})W^3\rho^2 C_p}{\mu k} \tag{3.2}$$

The test model was placed on a table near the centre of the test beam. The blind structure was mounted on the required spacers, and the assembly was carefully positioned into the model. The position of the hot plate was set and clamps were put in place. The height of the table was adjusted such that the required section of cavity could be viewed in the output. A plumb bob was used to level the model vertically by adjusting the legs of the base plate. The horizontal alignment was also checked against a spirit level.

The interferometer test beam was accurately aligned with the test model. The plates were aligned by lining up the locating pins on the surface. A white card was placed just beyond the model and the flat mirror (M1) was rotated until reflection from the plate surfaces was eliminated, so that the test beam was aligned with the plate surfaces. The blind assembly was also aligned to the test beam by adjusting the screws of the top spacer that were resting on the model. Finally, finite and infinite fringe patterns were obtained using Tarasuk's [63] near field-far field focusing technique.

It was noted that for each section of the cavity, the above alignment procedure had to be repeated to ensure correct alignment of the test beam. Consequently, the finite fringe pattern had to be reset each time the flat mirror (M1) was adjusted. These minor

adjustments were very time-consuming and were not carried out during the infinite fringe mode. Such high accuracy was not necessary since the infinite fringe interferograms were not used for heat transfer measurements.

The angle of each blind slat was manually set one by one. With the reference beam blocked, the slat angle was set by matching the interferometric output against a special grid of the required angle. All seventeen blind slats were painstakingly set by checking the output image of the three different sections of cavity before the experiments began.

The camera was positioned and leveled with the image reflected from a small mirror at the focal point. The camera was aligned so that the image fit completely in the lens. A scale photo was taken at a shutter speed of $1/30^{th}$ of a second with the reference beam blocked and the model at room temperature. As the system reached steady-state, the lights in the room were turned off and an interferogram was taken at a shutter speed of $1/60^{th}$ of a second. Finite fringe interferograms were taken first for all experiments. The interferograms were developed according to Polaroid's instructions and then scanned. Finally, another set of experiments were repeated and infinite fringe interferograms were obtained for visualization.

3.3 Interferogram Analysis

The analysis of interferograms is based on the wave nature of light. The amplitude (a) of a monochromatic light, such as the laser light used in the present experiment, traveling in the x-direction can be expressed as:

$$a = a_o \sin\frac{2\pi}{\lambda}(ct - x) \tag{3.3}$$

where a_o is the maximum amplitude, λ the wavelength, c the speed of light, t the time and x the position. Thus, the amplitude of the reference beam at a fixed point can be expressed as:

$$a_{ref} = a_{o,ref} \sin\frac{2\pi ct}{\lambda} \tag{3.4}$$

Similarly, the amplitude of the test beam at the same position can be expressed as:

$$a_{test} = a_{o,test} \sin\left(\frac{2\pi ct}{\lambda} - \phi\right) \tag{3.5}$$

where ϕ is the phase shift between the two beams due to the different index of refraction of the air at the test section.

Assuming the maximum amplitude of both beams to be equal ($a_{o,ref} = a_{o,test} = a_o$), the recombined output beam can be written as the sum of equations (3.4) and (3.5):

$$a = a_o\left(\sin\frac{2\pi ct}{\lambda} + \sin\left(\frac{2\pi ct}{\lambda} - \phi\right)\right) \tag{3.6}$$

It can be seen that constructive interference will occur when $\phi/2\pi$ is an integer, and destructive interference will occur when $(\phi/2\pi) + 1/2$ is an integer. The constructive and destructive fringes can be measured on the interferograms. The distance from fringe centre to fringe centre represents a phase difference of one wavelength between the two beams.

A fringe shift (ε) occurs when the test beam is 180° out of phase with the reference beam, which is when the number of wavelengths in the direction of the reference beam differs by an integer amount. Using the plate surface as reference, this can be expressed as:

$$\varepsilon = N - N_{ref} \equiv \text{integer} \tag{3.7}$$

where N is the number of wavelengths, which can be determined for a given wavelength if the length of the model (Z) is known, as follows:

$$N = \frac{Z}{\lambda} \tag{3.8}$$

The index of refraction (n) of a medium is the ratio of the speed of light in a vacuum (c_o) to the speed of light in the medium (c):

$$n = \frac{c_o}{c} = \frac{\lambda_o}{\lambda} = \frac{N}{N_o} \tag{3.9}$$

With the refractive index of one beam being a known constant value (n_{ref}), equation (3.7) can be written as:

$$\varepsilon = N(n - n_{ref}) = \frac{Z}{\lambda}(n - n_{ref}) \tag{3.10}$$

The relationship between the index of refraction and density (ρ) of a fluid is given by the Lorenz-Lorenz equation:

$$\frac{(n^2 - 1)}{(n^2 + 2)\rho} = \frac{3}{2}G \tag{3.11}$$

where G is the Gladstone-Dale constant, which is dependent on the type of fluid and the wavelength of light. For air and a He-Ne laser ($\lambda = 6.328\times10^{-7}$ m), $G = 0.226\times10^{-3}$ m^3/kg [67]. Since air has a refractive index of nearly 1 (n = 1.0002716 at standard temperature and pressure [62]), equation (3.11) can be reduced to:

$$\frac{(n - 1)}{\rho} = G \tag{3.12}$$

It follows that for air at the plate surface:

$$n_{ref} = G\rho_{ref} + 1 \tag{3.13}$$

and for air near the test section:

$$n = G\rho + 1 \tag{3.14}$$

Substituting equations (3.13) and (3.14) into equation (3.10) yields:

$$\varepsilon = \frac{ZG}{\lambda}\left(\rho - \rho_{ref}\right) \tag{3.15}$$

For the present study, air can be considered to behave as an ideal gas. Thus, for a given pressure (p) and ideal gas constant of air (R = 287 J/kg·K), the relationship between fluid density and temperature (T) is:

$$\rho = \frac{p}{RT} \tag{3.16}$$

Substituting equation (3.16) into equation (3.15) gives the equation for determining fringe shift between two known temperatures:

$$\varepsilon = \frac{ZpG}{R\lambda}\left(\frac{1}{T} - \frac{1}{T_{ref}}\right) \tag{3.17}$$

Solving for temperature, equation (3.17) can be written in a more useful form as:

$$T = \frac{T_{ref}}{\frac{\varepsilon R\lambda T_{ref}}{GpZ} + 1} \tag{3.18}$$

In the present study, the plate surface temperature T_s was used as the reference temperature in equation (3.18) to calculate fringe temperatures. Since the first fringe did not necessarily represent a full fringe shift from the plate surface, linear extrapolation of the first two fringes closest to the surface was used to determine the fractional fringe shift. Each consecutive fringe was then represented by this fractional shift plus an integer amount.

3.4 Calculation of Local and Average Plate Nusselt Numbers

An expression for the local heat transfer coefficient (h) can be found by equating the heat transferred by convection to the heat transferred by conduction at the plate surface ($x = 0$), as follows:

$$-k_s \left.\frac{dT}{dx}\right|_{x=0} = h\left(T_{s,h} - T_{s,c}\right) \tag{3.19}$$

$$h = \frac{-k_s \left.\frac{dT}{dx}\right|_{x=0}}{\left(T_{s,h} - T_{s,c}\right)} \tag{3.20}$$

where k_s is the thermal conductivity of air evaluated at the surface temperature obtained from property tables (see Appendix A).

The local Nusselt number (Nu) is defined as:

$$Nu = \frac{hW}{k_f} = \frac{-k_s W \left.\frac{dT}{dy}\right|_{x=0}}{\left(T_{s,h} - T_{s,c}\right) k_f} \tag{3.21}$$

where k_f is the thermal conductivity of air evaluated at the film temperature, also obtained from property tables. The temperature gradient (dT/dy) at the wall is obtained from the fringe temperature profiles on the interferogram. The temperature difference ($T_{s,h} - T_{s,c}$) is calculated from the average plate temperatures measured from thermocouples.

The average Nusselt number (Nu_{avg}) is determined by numerically integrating the local values over the span of the plate using the trapezoidal rule.

A complete sample calculation is given in Appendix C.

Chapter 4

PRESENTATION AND DISCUSSION OF RESULTS

4.1 Introduction

Free convective heat transfer in a double-glazed window with a between-panes Venetian blind was visualized and the heat transfer results were analyzed. Using a Mach-Zehnder interferometer, experiments were conducted on a cavity of height L = 380.3mm with louvers mounted at the centre at blind tip-to-plate spacings of s = 2mm, s = 4mm, and s = 8mm, and at blind slat angles of $\phi = 0°$, $\phi = 45°$, and $\phi = 90°$ from the horizontal. Finite fringe interferograms were taken of the fringe shift field between the hot and cold isothermal flat plates at a temperature difference of $\Delta T \approx 20°C$. Heat transfer measurements were made at the Rayleigh numbers of $Ra \approx 4.5\times10^4$, $Ra \approx 6.7\times10^4$, and $Ra \approx 13.1\times10^4$, based on cavity widths of W = 28.7mm, W = 32.7mm, and W = 40.7mm, respectively. Local and average Nusselt numbers were obtained for heat transfer analysis. Infinite fringe interferograms were also obtained to visualize the temperature field inside the cavity.

4.2 Finite and Infinite Fringe Interferograms

For each test geometry, two composite interferograms were taken, one in finite fringe mode and the other in infinite fringe mode.

Figure 4.1 shows two composite images for $s = 2$mm and $\phi = 0°$, each composed of three separate photographs. Due to restriction in the size of the optical output of the MZI, the length of the cavity was divided into three individual shots, showing the top, middle, and bottom sections of the cavity.

In classical interferometry, the infinite fringe mode is usually preferred when obtaining images for heat transfer analysis. In applications where the test fluid is a gas at constant pressure, as is the case in this study, the fringes represent lines of constant temperature. Thus, infinite fringe interferograms have the advantage of providing full temperature field visualization. Normally, when setting the infinite fringe pattern, the optics must be adjusted so that no fringe appears in regions of ambient air, where there is no change in temperature. Since ambient air was not present in the cavity, it was not possible to achieve an infinite fringe pattern with high precision.

In order to overcome this problem, it was decided that the finite fringe mode shall be used for heat transfer analysis. In this mode of operation, there is no need for the presence of ambient air when setting the finite fringe pattern. Moreover, in regions of low heat transfer rates, such as the top and bottom ends of the cavity, fringes can become fat and indistinct on infinite fringe interferograms, making it difficult to locate fringe centres. With finite fringe interferograms, fringe shift data can be obtained more easily.

Although infinite fringe interferograms were not used for making heat transfer measurements, they were taken for visualization and discussion purposes. The infinite fringe interferograms for the blind slat angles of $\phi = 0°$, $\phi = 45°$, and $\phi = 90°$ at the three different blind tip-to-plate spacings are presented in Figures 4.2, 4.3, and 4.4, respectively.

(a) Finite fringe (b) Infinite fringe

Figure 4.1 Composite finite and infinite fringe interferograms for $s = 2$mm and $\phi = 0°$

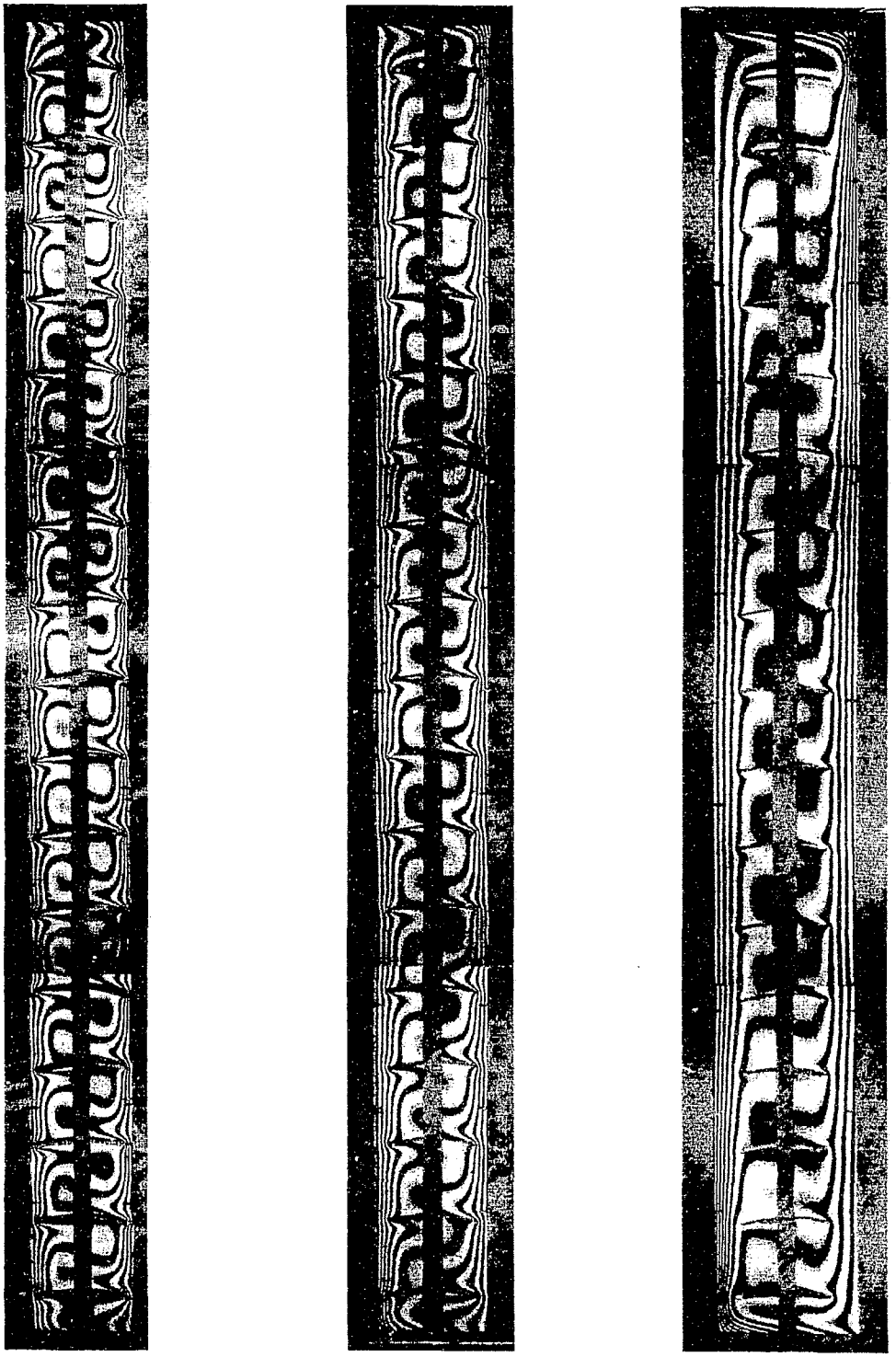

(a) $s = 2$mm (b) $s = 4$mm (c) $s = 8$mm

Figure 4.2 Composite infinite fringe interferograms for $\phi = 0°$ at various s

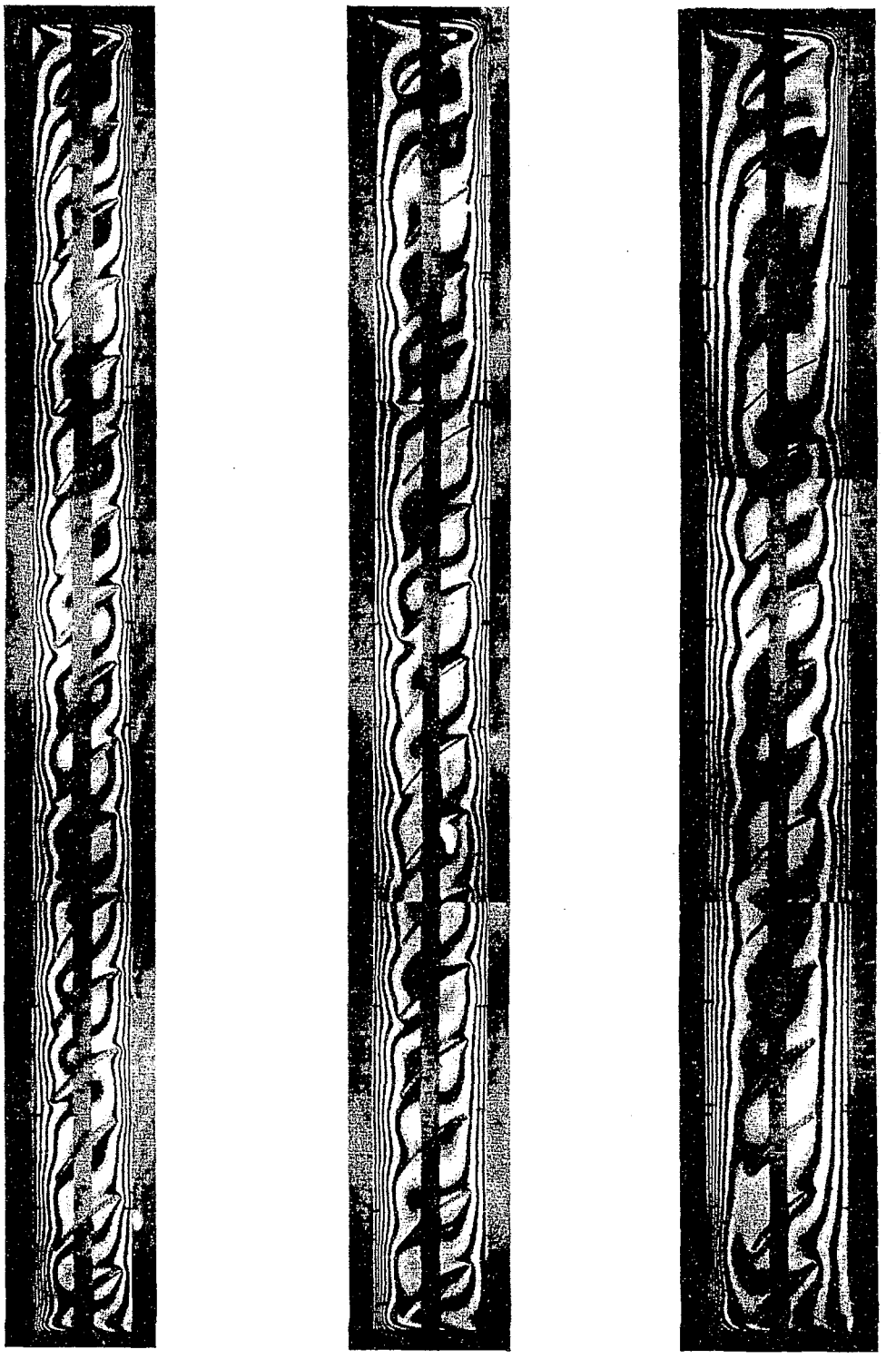

(a) $s = 2$mm (b) $s = 4$mm (c) $s = 8$mm

Figure 4.3 Composite infinite fringe interferograms for $\phi = 45°$ at various s

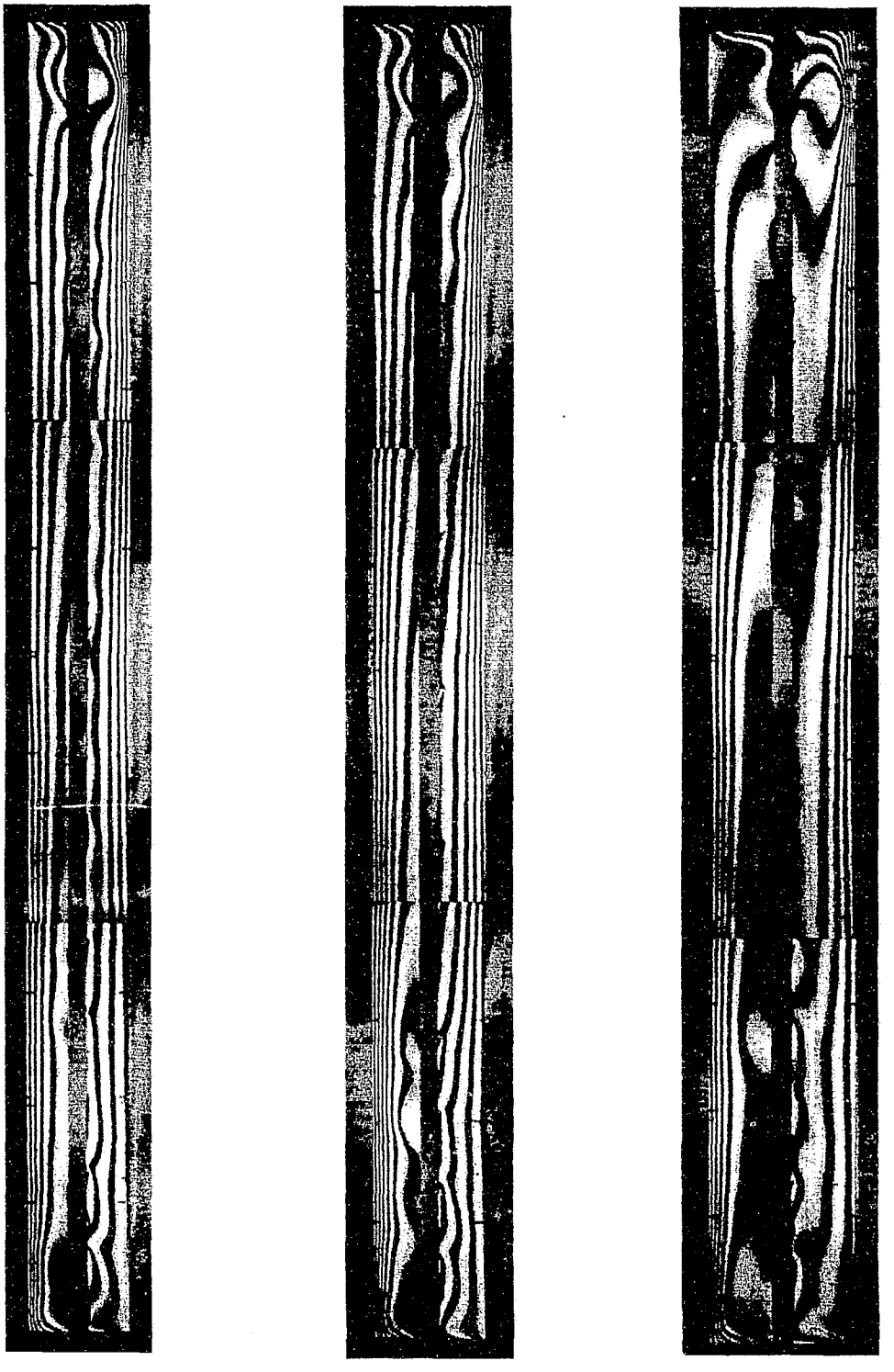

(a) $s = 2$mm (b) $s = 4$mm (c) $s = 8$mm

Figure 4.4 Composite infinite fringe interferograms for $\phi = 90°$ at various s

4.3 Heat Transfer Results

The distribution of local Nusselt numbers corresponding to the finite fringe interferogram for the case with blind tip-to-plate spacing of s = 2mm and blind slat angle of $\phi = 0°$ is shown in Figure 4.5. The results for both the hot plate and the cold plate are simultaneously plotted, along with the positions of each blind slat. In this configuration, the tips of the slats are very close to the plate surfaces. In effect, the slats are acting as a thermal bridge, increasing the conductive heat transfer rate across the cavity. This can be seen in the periodic extreme peaks and valleys on the graph, corresponding respectively to the maximum absolute values of local Nusselt numbers on the hot and cold plates, matching the location of each blind slat. Referring back to Figure 4.2, the infinite fringe interferogram shows the fringes close together near the plate surface at the slat tip locations, which indicates that the air flow is restricted by the slat, causing an increase in fluid velocity. Nevertheless, it is mostly conduction in the blind that contributes to the high heat transfer rates found at these peaks.

The air flow described above is generated by the hot air rising up the hot plate, turning at the top of the cavity, then meeting the cold plate and continuing downwards in a circulating movement around the cavity in the gap between the blind and the enclosure. For convenience, this shall be referred to as the outer circulation. Another type of air flow occurring simultaneously inside the cavity is the inner circulation, where hot and cold air interchanges in a circulating pattern in the spaces between each blind slat. The two types of air circulation are illustrated in Figure 4.6. This phenomenon is reminiscent of boundary layer flow on the vertical walls and secondary cellular flow in the core region defined in early literatures for free convection in vertical cavity [5, 6].

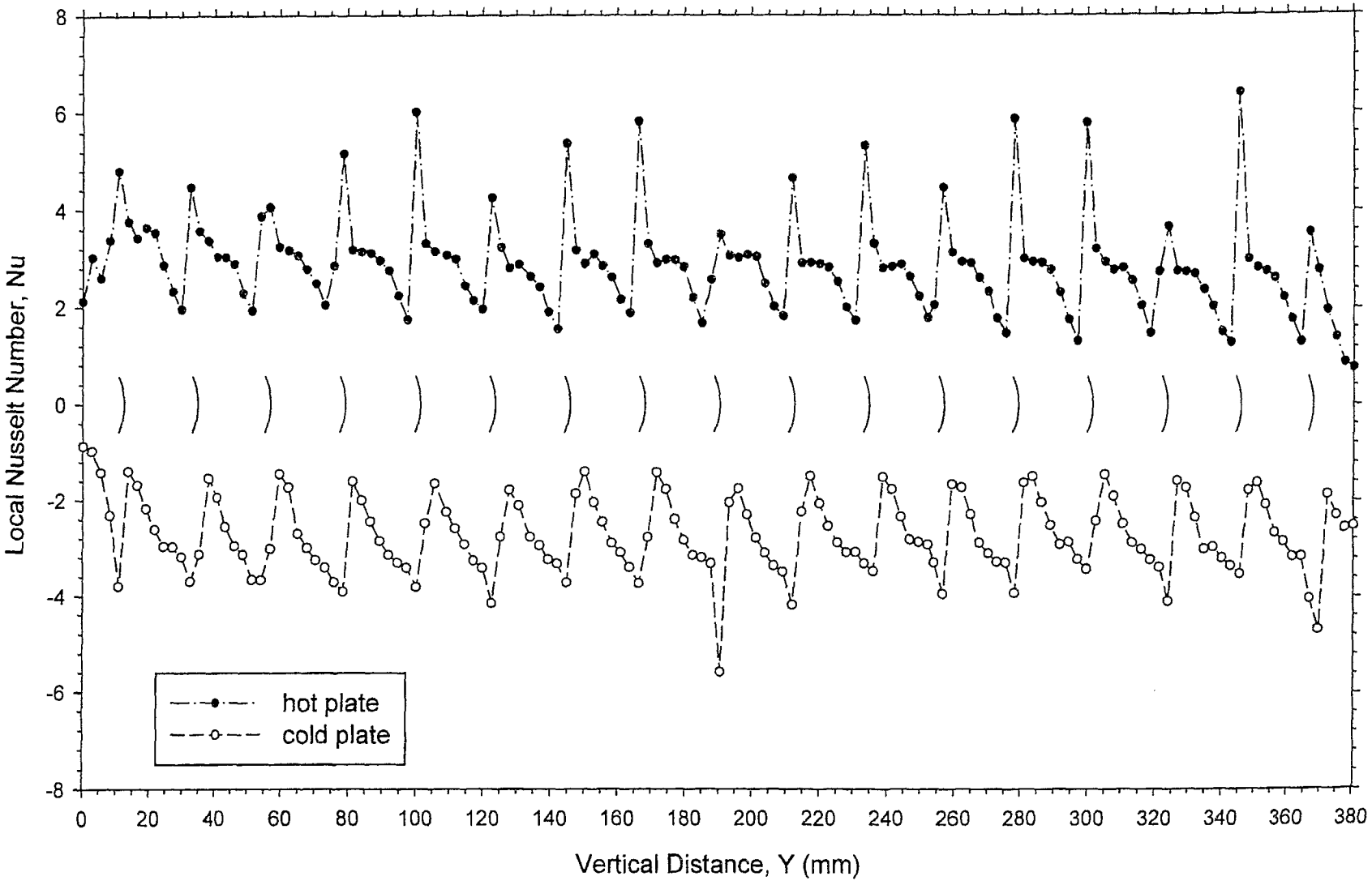

Figure 4.5 Local Nusselt number distribution for $s = 2$mm and $\phi = 0°$ at $Ra \approx 4.5\times10^4$

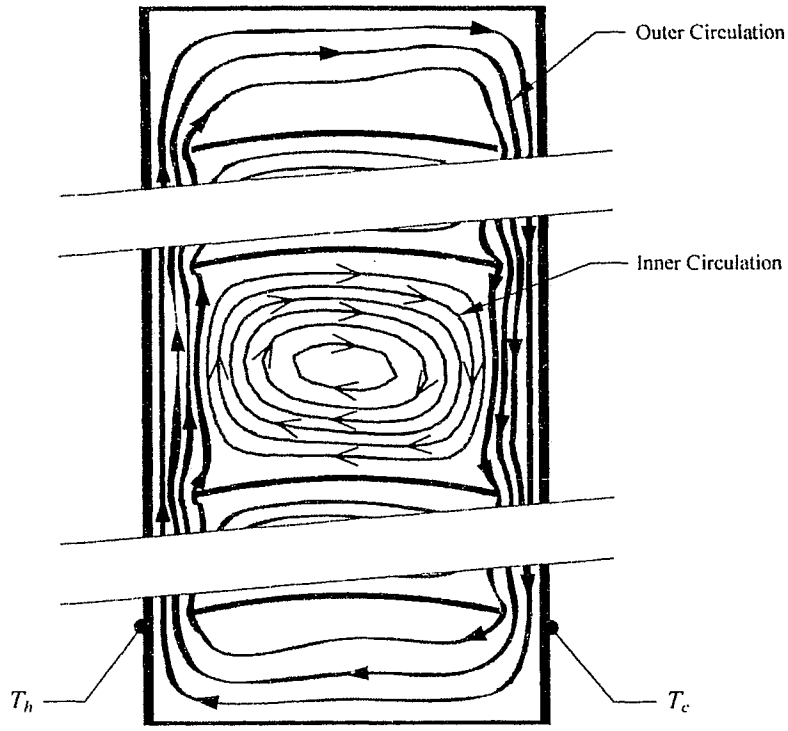

Figure 4.6 Sketch of inner and outer circulation flows

Figure 4.7 shows the local Nusselt number distribution for the case with blind tip-to-plate spacing of s = 4mm and blind slat angle of $\phi = 0°$. There are still periodic peaks where heat transfer rates are higher at the location of blind slats. With the increase in blind tip-to-plate spacing, however, the conductive effect of the slats is less prominent, so the magnitude of the peaks on the graph is smaller. As seen in Figure 4.2, the fringes are spaced further apart at the slat locations. As the space increases between the blind and the plates, convection increases as outer circulation flow grows stronger. The effect of convection is especially noticeable at the top and bottom ends of the cavity, where the air

turning at the corners and impinging on the opposite plate surface causes higher heat transfer rates for the cold and hot plates, respectively.

The local Nusselt number distribution shown in Figure 4.8 is also for the blind slat angle of $\phi = 0°$, but at the widest blind tip-to-plate spacing of $s = 8$mm. At this setting, there are no periodic peaks found on the graph, meaning that the conductive effect of the blind slats is largely lost when the tips of the slats are far from the plate surfaces. The infinite fringe interferogram in Figure 4.2 shows the slats having minimal effect on the local fringe spacing. Instead, heat transfer is dominated by the convective flow of the outer circulation, with evidence of very strong end effects found both on the graph and on the infinite fringe interferogram. From the interferogram, one can clearly see the development of the thermal boundary layer on the hot and cold plates, with low temperature gradients across the core region of the cavity.

The local Nusselt number distribution graphs for the blind slat angle of $\phi = 0°$ at the three different blind tip-to-plate spacings are shown together in Figure 4.9. For clarity, only heat transfer results for the hot plate are plotted on graphs used for the purpose of comparison. The graph shows the period of the peaks matches with the pitch of the blind slats, but the scale of the peaks differs between $s = 2$mm and $s = 4$mm. If the peaks are disregarded, the heat transfer rates remain relatively steady over the height of the cavity. This indicates that the convective effect of the outer circulation is small relative to the conductive effect of the blind slats for these two cases, except for the bottom region of $s = 4$mm, where air circulation is stronger. In contrast, for $s = 8$mm, the effect of convection is evident in the high Nusselt numbers at the bottom end of the plate, and the continuous decrease in heat transfer rate towards the top end of the plate.

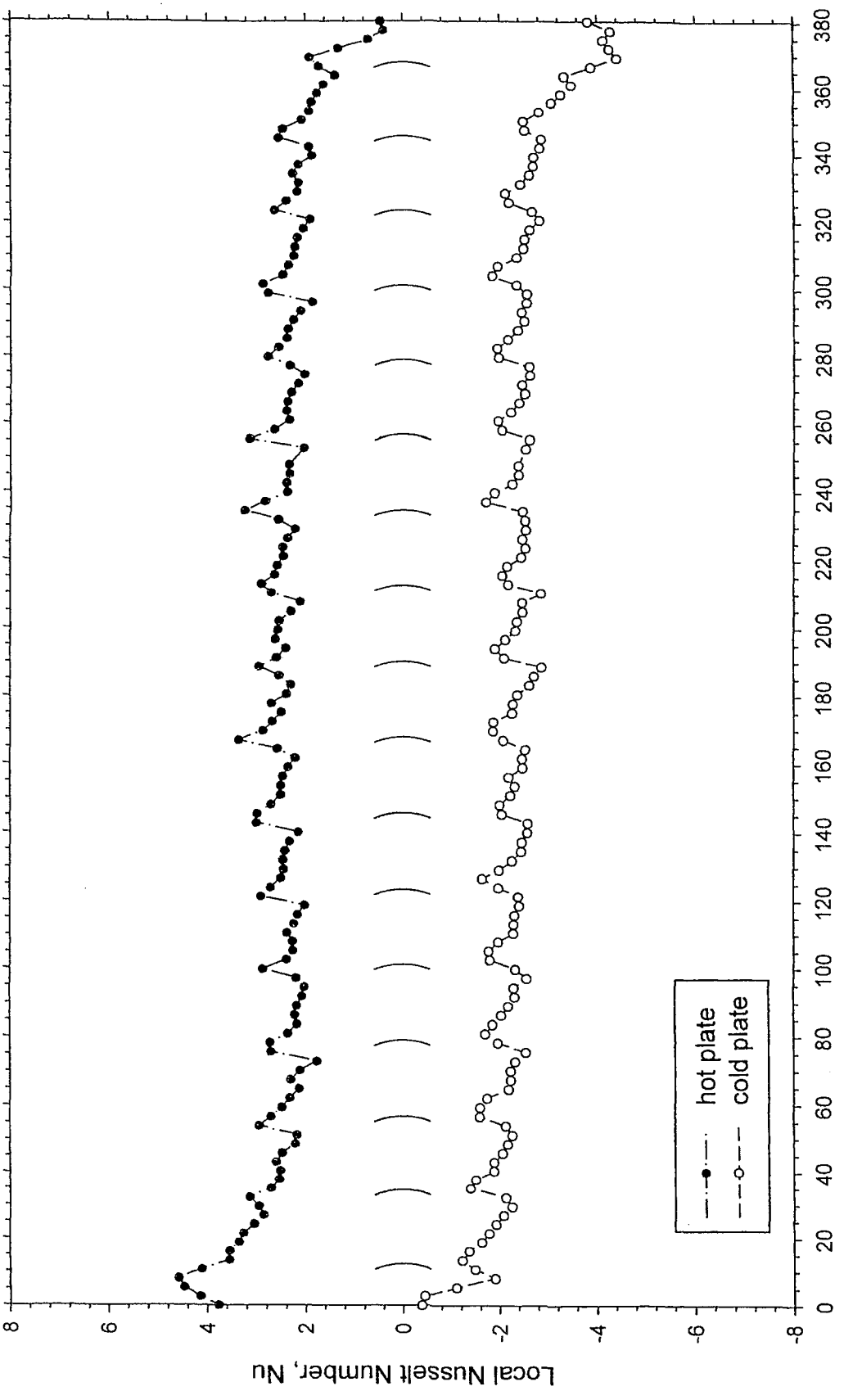

Figure 4.7 Local Nusselt number distribution for $s = 4$mm and $\phi = 0^{\circ}$ at $Ra \approx 6.7\times10^{4}$

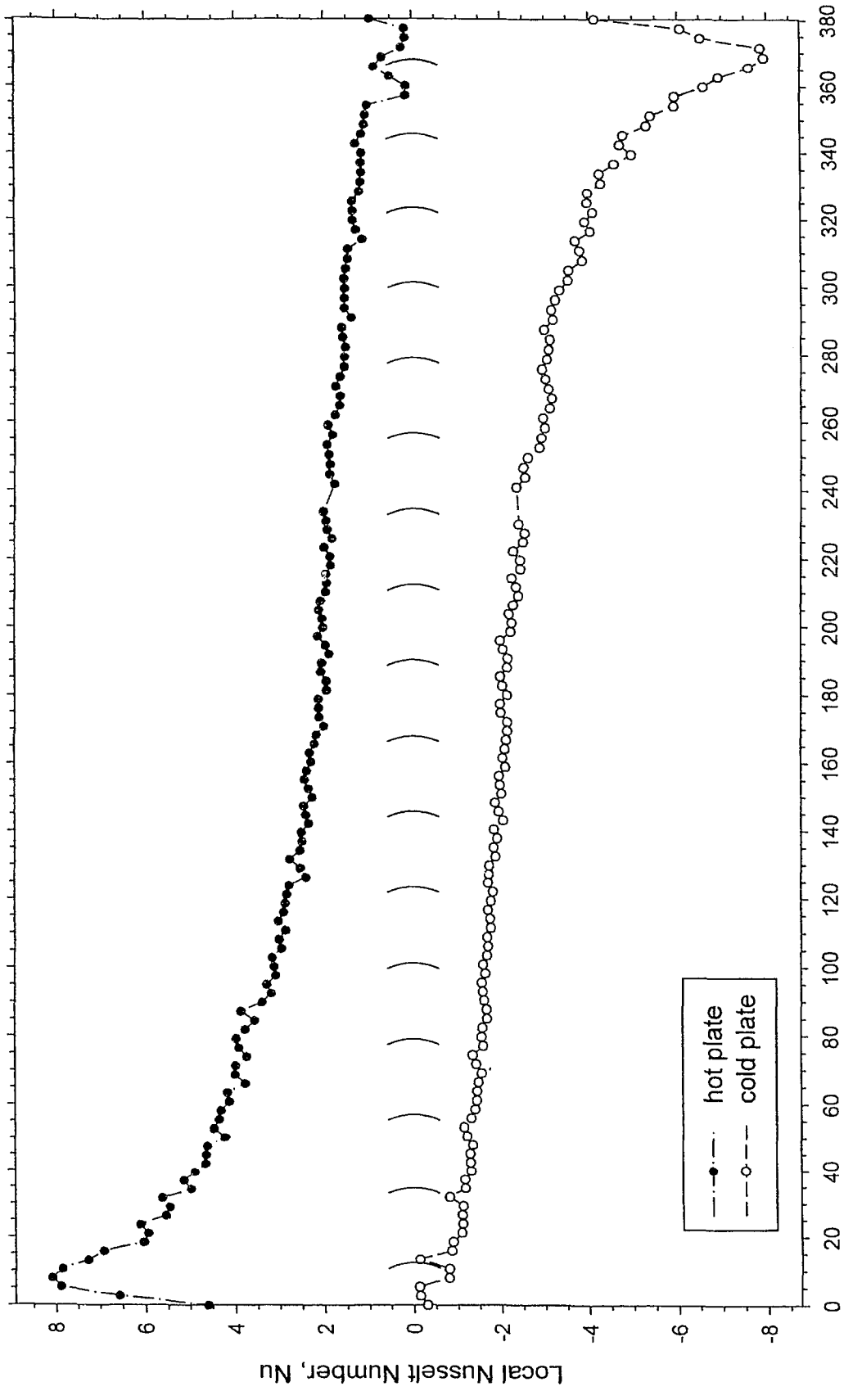

Figure 4.8 Local Nusselt number distribution for $s = 8$mm and $\phi = 0°$ at $Ra \approx 13.1 \times 10^4$

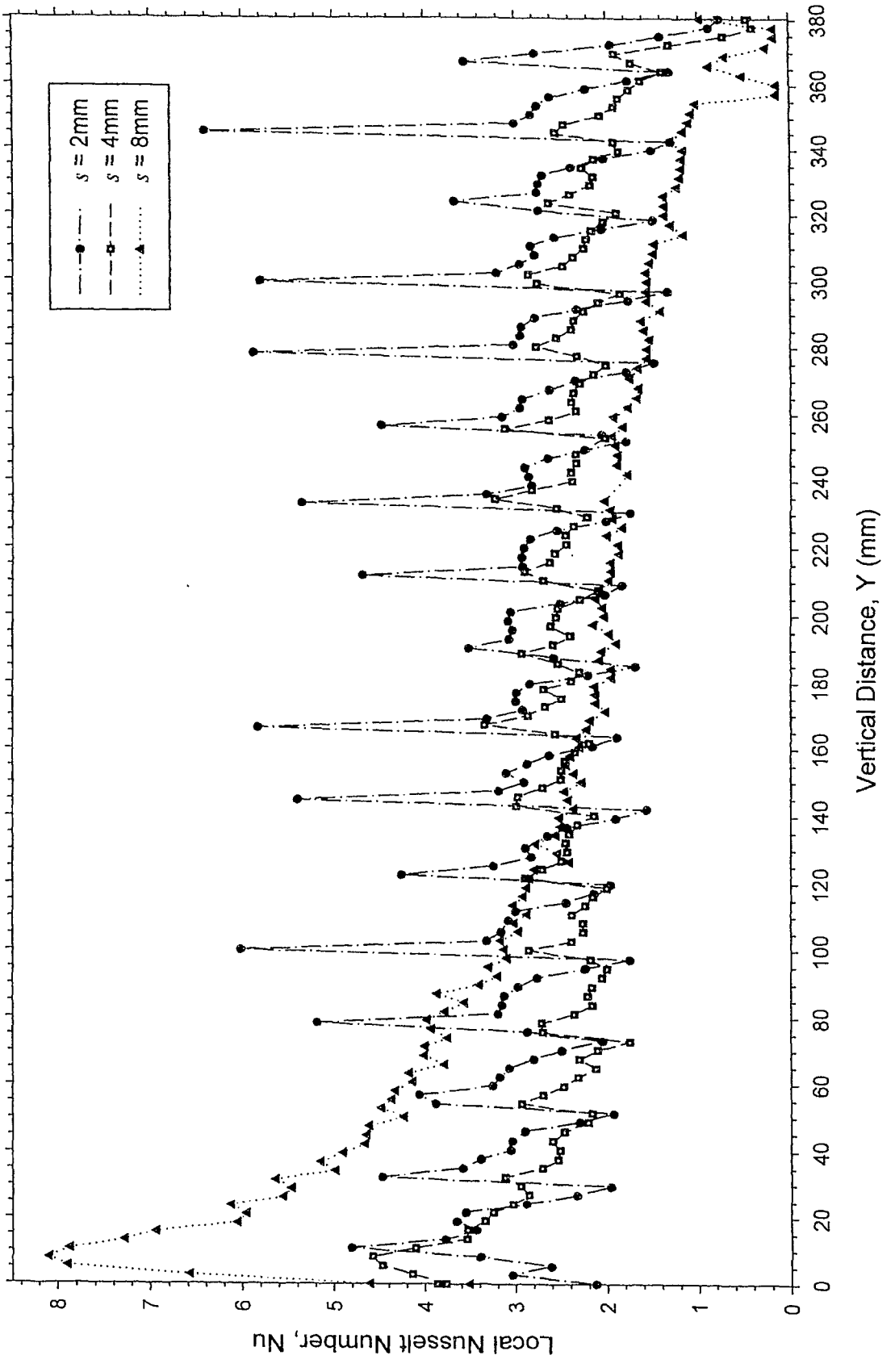

Figure 4.9 Local Nusselt number distributions for $\phi = 0°$ at various s

Figure 4.10 shows the distribution of local Nusselt numbers for the case of blind tip-to-plate spacing of s = 2mm and blind slat angle of $\phi = 45°$. At this slat angle, the gap between the blind tips and the surfaces of the plates is, in reality, more than 2mm. In turn, the conductive effect of the slats is less significant. By inspecting the location of the peaks, it is found that the maximum Nusselt numbers occur at regions between each slat, where the inner circulation flow takes place. The interaction between this inner circulation and the outer circulation pushes the boundary layer towards the plate surfaces, causing an increase in heat transfer rate. This can be observed on the infinite fringe interferogram in Figure 4.3. The high heat transfer rate caused by convective flow at the end regions of the cavity is also noted.

The local Nusselt number distribution for the blind slat angle of $\phi = 45°$ for the cases of blind tip-to-plate spacing of s = 4mm and s = 8mm are shown respectively in Figures 4.11 and 4.12. The heat transfer results for these are similar to those for the case of s = 2mm, with periodic peaks happening at locations between each blind slat. The infinite fringe interferograms in Figure 4.3 also show a similar trend. It is interesting to find periodic variations even at these wide spacings, which indicates that the effect of the inner circulation on the local heat transfer rate is rather strong.

The graphs for all three cases of blind tip-to-plate spacing at the blind slat angle of $\phi = 45°$ are shown in Figure 4.13. Since the peaks are caused by convective effect of the inner circulation flow rather than the conductive effect of the slats, their amplitudes do not differ much between the different blind tip-to-plate spacings, unlike the previous case of blind slat angle $\phi = 0°$. As the distance between the blind and plate surfaces increases, there is evidence of strengthening convection around the entire enclosure as outer circulation grows stronger. At the bottom of the cavity, local heat transfer rate

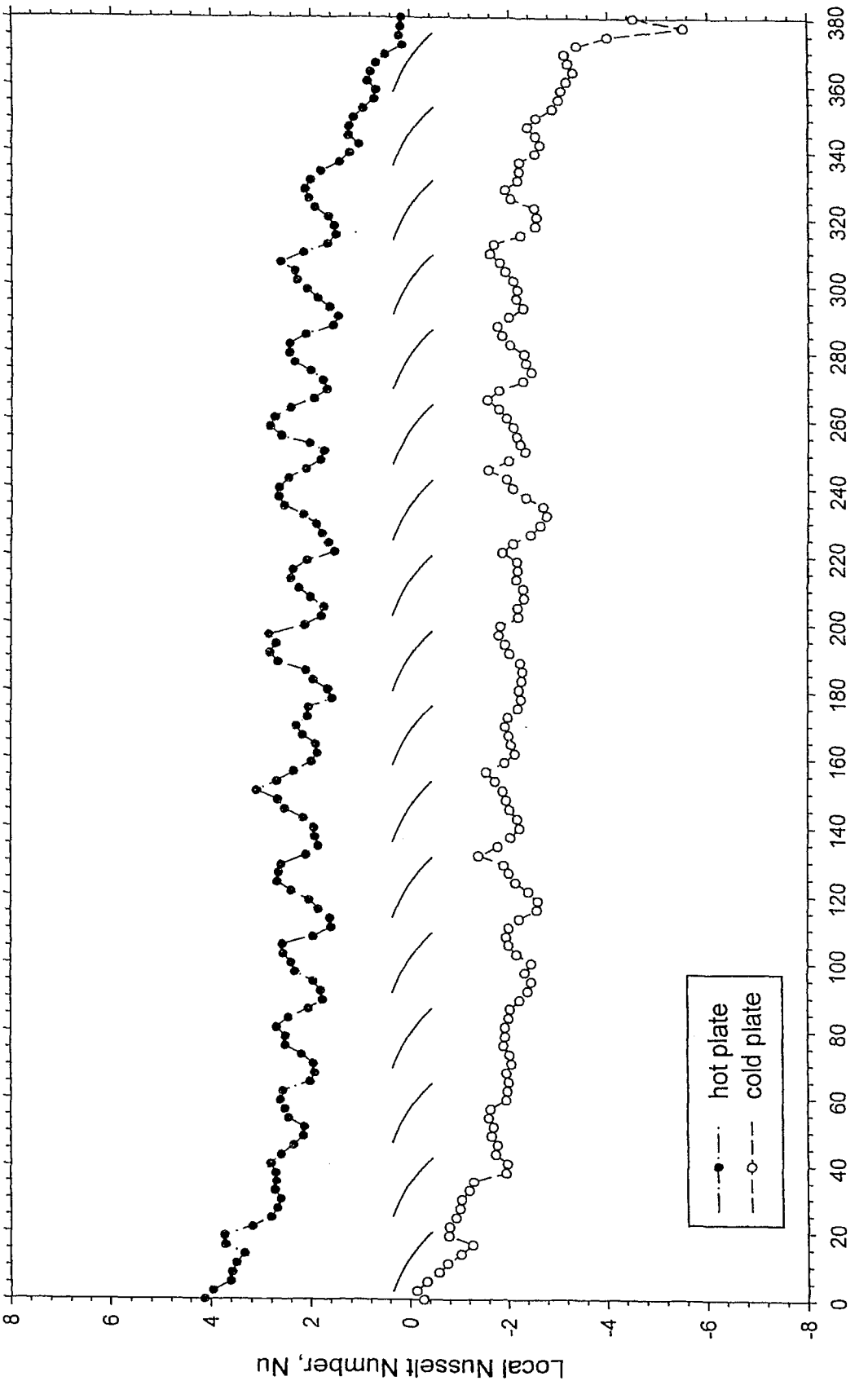

Figure 4.10 Local Nusselt number distribution for $s = 2$mm and $\phi = 45°$ at $Ra \approx 4.5\times10^4$

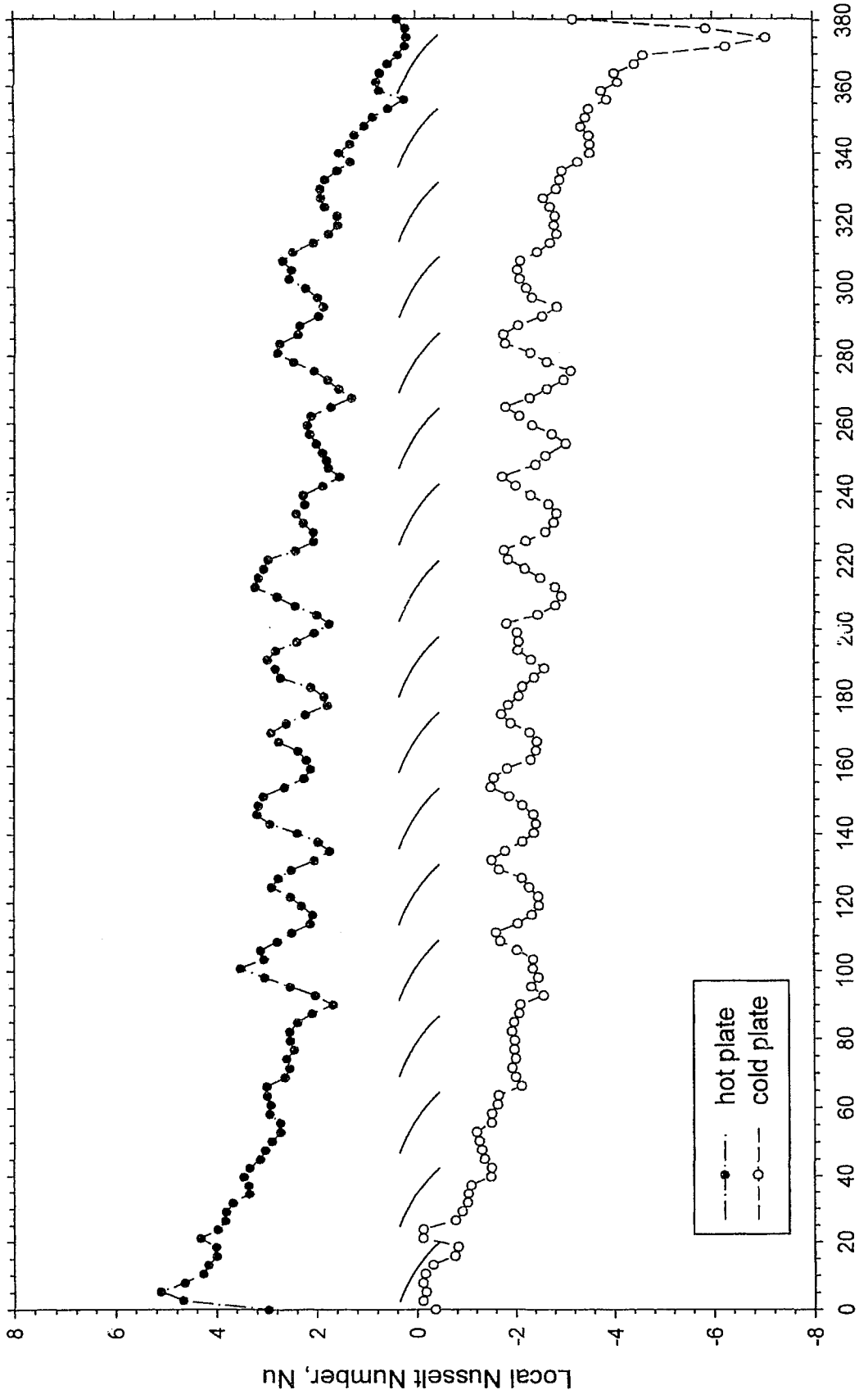

Figure 4.11 Local Nusselt number distribution for $s = 4$mm and $\phi = 45°$ at $Ra \approx 6.7 \times 10^4$

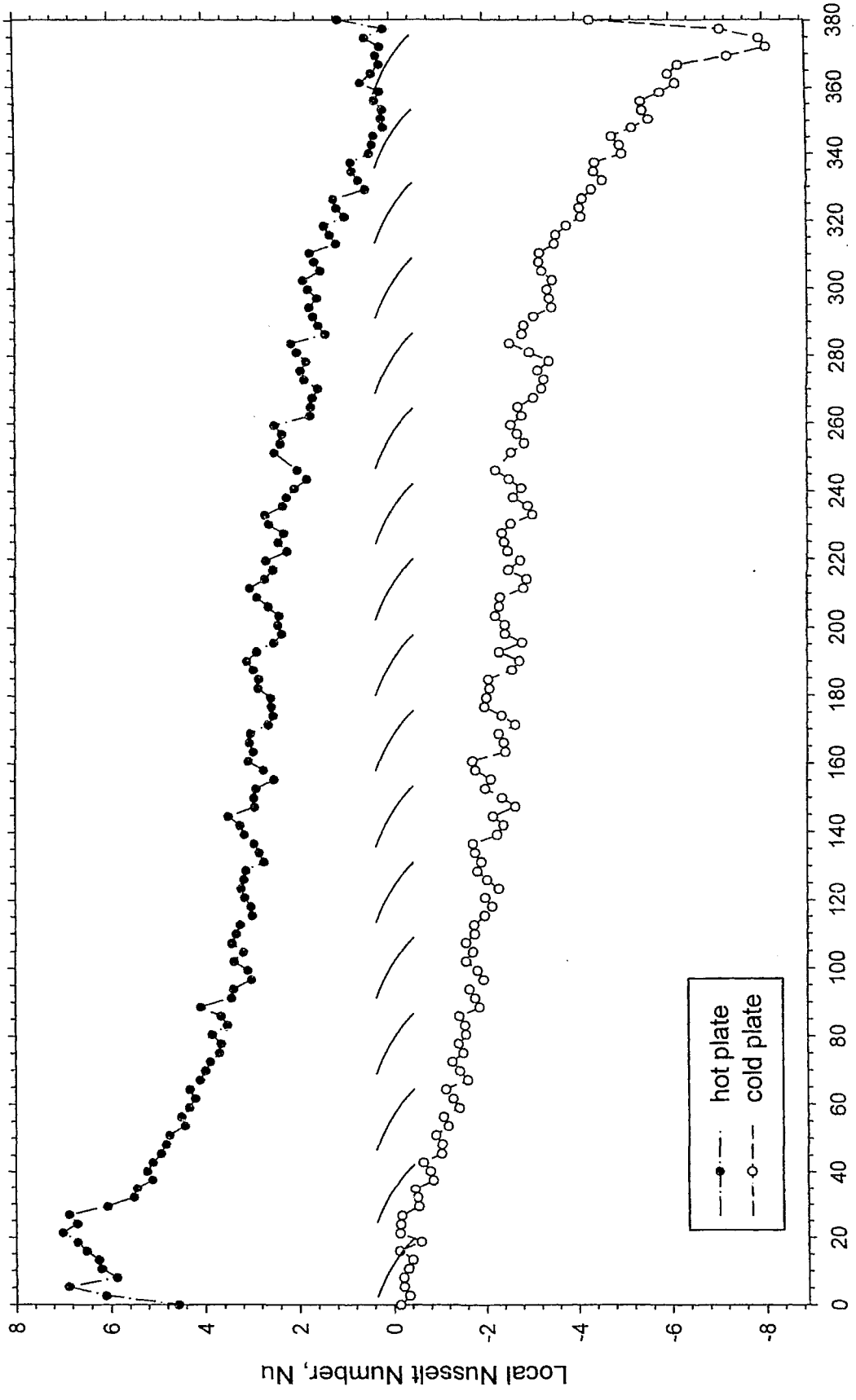

Figure 4.12 Local Nusselt number distribution for $s = 8$mm and $\phi = 45°$ at $Ra \approx 13.1 \times 10^4$

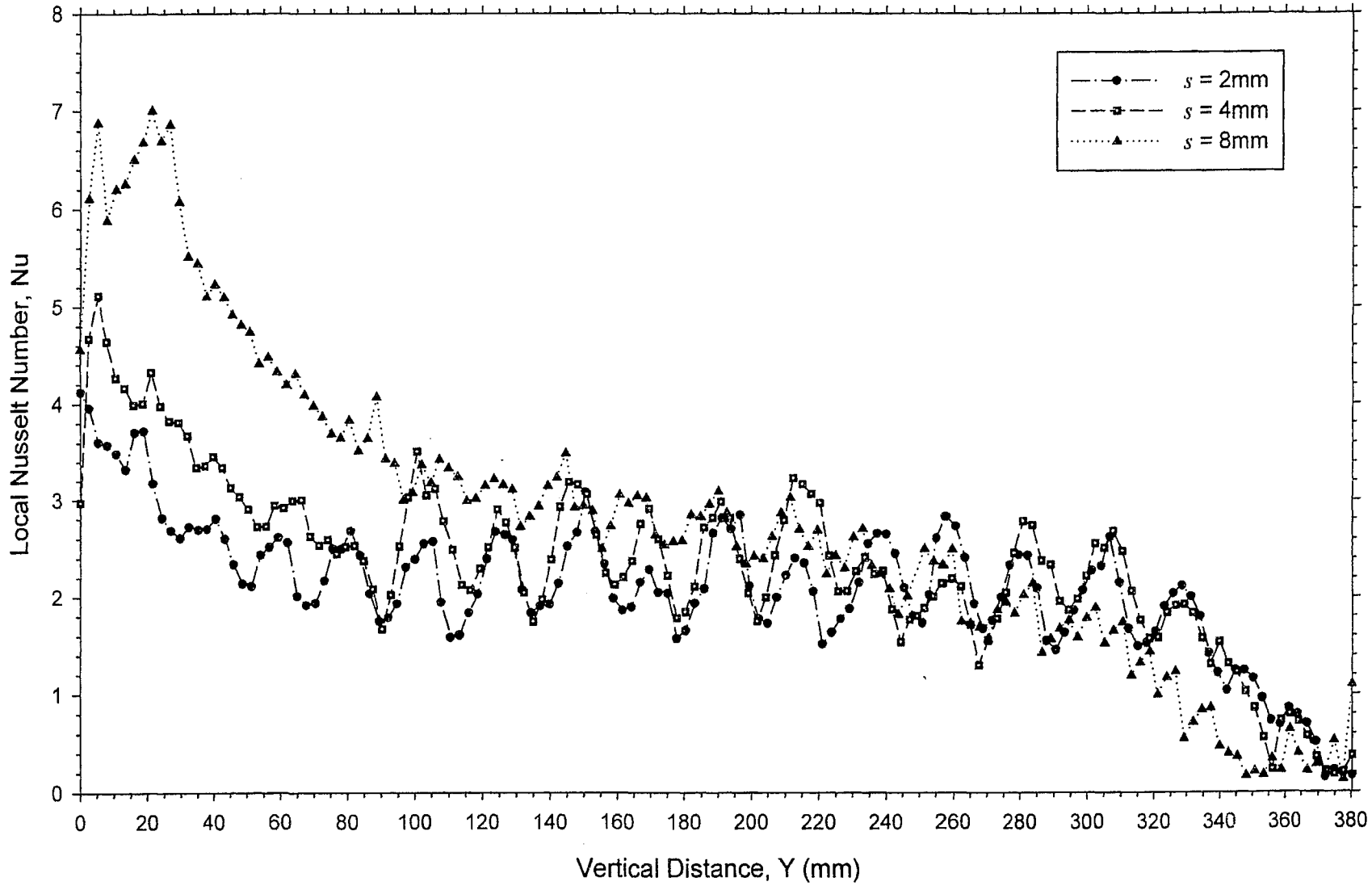

Figure 4.13 Local Nusselt number distributions for $\phi = 45°$ at various s

increases for the hot plate due to the convective effect caused by the stream of cooler air traveling with the outer circulation flow.

In Figures 4.14 to 4.16, the local Nusselt number distribution for the blind slat angle of $\phi = 90°$ at the blind tip-to-plate spacings of $s = 2$mm, $s = 4$mm, and $s = 8$mm are shown, respectively. With the blind at the closed position, the window cavity is separated into two narrow cavities of half the original width. Convective heat transfer is occurring on both the hot and cold plate surfaces to the air within the partitioned cavities. Hence, with the exception of end effects, heat transfer rate remains relatively steady in the centre region of the cavity, with the absence of peaks. Looking at the infinite fringe interferograms in Figure 4.4, the boundary layer growth on the plate surfaces is visible. Specifically, comparing the case of $s = 8$mm with the no blind case in Figure 4.17, the boundary layer flows in the cavity with and without the blind are very much alike.

At this point, it is necessary to identify some features found on the graphs that are caused by imperfections in the manufacture of the experimental model. One must keep in mind that commercial blinds will have similar, likely greater, imperfections. Despite the absence of peaks, there is evidence of fluctuations, particularly near the top and bottom of the enclosure, on the graphs in Figures 4.14 through 4.16. This is the effect of air leakage between the blind slats, which is also evident in Figure 4.4. Although the blind is supposed to be completely closed at the slat angle of $\phi = 90°$, it is not possible to do so in practice. In fact, the experimental model has been designed such that the ends of the slats overlap one another when the blind is closed, which simulates the operation of real commercial blinds. At each position where two slats overlap, there is inevitably a small gap where air can flow through. In retrospect, it may be more useful to study a blind slat angle of, say, $\phi = 85°$.

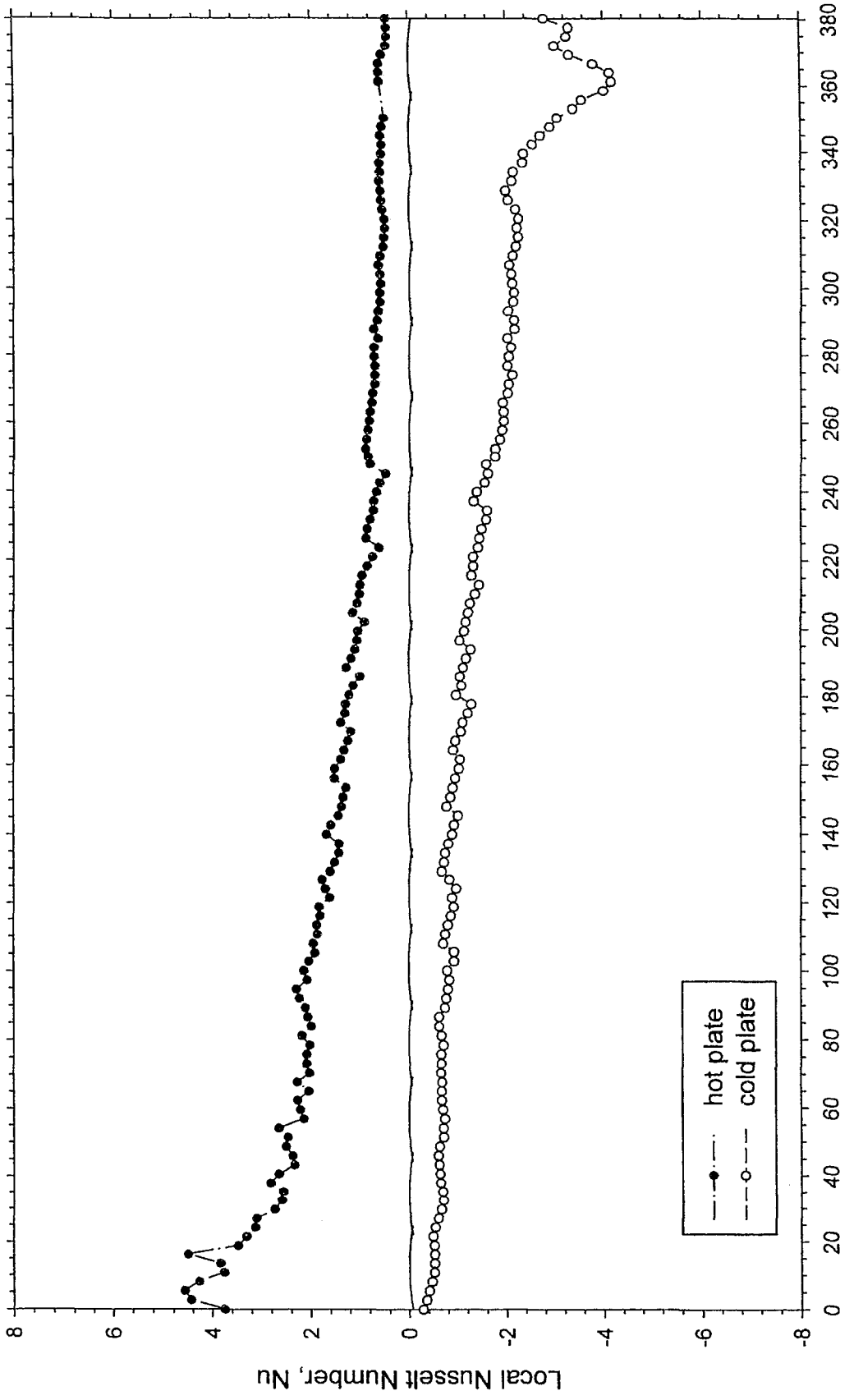

Figure 4.14 Local Nusselt number distribution for $s = 2$mm and $\phi = 90°$ at $Ra \approx 4.5\times10^4$

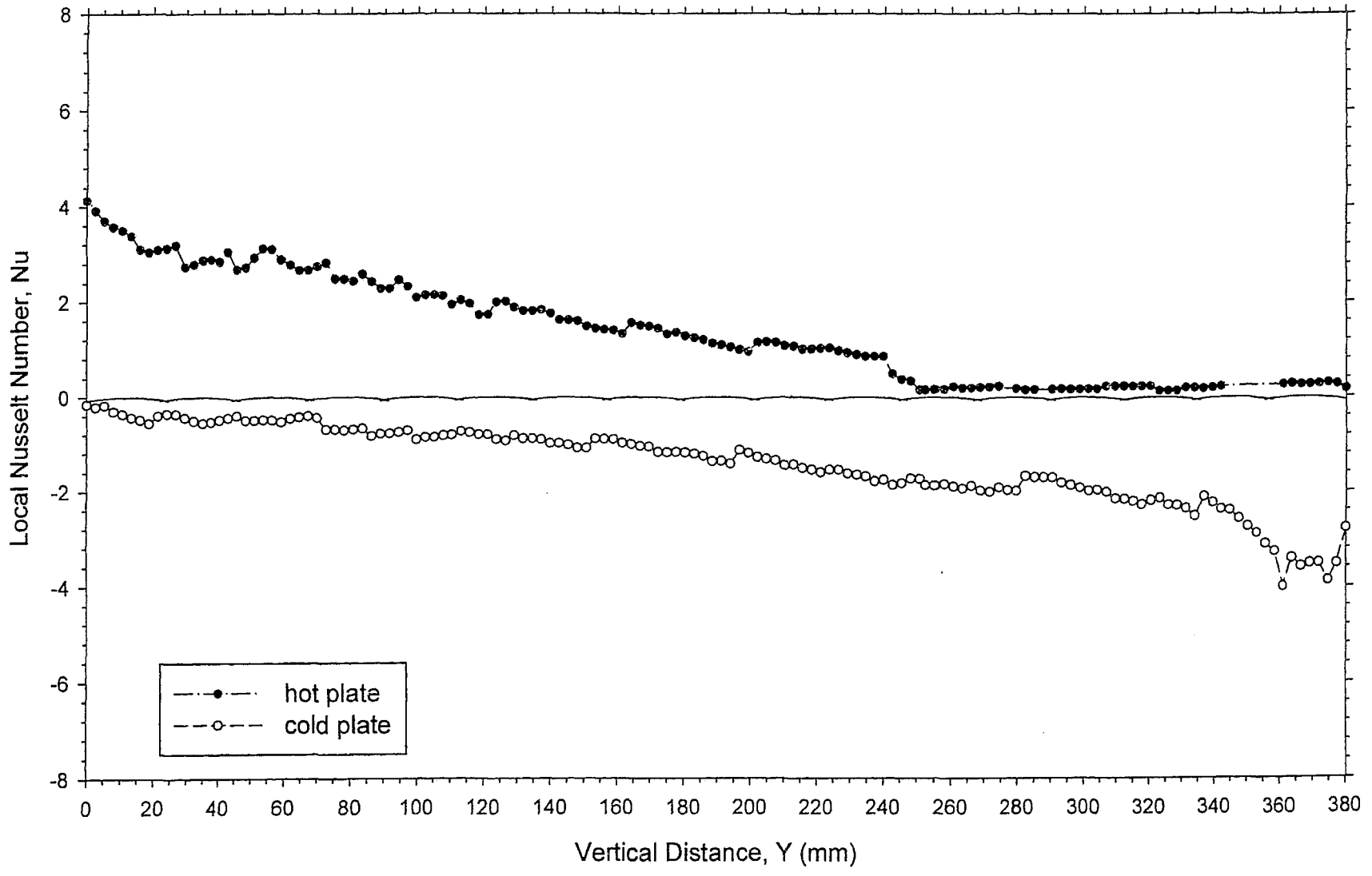

Figure 4.15 Local Nusselt number distribution for $s = 4$mm and $\phi = 90°$ at $Ra \approx 6.7\times10^4$

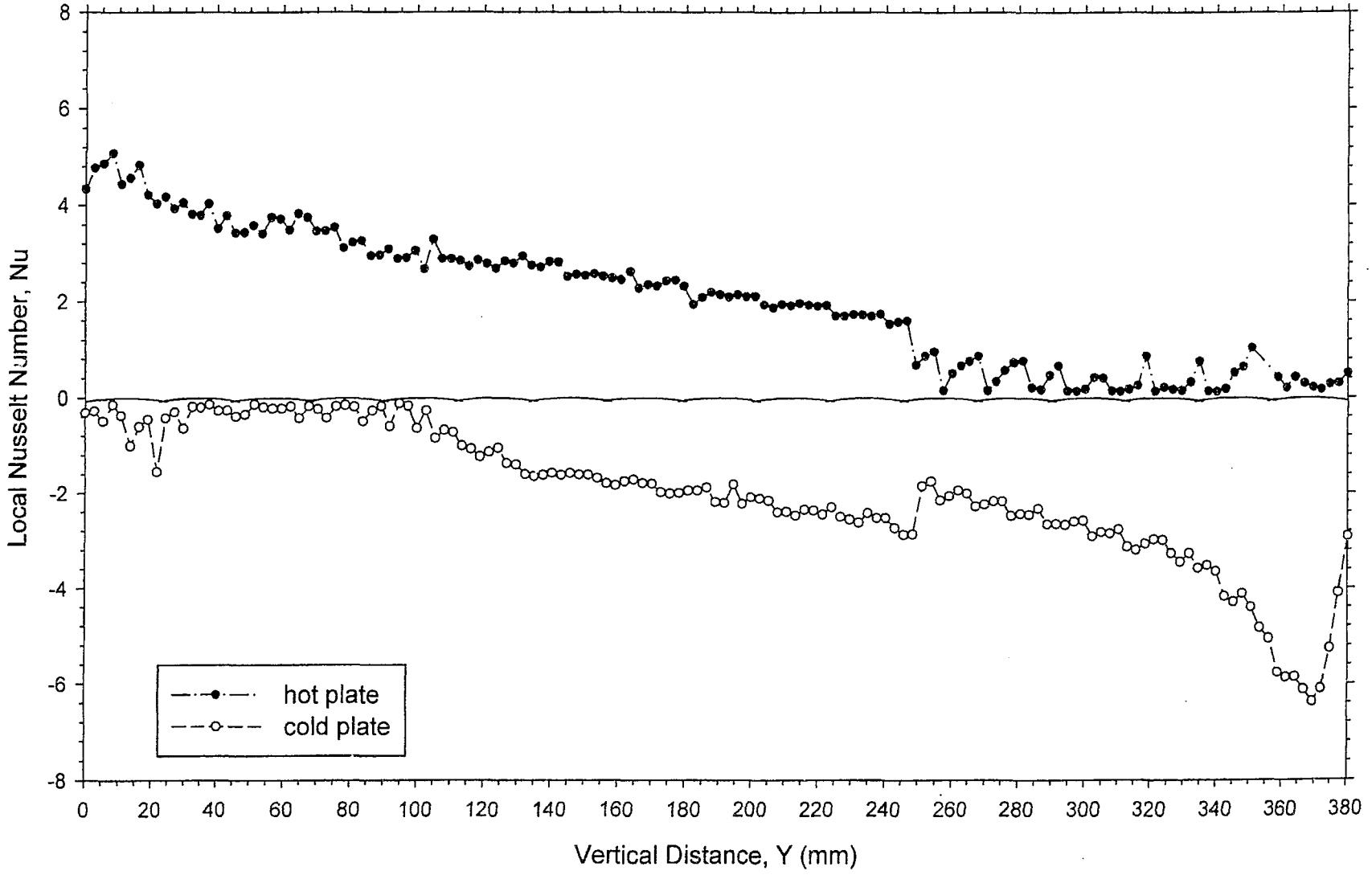

Figure 4.16 Local Nusselt number distribution for s = 8mm and ϕ = 90° at $Ra \approx 13.1\times10^4$

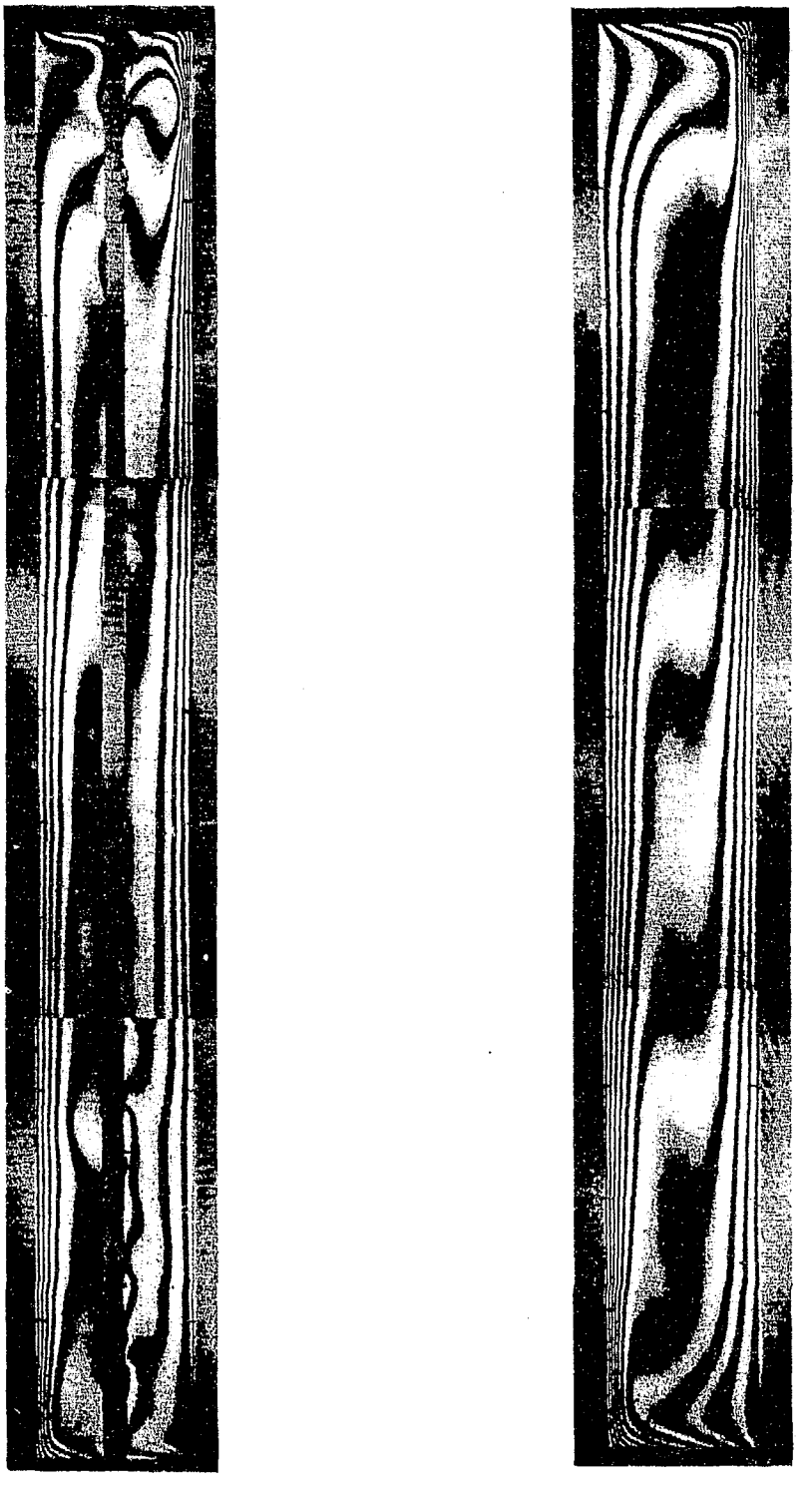

(a) With blind, $\phi = 90°$ (b) Without blind

Figure 4.17 Composite infinite fringe interferograms for $s = 8$mm

In addition, there are small step discontinuities in local Nusselt number found on the graphs in all cases. For example, one case where the discontinuity is obvious is for the blind slat angle of ϕ = 90°, around y = 250mm in Figure 4.16. As mentioned previously, since the interferograms for each case has to be taken in three shots, changes in the state of the test section at different times cannot be avoided. Even though careful measures have been taken, it is hard to control experimental parameters, such as surface temperature of the plates and settings of the optics, to ensure that they are exactly the same between each shot. For this reason, the graphs and composite interferograms may not match perfectly between the different sections of the cavity.

A summary of the average Nusselt numbers for both the hot and cold plates, integrated over the height of the cavity, is presented in Table 4.1 for the nine cases of blind tip-to-plate spacing and blind slat angle. It can be seen that the average Nusselt numbers for the hot and cold plates for the same case differ by from –2.0% to +7.7%. Generally, the hot and cold plate average Nusselt numbers are the same to better than 4%, which is well within the expected level of experimental uncertainty (see Appendix D). Although the main reason for these differences is likely experimental uncertainty, one should also keep in mind that only the convective heat transfer rate is measured in the experiment. Some difference in the hot and cold plate Nusselt numbers can be expected because of: (i) thermal radiation effects, (ii) heat losses/gains at the end walls and optical windows, and (iii) air leakage to/from the enclosure.

Table 4.1 Summary of average Nusselt numbers

s	ϕ	Ra	$Nu_{avg,\,hot}$	$Nu_{avg,\,cold}$	% Diff
2mm	0°	4.5×10^4	2.89	2.73	+5.7
2mm	45°	4.5×10^4	2.13	2.10	+1.2
2mm	90°	4.5×10^4	1.43	1.46	–2.0
4mm	0°	6.7×10^4	2.47	2.35	+5.2
4mm	45°	6.7×10^4	2.36	2.27	+3.9
4mm	90°	6.7×10^4	1.53	1.44	+6.4
8mm	0°	13.1×10^4	2.51	2.59	–0.6
8mm	45°	13.1×10^4	2.81	2.60	+7.7
8mm	90°	13.1×10^4	2.07	2.01	–0.3

The effect of blind slat angle is now examined. In general, for all blind tip-to-plate spacings, the average Nusselt number decreases as blind slat angle increases. This can be easily explained for the blind tip-to-plate spacing of s = 2mm and ϕ = 0°, as shown in Figure 4.18, where the local heat transfer rate is strongly dependent on the conductive effect of the blind slats. As the tips of the slats move away from the plate surfaces at ϕ = 45°, the local heat transfer rates decrease as the conductive effect lessens. When the blind is closed at ϕ = 90°, local heat transfer rates remain relatively low as air circulates primarily within the two separate half-width cavities. At s = 4mm, where the convective outer circulation within the cavity has a more significant effect on heat transfer rate, changing the blind slat angle from ϕ = 0° to ϕ = 45° causes very little change in local Nusselt numbers, which can be seen in Figure 4.19 as the two graphs almost superimpose upon each other. When the blind slat angle goes to ϕ = 90°, however, the local heat transfer rates drop notably as the blind inhibits the outer circulation flow. The trend is similar for the case of s = 8mm.

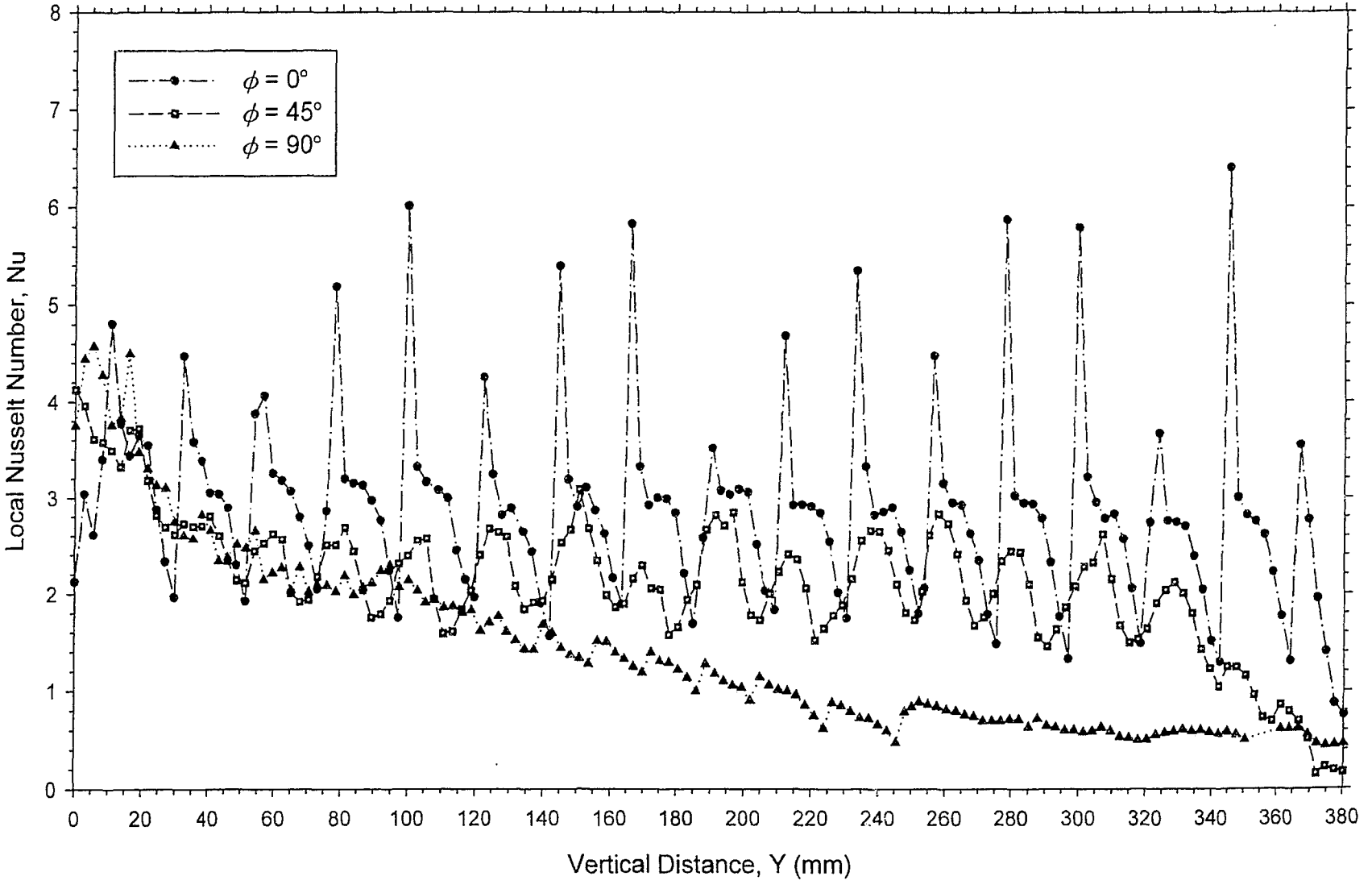

Figure 4.18 Local Nusselt number distributions for s = 2mm at various ϕ

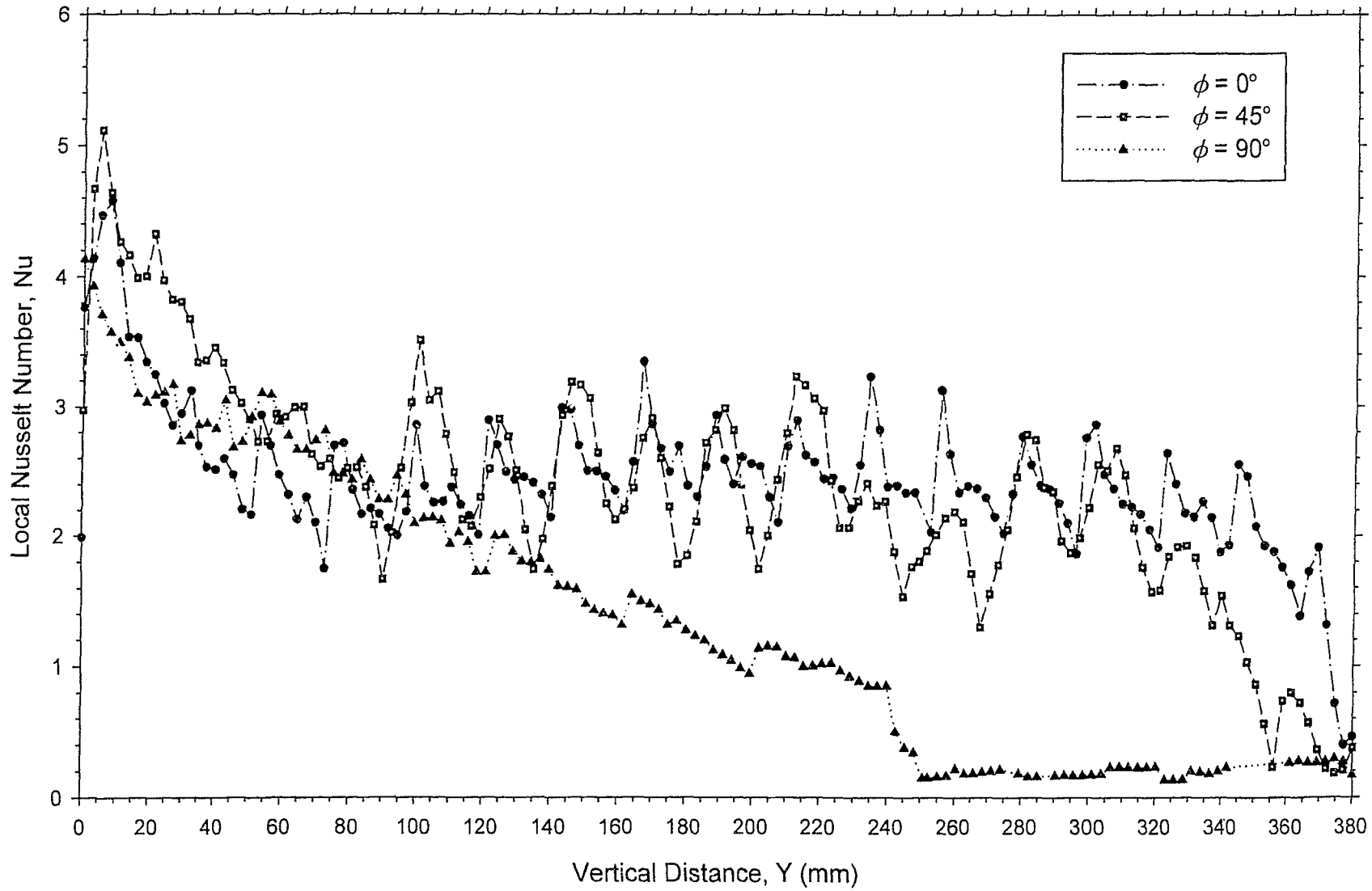

Figure 4.19 Local Nusselt number distributions for s = 4mm at various ϕ

In Figure 4.20, the average Nusselt numbers for the hot plate for all the cases are compared to the cavity correlation by ElSherbiny et al. [14]. Since the correlation applies to an empty cavity without blinds, the graph illustrates the impact on overall heat transfer caused by the presence of blinds. Apparently, except for one case, all the experimental average Nusselt numbers fall below the curves defined by equation (1.2), at the corresponding Rayleigh numbers (Ra) and aspect ratios (A). The results show that the blind can inhibit heat transfer across the cavity, hence, improve the insulating effect of the double-glazed window. With the blind slat angle of $\phi = 90°$, the experimental average Nusselt numbers are lowered by up to 40%. For the case of $\phi = 0°$ at the close blind tip-to-plate spacing of $s = 2$mm, the experimental average Nusselt number is much higher than the theoretical value. This is due mainly to the strong conductive heat transfer across the blind slats, which greatly increases the local heat transfer rates at the slat locations. In this case, the insulation provided by the air space in the window cavity is diminished by the interference of the blind. Nonetheless, in most cases, the between-panes blind is able to enhance the thermal performance of the double-glazed window by suppressing the convective heat transfer across the cavity.

4.4 Reproducibility of the Experiment

To illustrate the reproducibility of the results, one experiment was repeated after a lapse of a few days. The interferogram for the blind tip-to-plate spacing of s = 2mm and blind slat angle of $\phi = 0°$ at the bottom section of the cavity was chosen. The results of the reproducibility test are presented in Figure 4.21.

This experiment was expected to be one of the most difficult to replicate because of the close proximity of the tips of the blind slats to the plate surfaces. Both interferograms were scanned at the same frequency. By inspection, the periodic variation and distribution of local Nusselt numbers was virtually identical. The locations of some maxima and minima were shifted, due probably to the inaccuracy in setting the blade angle, which can cause fluctuations in blind tip-to-plate spacing. The discrepancies in heat transfer data can also be attributed to inconsistent scanning between each interferogram, such as locating fringe centres and the plate surface.

Despite the some dissimilarity in local Nusselt numbers, the average Nusselt numbers of the two experiments changed only slightly ($Nu_{orig.} = 1.086$, $Nu_{repro.} = 1.152$). The experimental uncertainty in local Nusselt number is shown in Appendix D to be about ±7%. This is consistent with the overall difference in average Nusselt number between the original experiment and the reproducibility test.

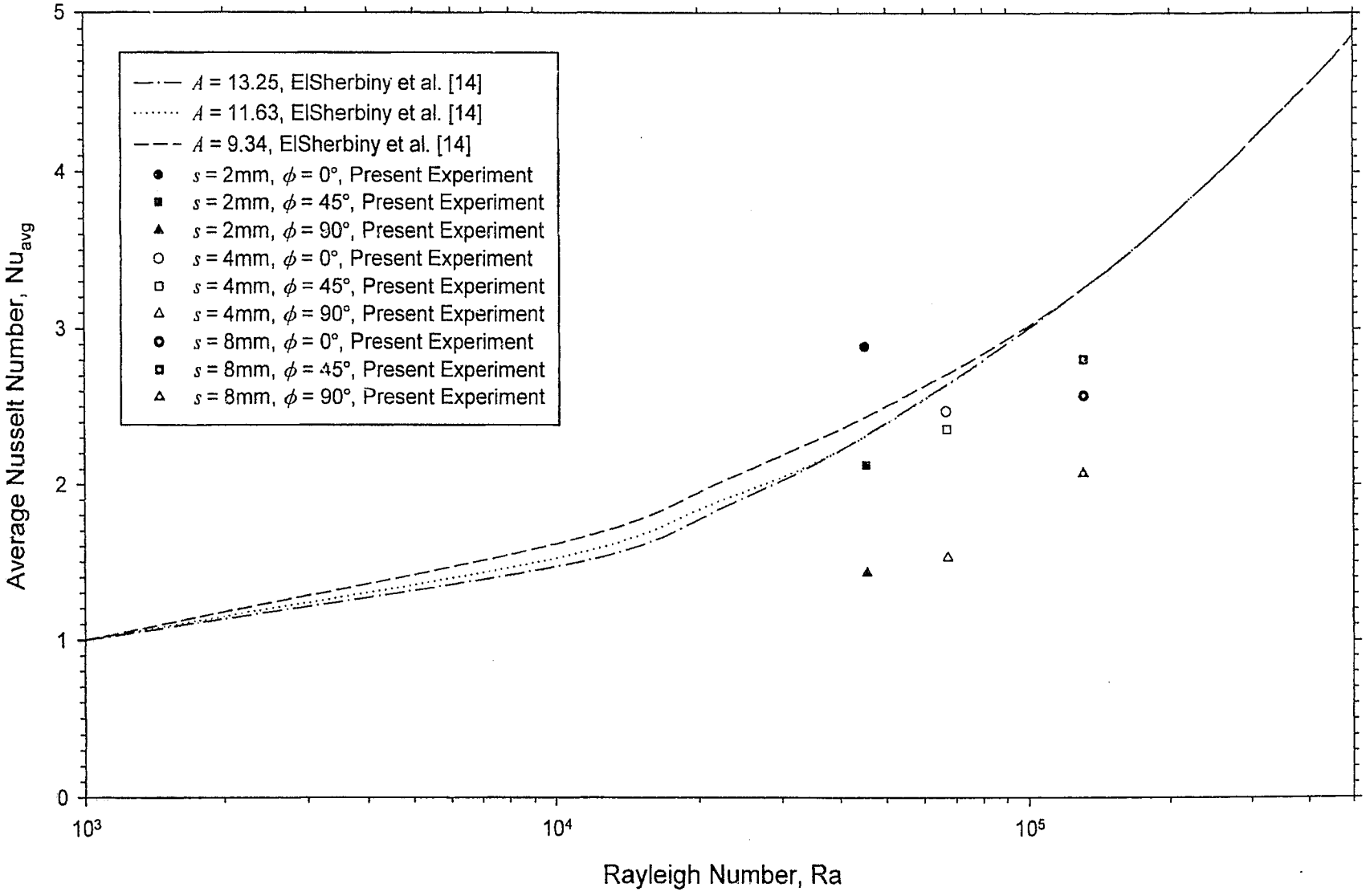

Figure 4.20 Comparison of average Nusselt numbers with cavity correlation

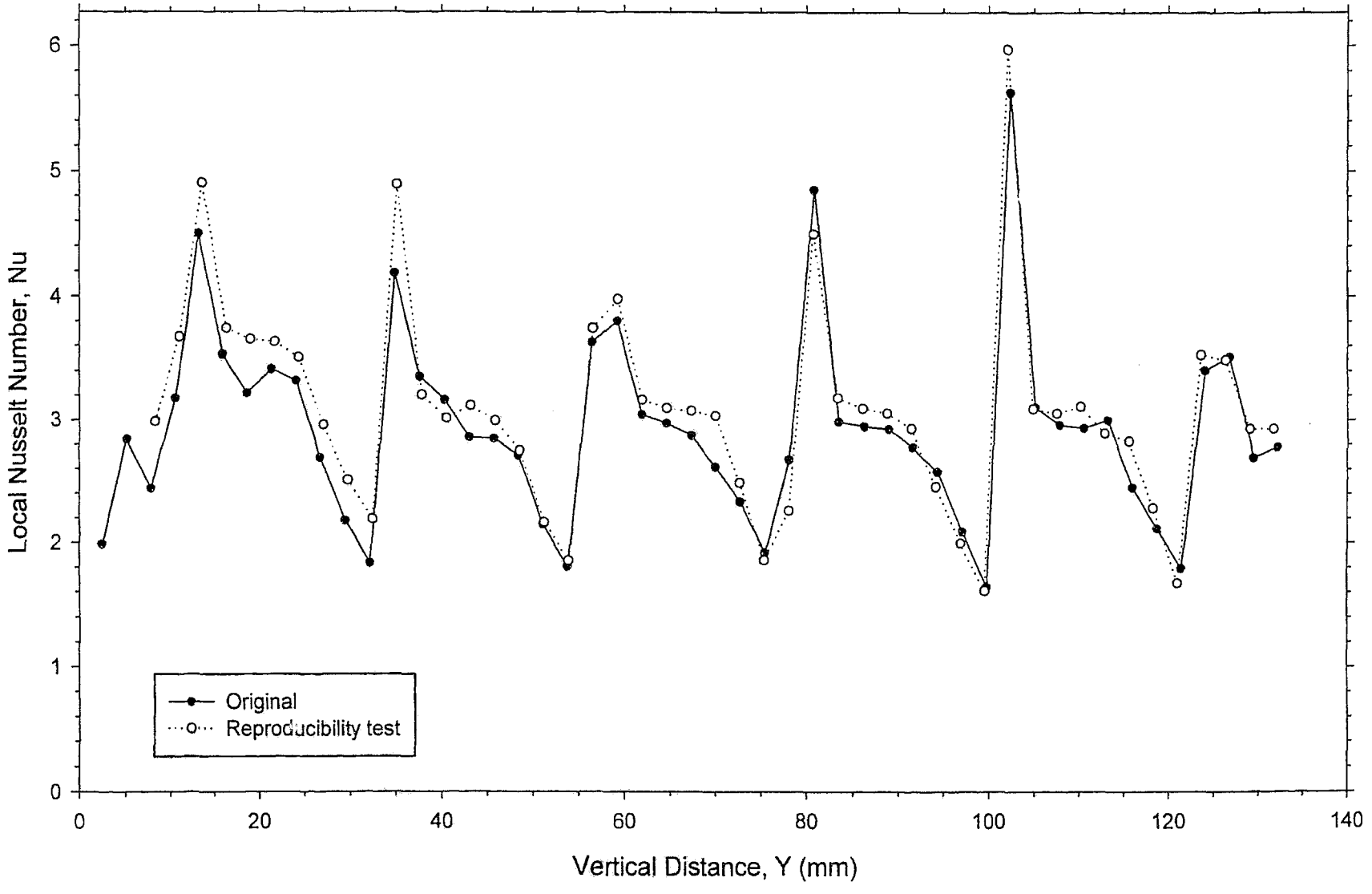

Figure 4.21 Reproducibility test for $s = 2$mm and $\phi = 0°$, bottom section

Chapter 5

NUMERICAL STUDY

5.1 Introduction

In order to predict the heat transfer results to be expected from the interferometric study, a preliminary numerical study was performed during the preparation stage of the experiment. This numerical study was intended to simulate the experimental model that was being developed at the time. Using the commercial CFD software package FIDAP [68], a two-dimensional conjugate conduction/convection numerical model was created to study the free convective heat transfer in a double-glazed window with a between-panes Venetian blind. Since the scope of this numerical study was limited, thermal radiation exchange was not considered in this study. Calculations were obtained for the blind tip-to-plate spacings of s = 2mm, s = 4mm, and s = 8mm, and at blind slat angles of $\phi = 0°$, $\phi = 45°$, and $\phi = 90°$ from the horizontal. Several parameters were held constant, such as the Prandtl number at Pr = 0.7 to model air in the cavity. The solid to air conductivity ratio was set as 4600, corresponding to aluminum blind slats. The dimensionless height of the window, or the aspect ratio of the cavity, was fixed at A = 13.22, 11.61, and 9.33 for s = 2mm, 4mm, and 8mm, respectively. Local Nusselt number data were generated in the range of $10^3 \leq Ra \leq 5\times10^5$, as well as temperature and stream function contours for visualization. The findings of this numerical study were published at CANCAM03 (Canadian Congress of Applied Mechanics) [69]. In this chapter, these results are compared to those obtained from the experiment.

5.2 Numerical Model

5.2.1 Model Geometry

The numerical study examines the natural convective heat transfer within a double-glazed window with between-panes Venetian blind. The problem geometry is shown in Figure 5.1. The hot and cold glazing surfaces are isothermal at temperatures T_h and T_c, respectively, while the top and bottom horizontal end walls are adiabatic. The height of the window, L, contains a total of seventeen blind slats. Taking into account the curvature of the blind slat, the nominal blind-to-plate spacing, b, is re-adjusted at each blind slat angle, ϕ, so that the blind tip-to-plate spacing (set from the $\phi = 0°$ position), s, is the same on both sides.

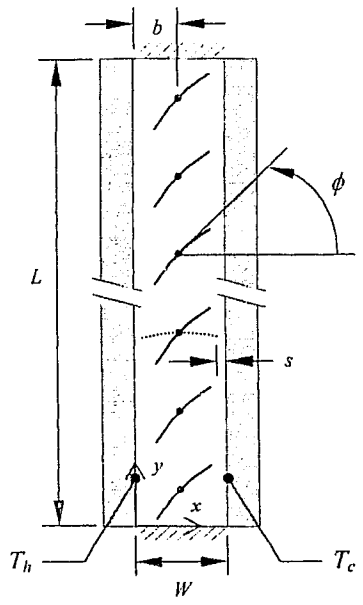

Figure 5.1 Numerical model geometry

5.2.2 Governing Equations and Solution Procedure

The flow is assumed to be two-dimensional, steady, laminar, and incompressible. Thermophysical properties are assumed to be constant, except for fluid density which is treated with the Boussinesq approximation. The dimensionless continuity, momentum, and energy equations [70] for the fluid are:

$$\frac{\partial U}{\partial X}+\frac{\partial V}{\partial Y}=0 \tag{5.1}$$

$$Gr^{1/2}\left(U\frac{\partial U}{\partial X}+V\frac{\partial U}{\partial Y}\right)=-\frac{\partial P}{\partial X}+\left(\frac{\partial^2 U}{\partial X^2}+\frac{\partial^2 U}{\partial Y^2}\right) \tag{5.2}$$

$$Gr^{1/2}\left(U\frac{\partial V}{\partial X}+V\frac{\partial V}{\partial Y}\right)=-\frac{\partial P}{\partial Y}+\left(\frac{\partial^2 V}{\partial X^2}+\frac{\partial^2 V}{\partial Y^2}\right)+Gr^{1/2}\theta \tag{5.3}$$

$$PrGr^{1/2}\left(U\frac{\partial \theta}{\partial X}+V\frac{\partial \theta}{\partial Y}\right)=\frac{\partial^2 \theta}{\partial X^2}+\frac{\partial^2 \theta}{\partial Y^2} \tag{5.4}$$

where the dimensionless variables are defined as follows:

$$X=\frac{x}{W},\ Y=\frac{y}{W},\ U=\frac{u}{U_{ref}},\ V=\frac{v}{U_{ref}}$$

$$U_{ref}=\frac{\alpha PrGr^{1/2}}{W},\ \theta=\frac{T-T_c}{T_h-T_c} \tag{5.5}$$

$$p'=p-p_\infty,\ P=\frac{p'W}{\mu U_{ref}}$$

and the Rayleigh number based on cavity width is:

$$\mathrm{Ra}=\frac{\rho\beta(T_h-T_c)W^3}{\nu\alpha} \tag{5.6}$$

Steady conduction in the solid blind slats is modeled by Laplace's equation:

$$\frac{\partial^2\theta}{\partial X^2}+\frac{\partial^2\theta}{\partial Y^2}=0 \tag{5.7}$$

The dimensionless boundary conditions are as follows:

$$U=V=0,\ \theta=1 \qquad \text{for } X=0,\ 0\le Y\le \frac{L}{W}$$

$$U=V=0,\ \theta=0 \qquad \text{for } X=1,\ 0\le Y\le \frac{L}{W} \tag{5.8}$$

$$U=V=0,\ \frac{\partial\theta}{\partial Y}=0 \qquad \text{for } 0\le X\le 1,\ Y=0,\ \frac{L}{W}$$

Equations (5.1) through (5.7) are solved subject to the boundary conditions specified in (5.7) using the finite element method [71]. Nine-node quadrilateral elements with biquadratic interpolation functions are used for temperature and velocity. Pressure is eliminated from the momentum equations using the penalty formulation [72]. The discretized equations are solved using successive substitution to speed convergence. Based on a grid sensitivity study that has been conducted, a mesh of approximately 40,000 nodes is used.

5.3 Numerical Results

A comparison of the temperature contours for $\phi = 0°$ and the three blind tip-to-plate spacings of s = 2mm, s = 4mm, and s = 8mm at $Ra = 4\times10^4$, $Ra = 4\times10^4$, and $Ra = 10\times10^4$, respectively from the numerical study with the infinite fringe interferograms taken at $Ra \approx 4.5\times10^4$, $Ra \approx 6.7\times10^4$, and $Ra \approx 13.1\times10^4$, respectively from the experiment is given in Figure 5.2.

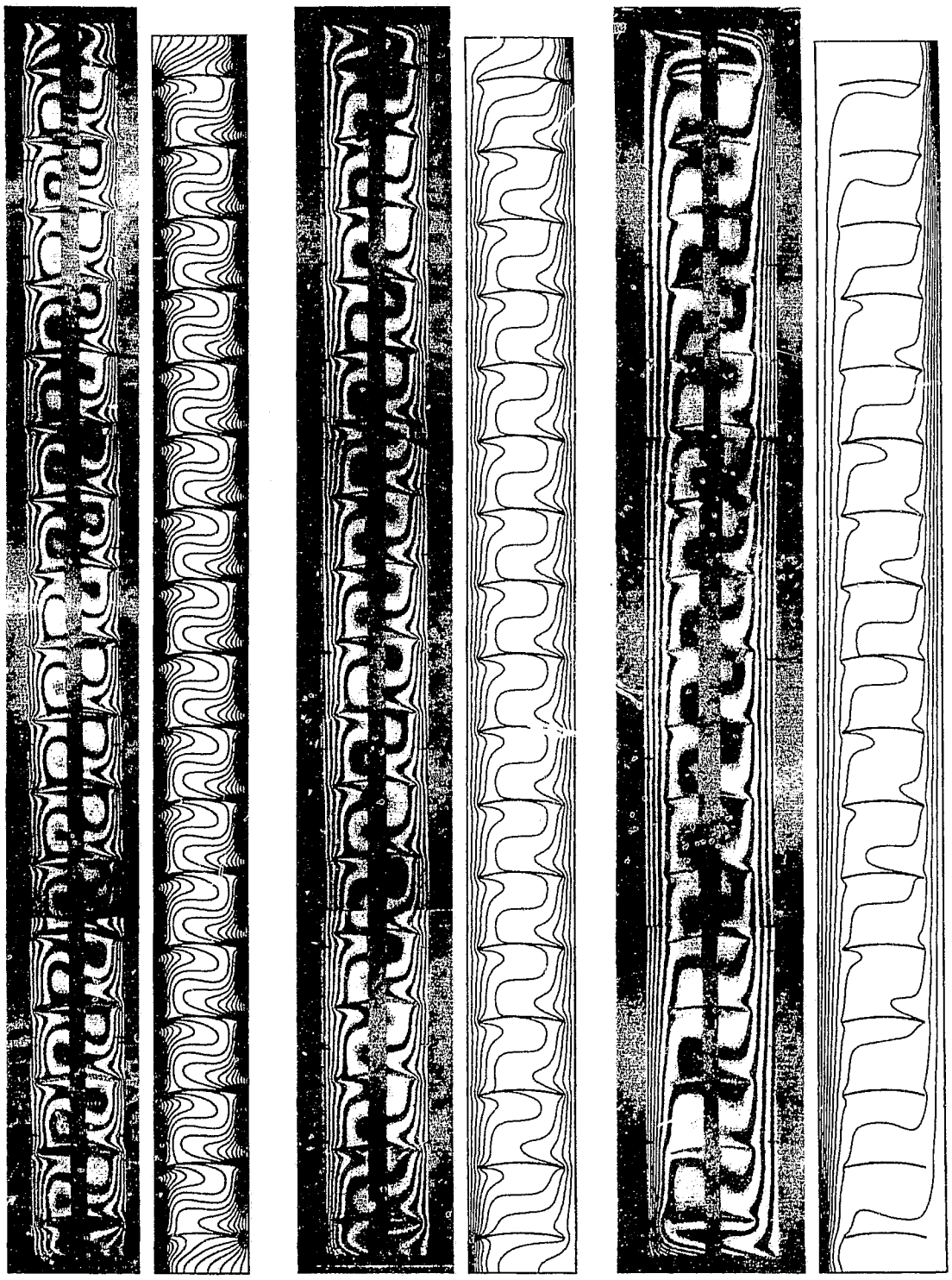

(a) $s = 2$mm (b) $s = 4$mm (c) $s = 8$mm

Figure 5.2 Comparison of temperature contours for $\phi = 0°$ at various s

Since the parameters for the numerical study were set before the experiment was carried out, the Rayleigh numbers were close to, but not exactly the same as those of the experiment. Also, as mentioned in Chapter 4, the fringes on the infinite fringe interferograms might not represent the exact location of the actual isotherms. Despite these discrepancies, the temperature fields show excellent qualitative agreement.

Figure 5.3 shows a comparison of local Nusselt numbers for s = 2mm and $\phi = 0°$ at $Ra = 4\times10^4$ from the numerical study with the experimental results at $Ra \approx 4.5\times10^4$. All local Nusselt number comparisons are presented for the hot plate. The numerical and experimental heat transfer distributions are generally consistent, with the exception of some peaks. This may be due to the fact that in the experimental model, the blind slats cannot be all perfectly set to the tip-to-plate spacing of s = 2mm. With the blind tips so close to the plate surface, the heat transfer rate is greatly affected by the slight deviation in tip-to-plate spacing, producing variation in the peak values.

When the blind tip-to-plate spacing is increased to s = 4mm for the same $\phi = 0°$, as shown in Figure 5.4 the variation in the peak values diminishes. Although the closest numerical Rayleigh number that can be used is $Ra = 4\times10^4$ compared to the experimental $Ra \approx 6.7\times10^4$, the local Nusselt number data agree well. However, the numerical solution overpredicts the heat transfer at the bottom of the hot plate. In the numerical model the end walls are treated as adiabatic, but in the experimental model there are heat losses happening at the end walls, which may contribute to the reduced convective heat transfer rates. This difference is also visible when comparing the numerical results at $Ra = 10\times10^4$ with the experimental results at $Ra \approx 13.1\times10^4$ for s = 8mm and $\phi = 0°$, shown in Figure 5.5.

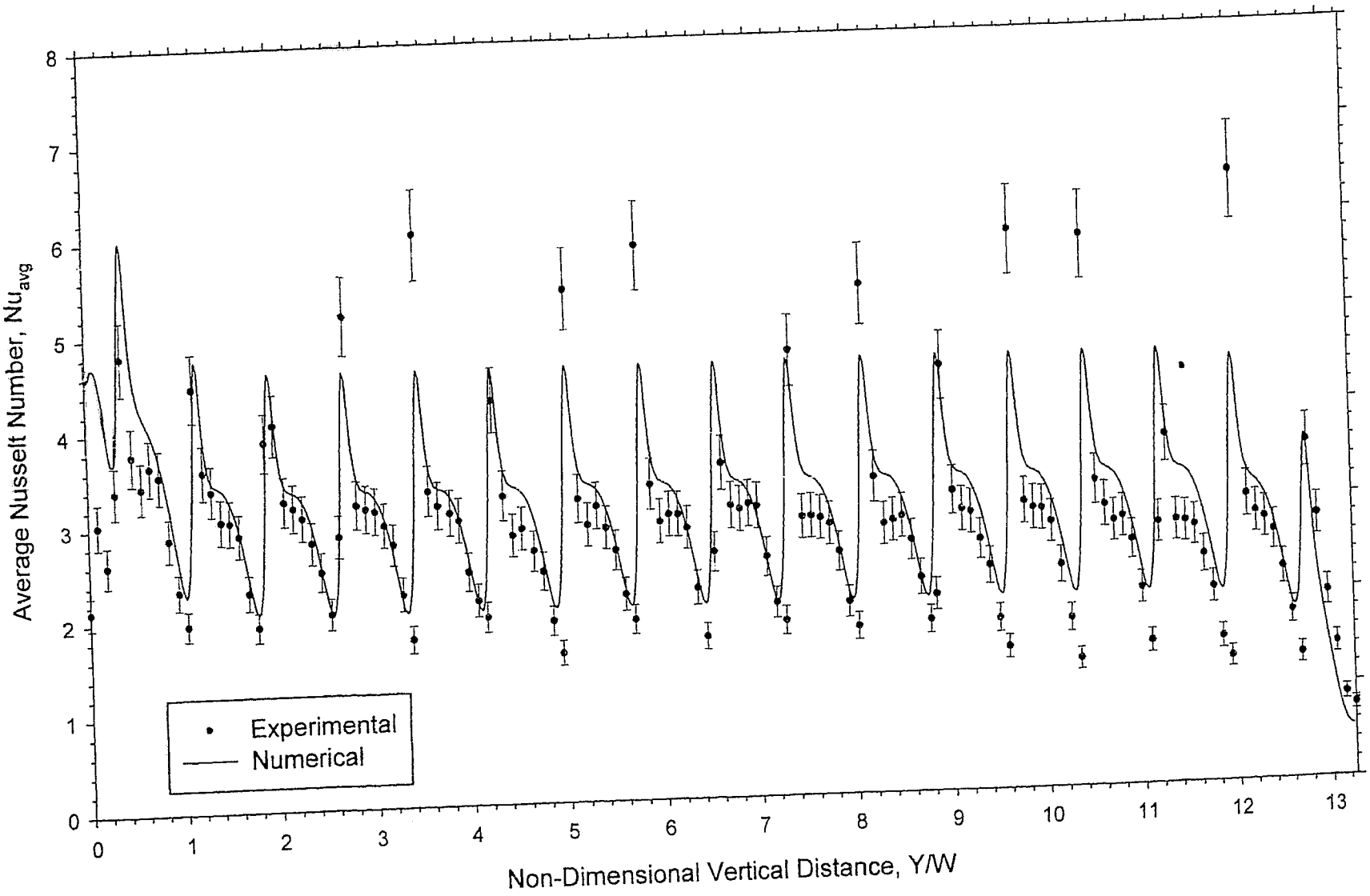

Figure 5.3 Comparison of local Nusselt number distribution for s = 2mm and $\phi = 0°$

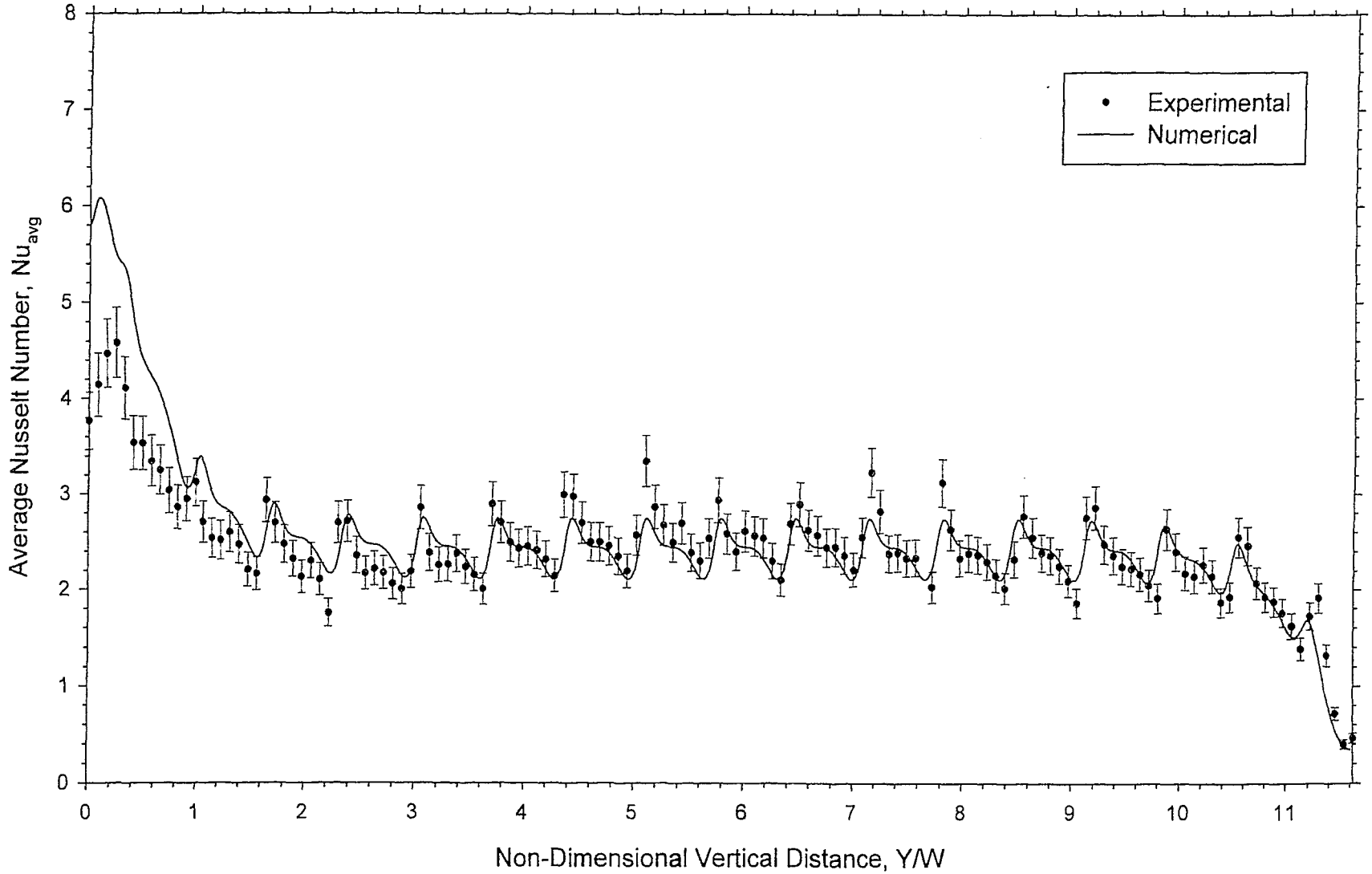

Figure 5.4 Comparison of local Nusselt number distribution for s = 4mm and $\phi = 0°$

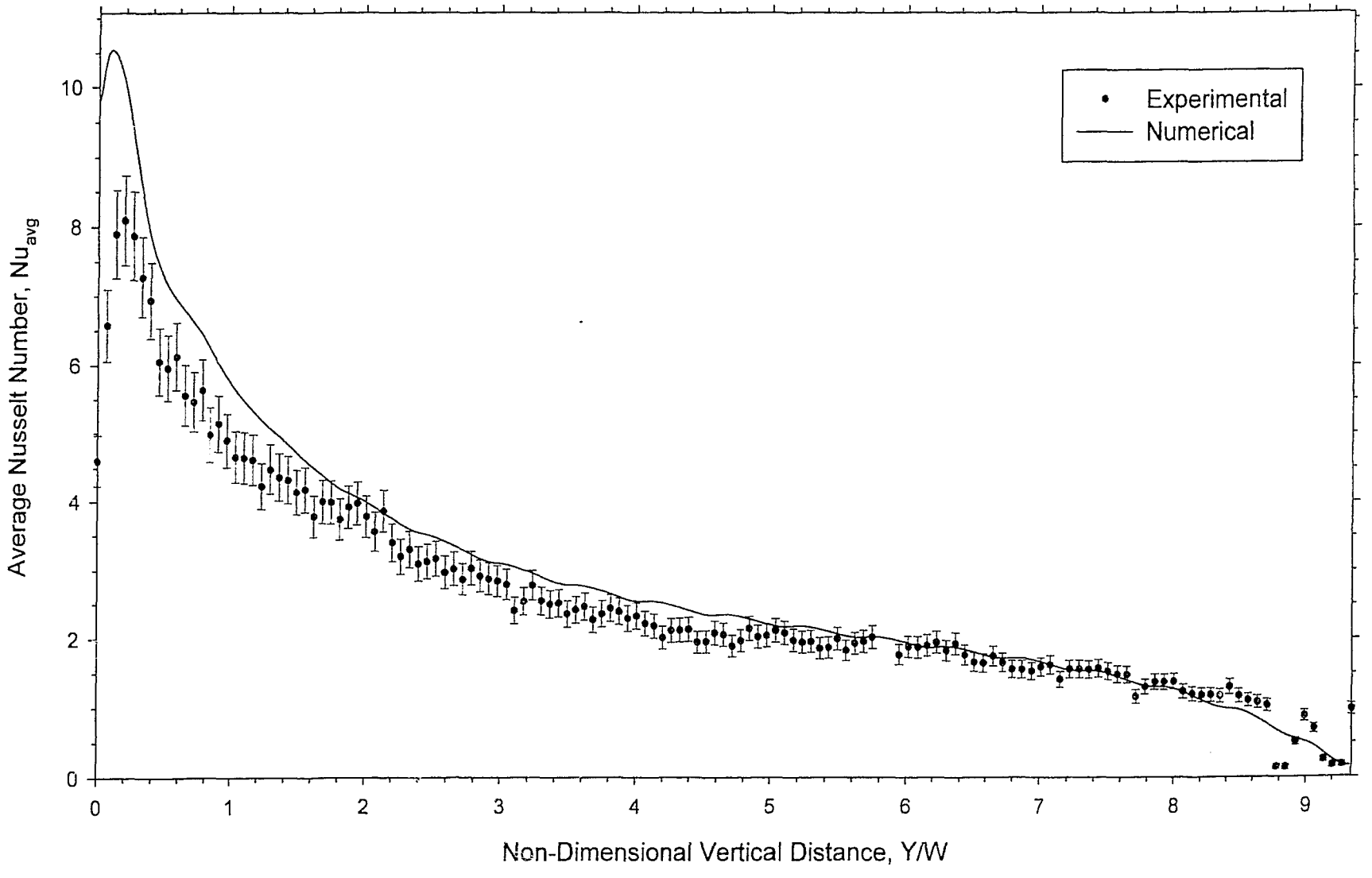

Figure 5.5 Comparison of local Nusselt number distribution for s = 8mm and $\phi = 0°$

A comparison of local Nusselt numbers for s = 2mm and $\phi = 45°$ at $Ra = 4\times10^4$ from the numerical study with the experimental results at $Ra \approx 4.5\times10^4$ is given in Figure 5.6. For this slat angle, the locations of the maximum and minimum local Nusselt numbers are completely mismatched between the numerical and experimental results. Looking at the isotherms shown in Figure 5.7, the numerical model predicts the maximum heat transfer occurring at the slat locations, where the tips of the slat impinge into the boundary layer of the hot and cold plates. By contrast, the infinite fringe interferogram shows the maximum heat transfer occurring in the space between each blind slat. The strong inner circulation flow between the slats is interacting with the outer circulation flow, and in effect, is pushing the boundary layer towards the plate surface. Apparently, analyzing the streamline plot in Figure 5.7, the numerical solution is unable to pick up this phenomenon.

For reasons discussed in Chapter 4, the imperfections in the experimental model at $\phi = 90°$ cause leakage between blind slats. Thus, a valid comparison cannot be made with the numerical results, which ideally models the blind as completely closed. Figure 5.8 shows the isotherm and streamline plots at $Ra = 10\times10^4$, along with the infinite fringe interferogram at $Ra \approx 13.1\times10^4$ for s = 8mm and $\phi = 90°$. In this case, one can clearly see the jets of air leaking between the blind slats near the top of the experimental model, whereas the numerical model portrays the blind as an impermeable membrane with absolutely no leakage. The numerical local Nusselt numbers obtained at $Ra = 4\times10^4$ with the experimental data taken at $Ra \approx 4.5\times10^4$ for s = 2mm and $\phi = 90°$ are presented in Figure 5.9. The periodicity of the numerical results is due to disturbances caused by the slight curvature in the shape of the closed blind slats. The experimental results show leakage through the blind slats.

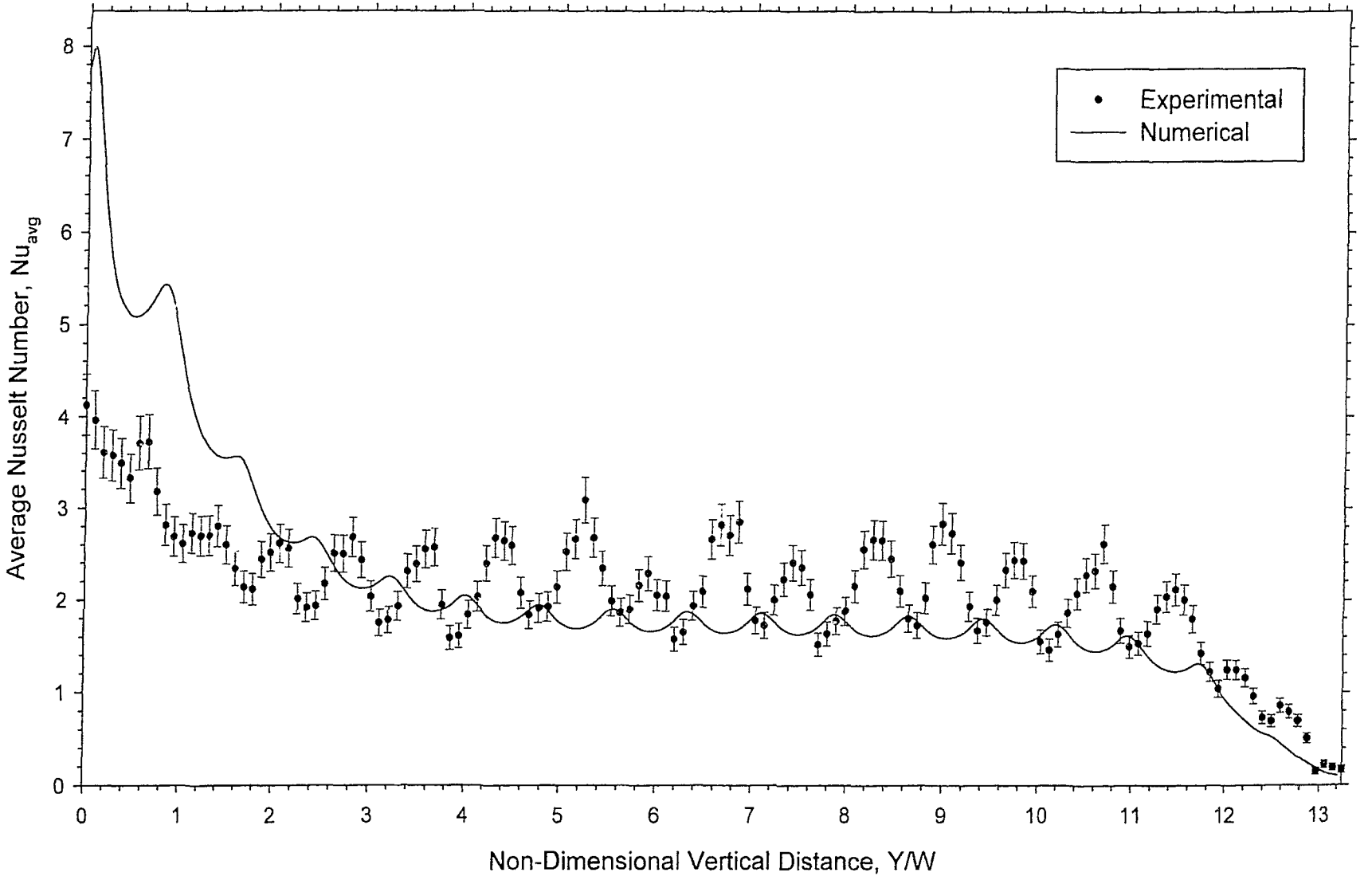

Figure 5.6 Comparison of local Nusselt number distribution for s = 2mm and $\phi = 45°$

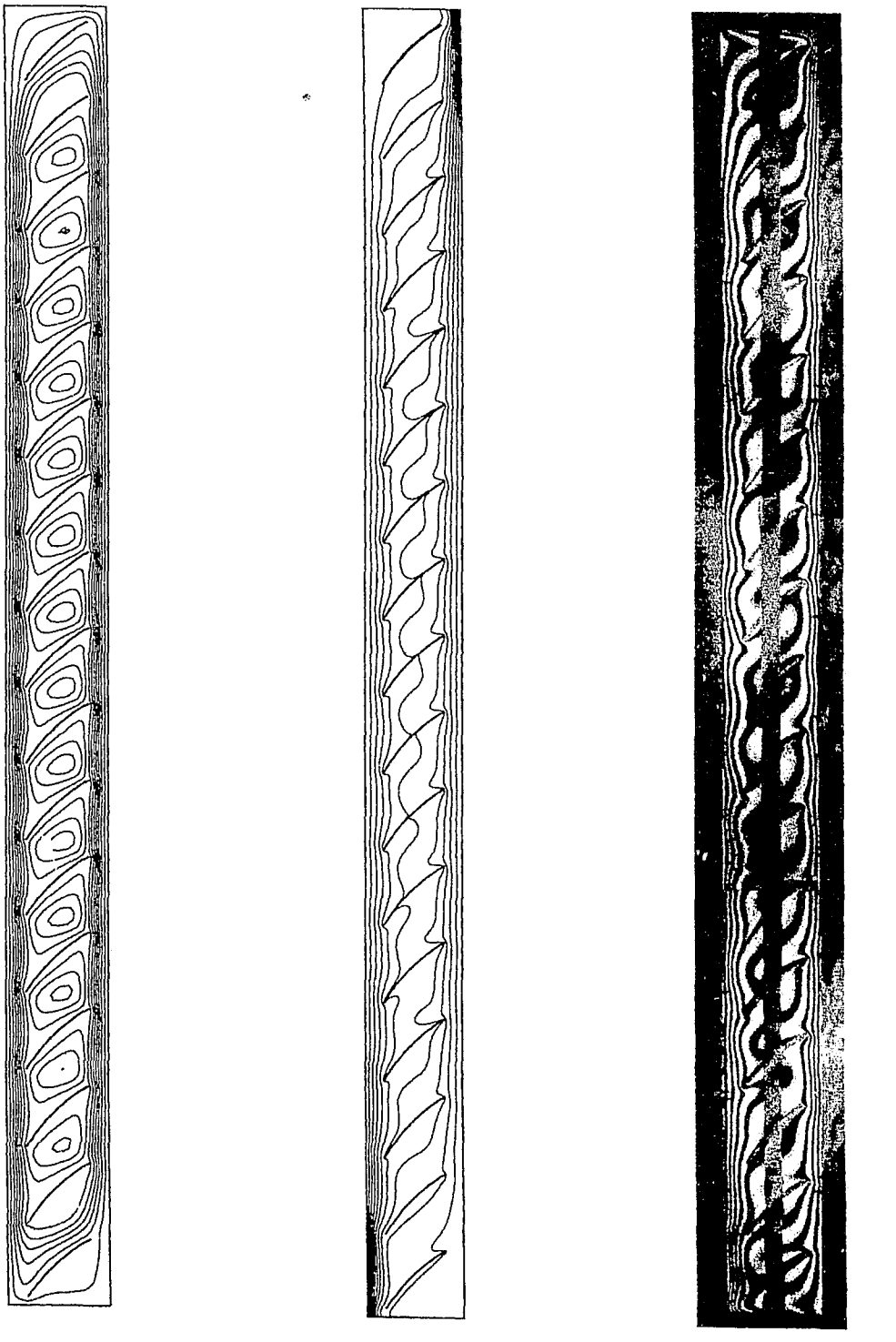

(i) streamlines (ii) isotherms (iii) interferogram

Figure 5.7 Comparison of stream and temperature contours with infinite fringe interferogram for $s = 2$mm and $\phi = 45°$

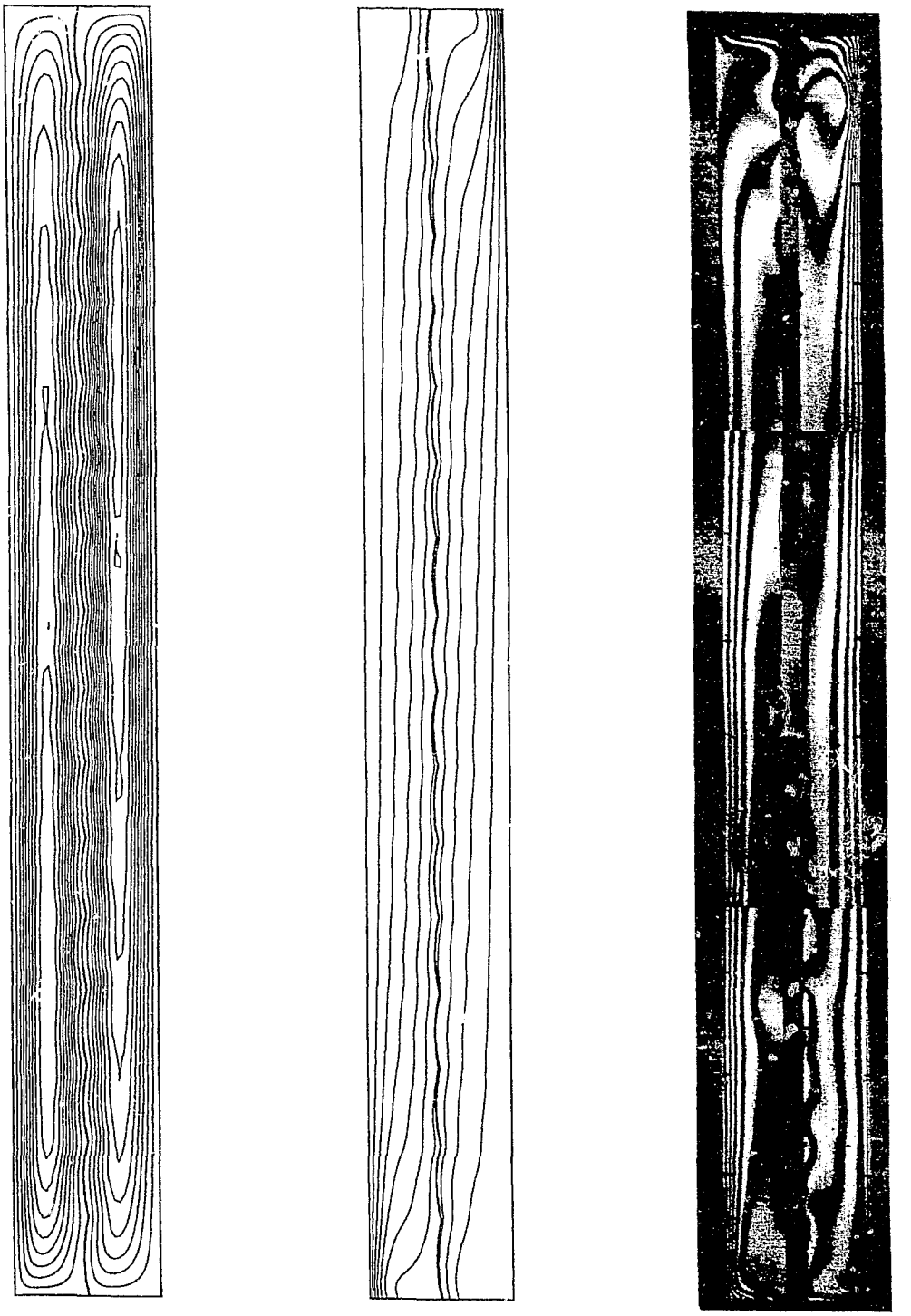

(i) streamlines (ii) isotherms (iii) interferogram

Figure 5.8 Comparison of stream and temperature contours with infinite fringe interferogram for $s = 8$mm and $\phi = 90°$

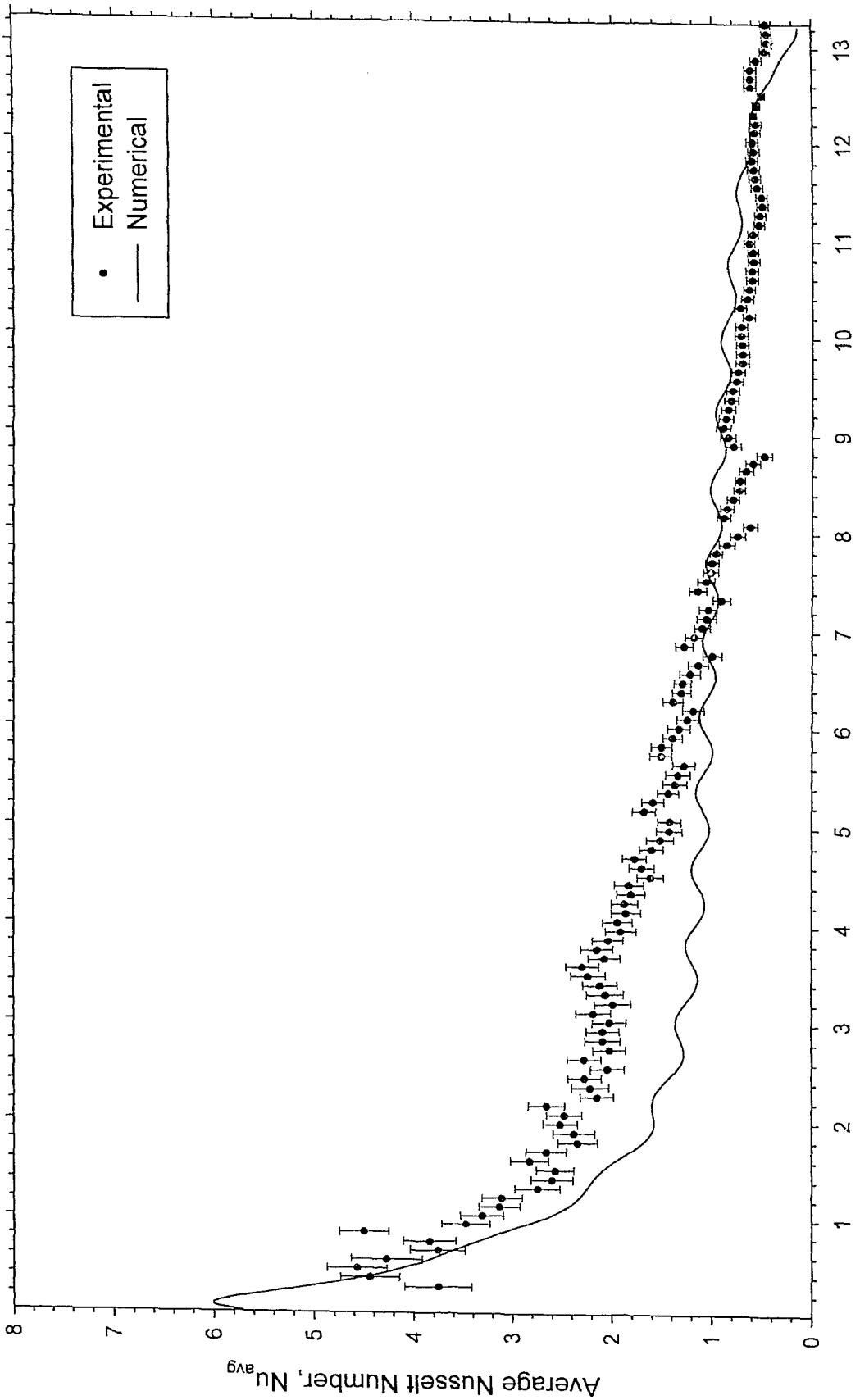

Figure 5.9 Comparison of local Nusselt number distribution for $s = 2$mm and $\phi = 90°$

In Figure 5.10, the average Nusselt numbers for $\phi = 90°$ and the three blind tip-to-plate spacings at the experimental Rayleigh numbers of $Ra \approx 4.5\times10^4$, $Ra \approx 6.7\times10^4$, and $Ra \approx 13.1\times10^4$ are compared to the average Nusselt numbers obtained numerically over a range of Rayleigh numbers. The leakage occurring between the blind slats in the experimental model causes a huge increase in the local heat transfer rates, especially near the top of the cold plate and bottom of the hot plate. In addition, with the blind completely sealing the window cavity, the numerical model effectively calculates the local heat transfer rates on the hot and cold side as two separate cavities with half the original width. Therefore, the numerical average Nusselt numbers are much lower than the experimental average Nusselt numbers for this particular slat angle.

Comparing the average Nusselt numbers for $\phi = 0°$ and $\phi = 45°$ at the three blind tip-to-plate spacings in Figures 5.11 and 5.12, respectively, the experimental results are consistently lower than the numerical values. Knowing that the local heat transfer data agrees fairly well in these cases (certainly for $\phi = 0°$, and for $\phi = 45°$ though not in distribution but in magnitude), except near the bottom of the hot plate and top of the cold plate, the difference in average Nusselt numbers can be attributed to end wall heat losses in the experimental model. If these end wall conditions can be reasonably modeled in the numerical study, it may improve agreement.

Most importantly, it must be kept in mind that this numerical study is performed on a conjugate conduction/convection model, with radiation neglected. As Phillips [38] found, convection is strongly coupled to the radiation exchange between the window and the blind. It is likely that the discrepancies in numerical and experimental average Nusselt numbers are due, for the most part, to this effect.

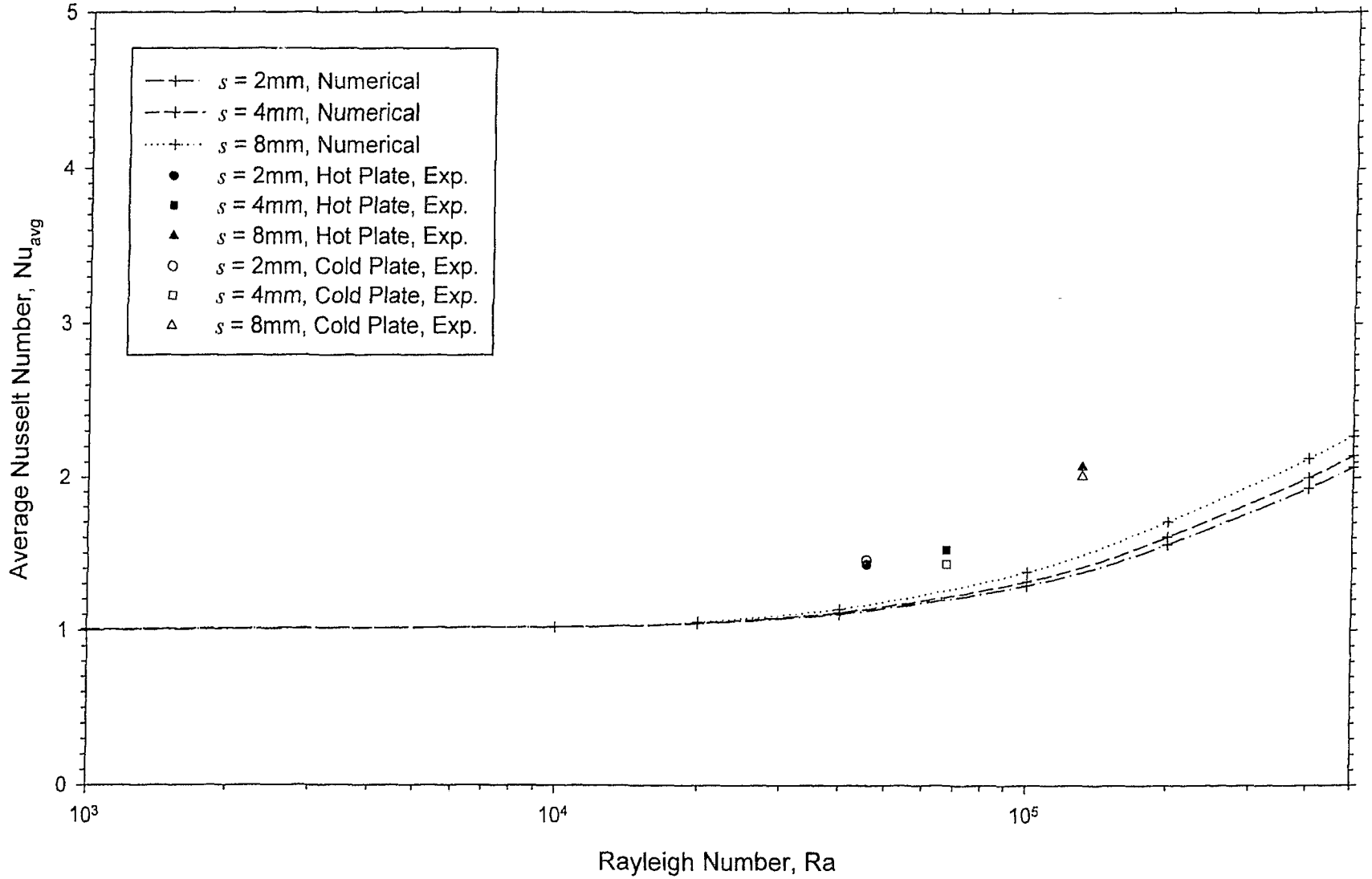

Figure 5.10 Comparison of numerical and experimental average Nusselt numbers for $\phi = 90°$

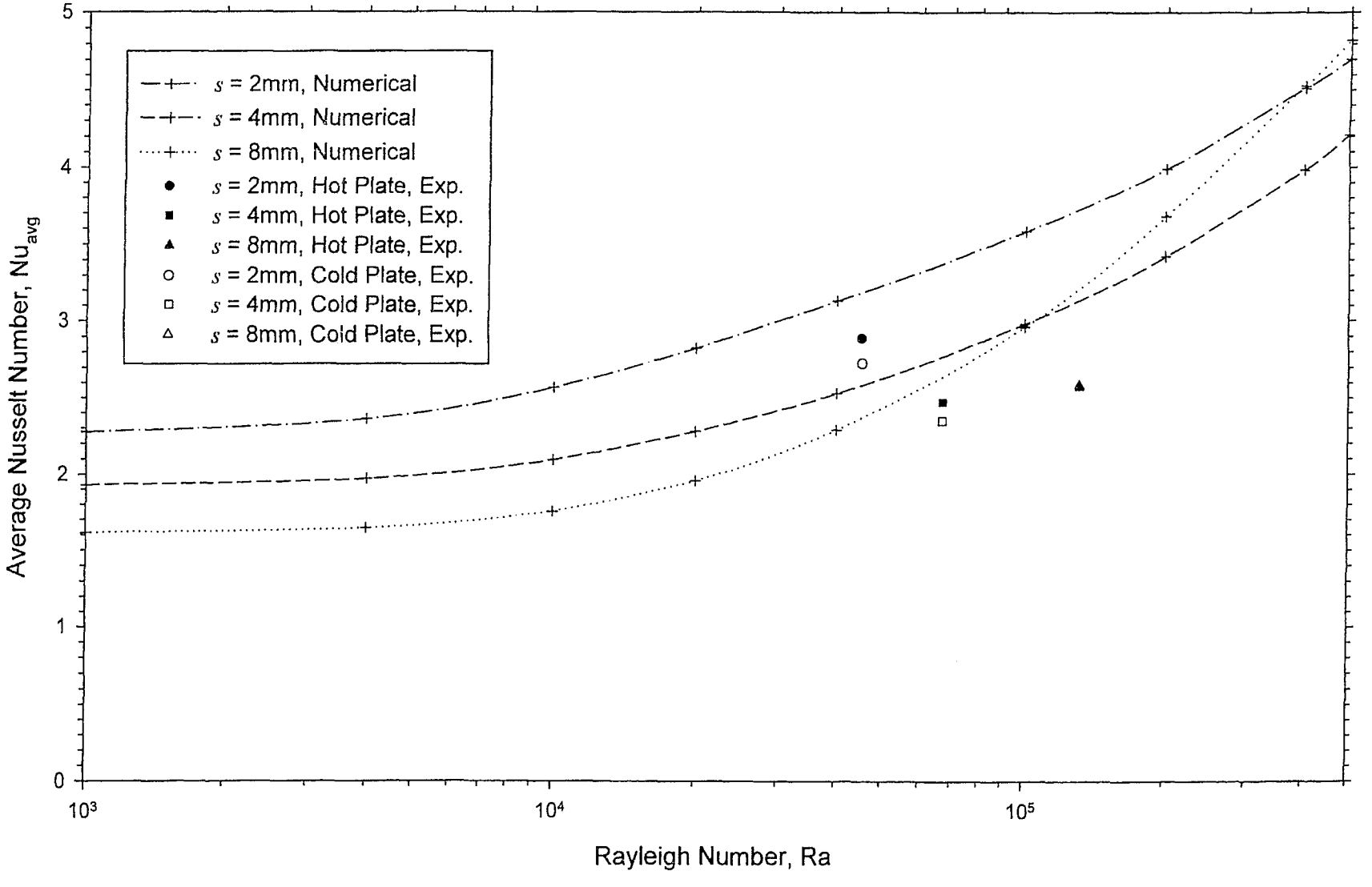

Figure 5.11 Comparison of numerical and experimental average Nusselt numbers for $\phi = 0°$

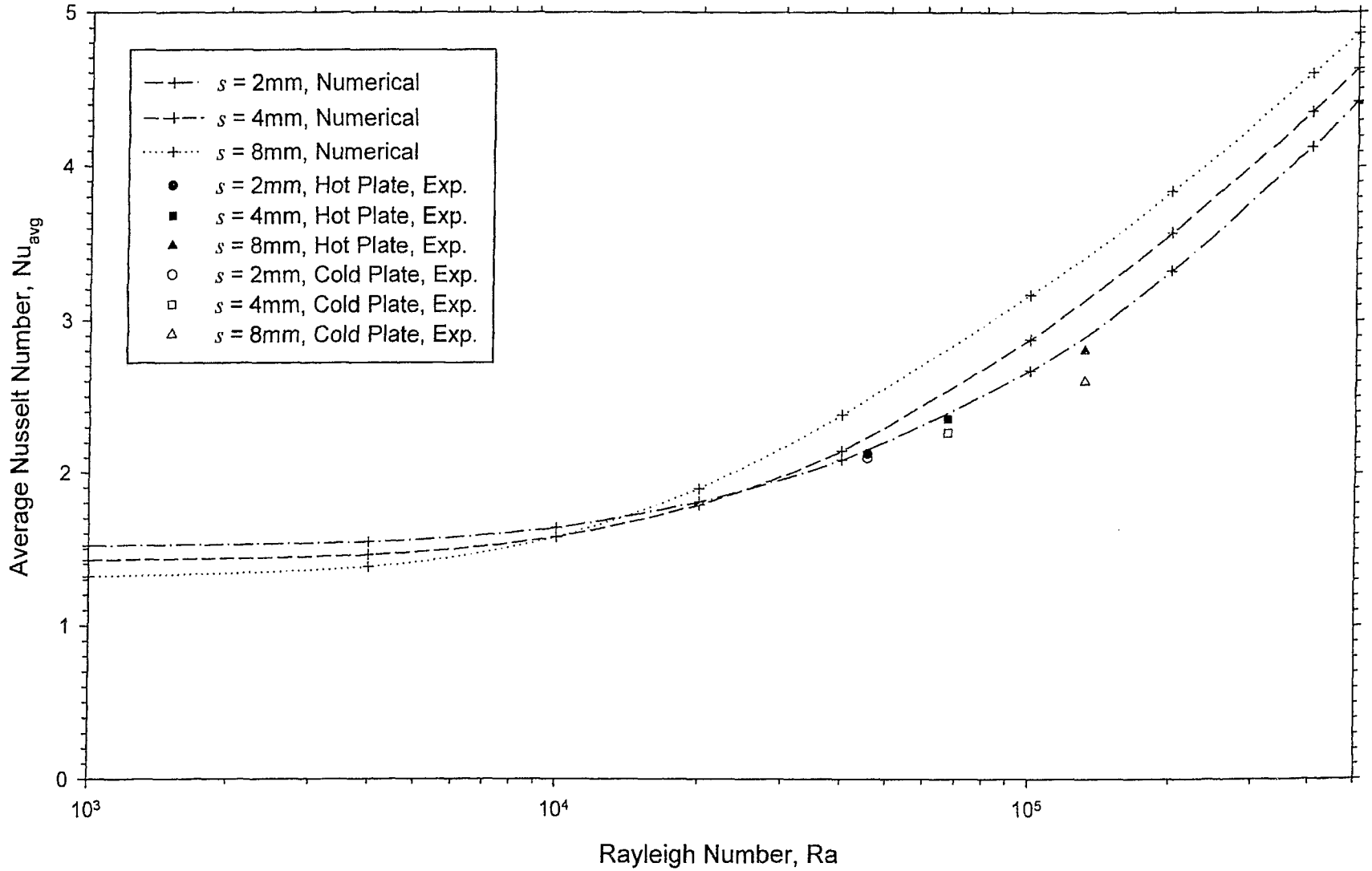

Figure 5.12 Comparison of numerical and experimental average Nusselt numbers for $\phi = 45°$

Chapter 6

CONCLUSIONS AND RECOMMENDATIONS

6.1 Conclusions

The results of an interferometric study on the effect of a between-panes Venetian blind in a double-glazed window have been presented. Finite fringe interferograms were obtained at three different blind tip-to-plate spacings and three different blind slat angles in air at a constant Rayleigh number for each cavity width. Local and average heat transfer data were calculated. Infinite fringe interferograms were taken for visualization of the temperature field inside the cavity. In addition, the results of a preliminary numerical study of the same heat transfer problem were compared with the experimental results. The conclusions are as follows:

i) The results show that a between-panes blind has a significant influence on local heat transfer rates. The distribution of local Nusselt numbers depends strongly on the blind slat angle. The variation in blind tip-to-plate spacings changes the fluid flow patterns inside the window cavity noticeably.

ii) With the exception of one case (s = 2mm and ϕ = 0°), the average Nusselt numbers obtained from the experiment are lower than the values computed from the correlation by ElSherbiny et al. [14] at the corresponding Rayleigh numbers and aspect ratios. This shows that between-panes Venetian blind can enhance the

thermal performance of a double-glazed window by reducing the convective heat transfer across the cavity.

iii) Two types of air flow are observed when the blind is open: the outer circulation around the perimeter of the cavity and the inner circulation which occurs between blind slats. These air flow patterns are comparable to the boundary layer flow and secondary multicellular flow described in the literature for an "empty" cavity.

iv) When the blind is fully open (ϕ = 0°), the conductivity of the aluminum blind slats increases the local heat transfer rates considerably, creating periodic maxima in Nusselt numbers. The effect is especially evident at close blind tip-to-plate spacing (s = 2mm). In this case, the blind slats are acting as thermal bridges between the hot and cold surfaces, greatly reducing the insulating ability of the window cavity at these locations.

v) At the blind slat angle of ϕ = 45°, the local heat transfer rates are affected by the interaction between the inner and outer circulation flows. Maximum local Nusselt numbers occur in the spaces between each slat. From the interferograms, it appears that strong inner circulation pushes the boundary layer towards the plate surfaces. This phenomenon has not been predicted by the numerical solution.

vi) With the blind in the closed position (ϕ = 90°), it partitions the cavity and the outer circulation is limited to flow within two narrower cavities. Although some

air leakage is unavoidable, this improves the performance of the window cavity as it is converted into two layers of insulation.

vii) For close blind tip-to-plate spacing (s = 2mm), the blind slat angle is a dominant factor in governing the local and average heat transfer rates in the cavity. The effect of blind slat angle weakens as the blind tip-to-plate spacing increases.

viii) In general, the numerical results are found to be in good agreement with the experimental data. Except for the blind slat angle of ϕ = 45° described previously, the local heat transfer rate distributions and temperature and flow patterns predicted by the numerical solution are similar in the experiment.

6.2 Recommendations

Suggestions pertaining to the experiment and numerical studies are listed in separate sections.

6.2.1 Recommendations for Experimental Study

i) The main purpose of the present study is to provide experimental data that can be used to validate results from future numerical studies. The development of improved numerical models is essential and ongoing at Ryerson University, and continues to support the research for the window design industry.

ii) The experimental analysis of window thermal performance needs to be done to study the effects of other shading devices such as roller blinds and vertical blinds.

iii) The study of between-panes blind may be extended to plastic or wooden blind slats. These materials have lower thermal conductivities than aluminum, and can help further reduce heat transfer across the window cavity. Heated blind slats should also be used to simulate solar irradiance under daytime conditions.

iv) In order to model the blind as completely closed (ϕ = 90°) and eliminate air leakage, a more sophisticated slat support system is required to precisely control the slat angle. However, as commercial blinds also have small gaps between the overlapping slats in the closed position, it is more realistic to study a blind angle slightly less than $\phi = 90°$ and allow tiny amounts of air to flow through the blind.

v) To better understand the fluid mechanics within the window cavity in the presence of between-panes Venetian blind, a flow visualization study should be conducted to obtain images of the velocity field.

vi) For the present study, measurements were taken on both the hot and cold plates for all twenty-seven finite fringe interferograms, which was a very time-consuming task. A digital analyzing system, like the one at University of Western Ontario developed by Naylor [73], would be a valuable asset to those performing future interferometric analyses at the Ryerson Heat Transfer Laboratory.

6.2.2 Recommendations for Numerical Study

i) Since the numerical analysis is intended to be a preliminary study for the experiment, radiative exchange has not been included in the computation to lessen the complexity of the problem. A full conjugate conduction/convection/radiation numerical model has to be developed to better approximate the heat transfer in the experiment.

ii) The top and bottom horizontal walls are modeled as adiabatic surfaces in the present numerical model. Obviously, there are minor heat losses happening at the end walls in the experimental model. There is a need to adequately simulate these end wall conditions in the numerical model in order to get acceptable local heat transfer results.

iii) As mentioned above, the blind cannot realistically be fully shut, and hence, should not be modeled as perfectly sealed in the numerical model. Instead, it should be represented as a permeable screen with a reasonable spacing set between overlapping slats. In this way, the numerical solution will be able to include the effect of air leakage in the cavity.

Appendix A

AIR PROPERTIES

Air properties were obtained from published data from Thermophysical Properties Research Center, Purdue University [74, 75, 76]. An extensive collection of experimental works was investigated to compile tabulated recommended values for dynamic viscosity, thermal conductivity, and specific heat. All properties are considered to be a function of temperature only, with the exception of density.

A.1 Dynamic Viscosity (μ)

The recommended values of Touloukian, Saxena, and Hestermans [74] are plotted as the upper curve in Figure A.1. Dynamic viscosity values evaluated at the film temperature were obtained by linear interpolations between data points. The values have an estimated accuracy of ±0.5% in the temperature range of this study.

A.2 Thermal Conductivity (k)

The recommended values of Touloukian, Liley, and Saxena [75] are plotted as the lower curve in Figure A.1. Thermal conductivity values evaluated at the plate surface temperature were obtained by linear interpolations between data points. The values have an estimated accuracy of ±1% in the temperature range of this study.

A.3 Specific Heat (C_p)

The following equation given by Toulukian and Makita [76] were used to obtain specific heat values at the film temperature. The correlation is valid for temperatures between 260K and 610K at standard pressure. The values are estimated to be accurate to ±0.25%.

$$C_p = 1044.66 - 3.15967\times10^{-1}T + 7.07908\times10^{-4}T^2 - 2.7034\times10^{-7}T^3 \qquad (A.1)$$

where temperature is in [K].

A.4 Density (ρ)

The density of air was calculated using the ideal gas law.

$$\rho = \frac{p}{RT} \qquad (A.2)$$

where R = 287.097J/kg·K; temperature is in [K] and pressure is in [Pa].

A.5 Coefficient of Thermal Expansion (β)

Since air is considered to behave as an ideal gas, the expression for the coefficient of thermal expansion can be simplified to:

$$\beta = \frac{1}{T_f} \qquad (A.3)$$

where T_f is the absolute film temperature in [K].

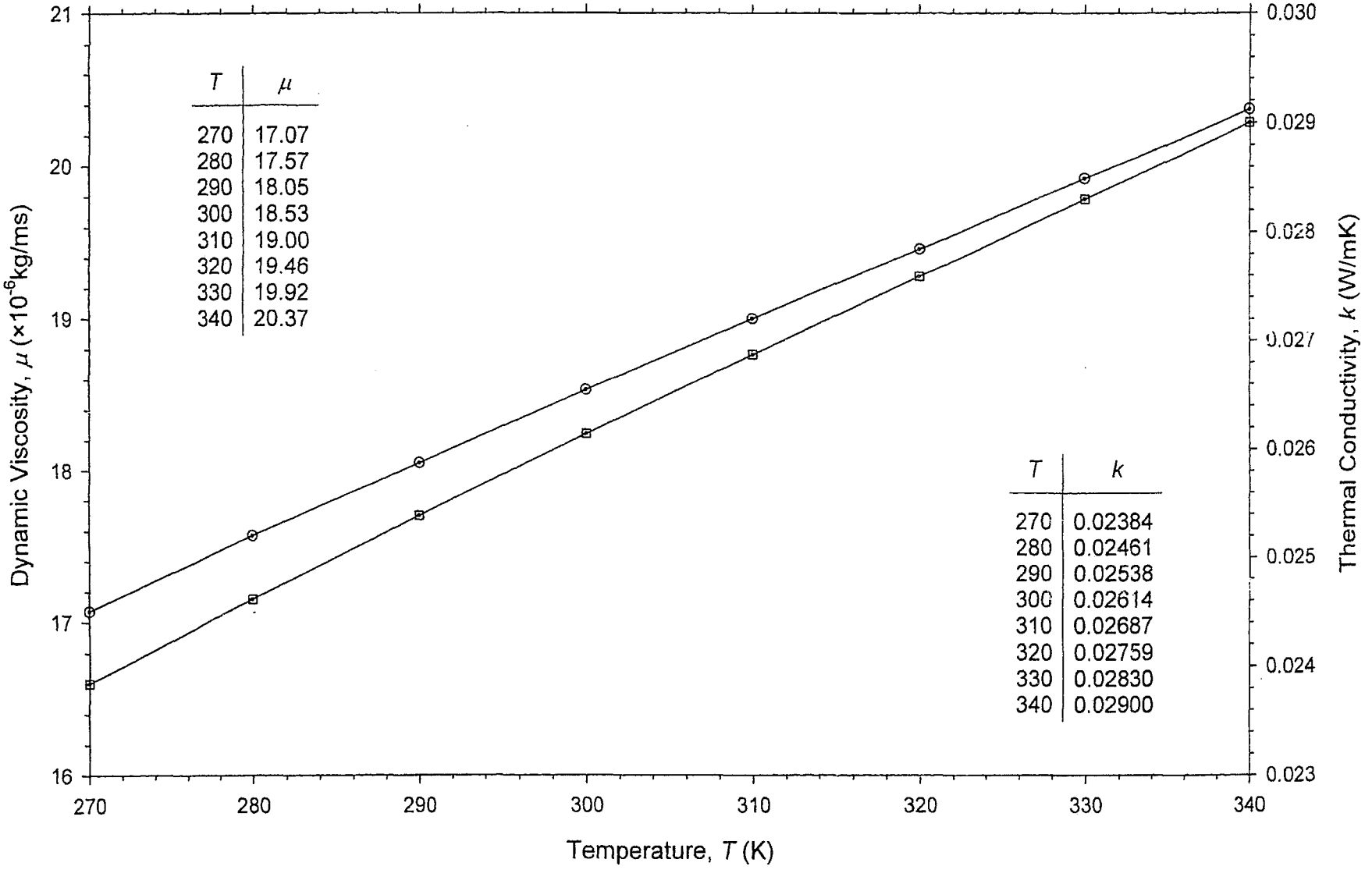

Figure A.1 Air properties: dynamic viscosity & thermal conductivity

Appendix B

EXPERIMENTAL DATA

Table B.1 Hot plate thermocouple calibration

Actual (°C)	Thermocouple Readings (°C)							
	1	2	3	4	5	6	7	8
15.0	14.9	14.4	14.8	14.9	14.9	14.4	14.9	14.8
20.0	20.1	19.7	19.9	20.2	20.1	19.6	20.0	20.0
25.0	24.6	24.3	24.6	25.3	24.6	24.4	24.6	25.0
30.0	29.6	29.3	29.5	29.8	29.5	29.3	29.5	29.5
25.0	24.6	24.3	24.6	24.3	24.6	24.3	24.6	25.0
20.0	20.2	19.7	19.9	20.2	20.1	19.6	20.0	20.0
15.0	15.0	14.5	14.8	14.9	15.0	14.5	15.0	14.8
25.5	25.2	24.8	25.1	24.5	25.2	24.9	25.2	25.1
30.0	29.7	29.3	29.5	29.8	29.5	29.4	29.6	29.6
35.5	35.3	34.9	35.1	35.4	35.1	35.0	35.1	35.0
40.0	39.7	39.4	39.5	39.6	39.7	39.4	39.6	39.6
35.1	34.8	34.5	34.7	34.9	34.7	34.5	34.7	34.7
30.0	29.7	29.4	29.5	29.8	29.6	29.4	29.6	29.6
25.5	25.2	24.8	25.1	25.2	25.2	24.8	25.2	25.1
Correction	**+0.2**	**+0.6**	**+0.3**	**+0.2**	**+0.2**	**+0.6**	**+0.3**	**+0.3**

Table B.2 Cold plate thermocouple calibration

Actual (°C)	Thermocouple Readings (°C)							
	9	10	11	12	13	14	15	16
15.0	14.8	14.4	14.7	14.5	14.7	14.9	14.4	14.6
20.0	20.0	19.7	19.9	19.7	19.9	20.0	19.6	19.9
25.0	24.6	24.3	24.6	24.8	24.4	24.6	24.3	24.9
30.0	29.5	29.2	29.4	29.3	29.3	29.4	29.2	29.4
25.0	24.6	24.3	24.5	24.8	24.4	24.6	24.3	24.9
20.0	20.1	19.7	19.9	19.7	19.9	20.0	19.6	19.9
15.0	14.9	14.5	14.7	14.5	14.7	14.9	14.4	14.7
25.5	25.1	24.8	25.0	25.3	25.0	25.1	24.9	25.0
30.0	29.6	29.3	29.5	29.3	29.5	29.5	29.3	29.4
35.5	35.2	34.9	35.1	34.9	35.0	35.0	34.9	34.9
40.0	39.6	39.4	39.5	39.3	39.5	39.5	39.4	39.5
35.1	34.7	34.4	34.6	34.5	34.8	35.1	34.5	34.5
30.0	29.6	29.3	29.5	29.3	29.7	29.6	29.3	29.5
25.5	25.1	24.8	25.0	25.3	25.0	25.1	24.8	25.0
Correction	**+0.3**	**+0.6**	**+0.4**	**+0.4**	**+0.4**	**+0.3**	**+0.6**	**+0.4**

Table B.3 Venetian blind thermocouple calibration

Actual (°C)	Thermocouple Readings (°C)							
	17	18	19	20	21	22	23	24
15.0	15.0	14.8	14.3	14.6	14.9	14.7	14.4	14.7
20.0	20.1	20.0	19.6	19.8	20.1	19.9	19.7	19.8
25.0	24.8	24.6	24.2	24.9	24.7	24.6	24.4	25.0
30.0	29.7	29.6	29.2	29.4	30.7	29.6	29.4	29.5
25.0	24.8	24.6	24.2	24.9	25.4	24.6	24.4	25.0
20.0	20.2	20.0	19.6	19.8	20.1	19.9	19.8	19.8
15.0	15.1	14.9	14.4	14.6	14.9	14.8	14.6	14.7
25.5	25.3	25.2	24.8	25.0	25.2	25.2	25.0	25.1
30.0	29.8	29.7	29.4	29.6	29.8	29.6	29.5	29.6
35.5	35.4	35.1	34.9	35.1	35.3	35.2	35.1	35.1
40.0	39.7	39.7	39.5	39.5	39.8	39.7	39.6	39.6
35.1	34.8	34.7	34.4	34.5	34.8	34.8	34.8	34.7
30.0	29.7	29.7	29.4	29.6	29.7	29.6	29.8	29.6
25.5	25.2	25.1	24.8	25.0	25.2	25.1	25.1	25.1
Correction	**+0.2**	**+0.3**	**+0.6**	**+0.4**	**+0.1**	**+0.3**	**+0.4**	**+0.5**

Table B.4 Plate surface average and blind temperatures (°C) for s = 2mm

ϕ	Section	T_∞	$T_{s,h}$	$T_{s,c}$	Blind						
					T_1	T_2	T_3	T_4	T_5	T_6	T_7
0°	top	25.0	34.7	14.9	25.5	25.9	25.4	25.4	25.3	24.7	24.5
	middle	24.2	34.6	14.9	25.6	25.9	25.4	25.6	25.3	24.8	24.5
	bottom	24.2	34.8	14.9	25.7	26.0	25.5	25.7	25.4	25.0	24.1
45°	top	25.0	34.7	15.0	28.0	26.8	25.2	25.5	25.1	23.2	21.6
	middle	24.1	34.7	14.9	27.9	26.6	25.0	25.8	24.7	23.6	22.3
	bottom	24.2	35.0	14.9	28.0	27.0	25.5	25.5	25.0	23.4	21.6
90°	top	25.1	35.0	15.0	27.6	27.4	27.5	25.6	23.2	22.6	20.8
	middle	24.1	34.9	14.9	27.9	28.1	26.9	25.2	23.4	21.8	20.7
	bottom	24.2	34.9	14.9	27.3	28.7	26.9	24.8	23.4	23.1	21.9

Table B.5 Plate surface average and blind temperatures (°C) for s = 4mm

ϕ	Section	T_∞	$T_{s,h}$	$T_{s,c}$	Blind						
					T_1	T_2	T_3	T_4	T_5	T_6	T_7
0°	top	24.3	34.8	14.9	27.4	26.5	25.5	26.1	25.2	24.7	22.7
	middle	24.3	34.7	14.9	27.1	26.3	25.4	25.7	25.1	24.5	22.5
	bottom	24.7	35.0	15.0	27.5	26.7	25.8	25.8	25.3	24.8	22.9
45°	top	24.3	34.8	14.9	28.8	27.6	25.6	25.4	24.4	22.6	21.2
	middle	24.2	35.0	14.9	28.7	27.4	25.7	25.2	24.7	22.3	21.0
	bottom	24.9	35.0	15.0	28.6	27.2	25.3	25.2	24.3	22.4	21.2
90°	top	24.3	35.2	14.9	28.7	28.0	27.4	25.4	23.5	21.8	21.2
	middle	24.3	34.8	14.9	28.8	28.1	27.1	25.0	22.9	22.3	21.6
	bottom	24.8	34.9	14.9	28.4	28.6	26.9	24.1	23.4	22.7	21.9

Table B.6 Plate surface average and blind temperatures (°C) for s = 8mm

ϕ	Section	T_∞	$T_{s,h}$	$T_{s,c}$	Blind						
					T_1	T_2	T_3	T_4	T_5	T_6	T_7
0°	top	24.5	34.9	15.0	29.6	29.0	27.5	25.8	24.1	22.1	20.9
	middle	25.0	35.3	15.0	29.3	28.7	27.1	25.8	23.9	21.9	20.9
	bottom	25.0	34.9	15.0	29.4	28.9	27.3	25.4	23.9	22.0	20.9
45°	top	24.5	35.0	15.0	29.3	28.8	26.8	25.1	23.7	21.6	21.0
	middle	24.4	34.8	14.9	29.4	28.9	26.9	24.8	23.4	21.2	20.9
	bottom	25.1	35.3	15.0	29.7	29.3	27.3	25.0	23.8	21.6	21.0
90°	top	24.5	34.9	15.0	28.7	28.5	27.4	25.5	23.2	22.1	21.8
	middle	24.4	35.1	14.9	28.1	29.1	27.2	25.5	23.3	22.0	21.6
	bottom	25.1	34.9	15.0	27.9	28.7	27.1	25.4	23.2	22.2	21.7

Table B.7(a) Local Nusselt numbers for $s = 2$mm, $\phi = 0°$, top section
$p = 752.642$mmHg, $Ra = 4.439\times10^4$

Hot Plate				Cold Plate			
y (mm)	Nu	y (mm)	Nu	y (mm)	Nu	y (mm)	Nu
72.64	0.7561	0*	2.7875	72.64	-2.5343	0	-1.9021
69.95	0.8741	-2.69	2.9565	69.95	-2.5747	-2.69	-1.4519
67.26	1.4064	-5.38	3.2167	67.26	-2.3045	-5.38	-2.4267
64.57	1.9553	-8.07	5.7990	64.57	-1.8749	-8.07	-3.4215
61.88	2.7744	-10.76	1.3339	61.88	-4.6980	-10.76	-3.2162
59.19	3.5517	-13.45	1.7673	59.19	-4.0426	-13.45	-2.8591
56.50	1.3095	-16.14	2.3285	56.50	-3.1604	-16.14	-2.9111
53.81	1.7674	-18.83	2.7913	53.81	-3.1689	-18.83	-2.5062
51.12	2.2232	-21.52	2.9389	51.12	-2.8561	-21.52	-2.0340
48.43	2.6180	-24.21	2.9499	48.43	-2.6746	-24.21	-1.4971
45.74	2.7623	-26.90	3.0236	45.74	-2.0811	-26.90	-1.6266
43.05	2.8263	-29.59	5.8752	43.05	-1.6291	-29.59	-3.9224
40.36	3.0092	-32.28	1.4838	40.36	-1.7859	-32.28	-3.2940
37.67	6.4149	-34.98	1.7920	37.67	-3.5240	-34.98	-3.2769
34.98	1.3010	-37.67	2.3481	34.98	-3.3563	-37.67	-3.1008
32.28	1.5151	-40.36	2.6301	32.28	-3.1993	-40.36	-2.8772
29.59	2.0439	-43.05	2.9272	29.59	-2.9629	-43.05	-2.2904
26.90	2.3880	-45.74	2.9531	26.90	-3.0045	-45.74	-1.7226
24.21	2.7054	-48.43	3.1502	24.21	-2.3464	-48.43	-1.6591
21.52	2.7491	-51.12	4.4734	21.52	-1.7313	-51.12	-3.9452
18.83	2.7662	-53.81	2.0634	18.83	-1.5824	-53.81	-3.2848
16.14	3.6720			16.14	-4.0960		
13.45	2.7486			13.45	-3.3882		
10.76	1.4939			10.76	-3.2287		
8.07	2.0621			8.07	-3.0067		
5.38	2.5709			5.38	-2.8678		
2.69	2.8330			2.69	-2.4787		

* $y = 0$mm corresponds to the centre locating pin on each interferogram

Table B.7(b) Local Nusselt numbers for $s = 2$mm, $\phi = 0°$, middle section
$p = 760.076$mmHg, $Ra = 4.532\times10^4$

Hot Plate				Cold Plate			
y (mm)	Nu	y (mm)	Nu	y (mm)	Nu	y (mm)	Nu
64.37	1.7959	-2.68	1.6911	64.37	-2.9144	-2.68	-3.1870
61.69	2.2442	-5.36	2.2111	61.69	-2.8574	-5.36	-3.1411
59.01	2.6433	-8.05	2.8435	59.01	-2.8093	-8.05	-2.8279
56.33	2.9030	-10.73	2.9918	56.33	-2.3360	-10.73	-2.3917
53.64	2.8584	-13.41	2.9970	53.64	-1.7615	-13.41	-1.7656
50.96	2.8248	-16.09	2.9230	50.96	-1.5060	-16.09	-1.4115
48.28	3.3245	-18.78	3.3209	48.28	-3.4680	-18.78	-2.7690
45.60	5.3519	-21.46	5.8300	45.60	-3.3073	-21.46	-3.7296
42.92	1.7473	-24.14	1.8958	42.92	-3.0665	-24.14	-3.3860
40.23	2.0141	-26.82	2.1634	40.23	-3.0775	-26.82	-3.0817
37.55	2.5402	-29.50	2.6258	37.55	-2.8753	-29.50	-2.8838
34.87	2.8419	-32.19	2.8709	34.87	-2.5241	-32.19	-2.4505
32.19	2.9118	-34.87	3.1057	32.19	-2.0615	-34.87	-2.0414
29.50	2.9309	-37.55	2.9071	29.50	-1.4900	-37.55	-1.3999
26.82	2.9225	-40.23	3.1872	26.82	-2.2345	-40.23	-1.8646
24.14	4.6802	-42.92	5.3951	24.14	-4.1697	-42.92	-3.7080
21.46	1.8355	-45.60	1.5627	21.46	-3.4766	-45.60	-3.3180
18.78	2.0306	-48.28	1.9043	18.78	-3.3506	-48.28	-3.2321
16.09	2.5108	-50.96	2.4314	16.09	-3.0902	-50.96	-2.9355
13.41	3.0601	-53.64	2.6450	13.41	-2.7798	-53.64	-2.7554
10.73	3.0889	-56.33	2.8132	10.73	-2.2987	-56.33	-2.2843
8.05	3.0351	-59.01	2.7639	8.05	-1.7568	-59.01	-1.7655
5.36	3.0722	-61.69	2.7379	5.36	-2.0474	-61.69	-1.9023
2.68	3.5167	-64.37	4.8659	2.68	-5.5706	-64.37	-4.5645
0	2.5776	-67.06	2.0119	0	-3.3107	-67.06	-3.2619
		-69.74	2.0255			-69.74	-3.2676
		-72.42	2.2777			-72.42	-2.9278
		-75.10	2.7900			-75.10	-2.6730
		-77.78	3.0199			-77.78	-2.4038

Table B.7(c) Local Nusselt numbers for $s = 2$mm, $\phi = 0°$, bottom section
$p = 760.076$mmHg, $Ra = 4.560\times10^4$

Hot Plate				Cold Plate			
y (mm)	Nu	y (mm)	Nu	y (mm)	Nu	y (mm)	Nu
62.16	2.9715	-2.70	3.0702	62.16	-1.9303	-2.70	-2.6981
59.45	2.8783	-5.40	3.1782	59.45	-1.7990	-5.40	-1.7345
56.75	3.7502	-8.11	3.2519	56.75	-3.5995	-8.11	-1.4515
54.05	3.6386	-10.81	4.0600	54.05	-3.7295	-10.81	-3.0109
51.35	1.9199	-13.51	3.8782	51.35	-3.5594	-13.51	-3.6663
48.64	2.2656	-16.21	1.9302	48.64	-3.2456	-16.21	-3.6565
45.94	2.6187	-18.92	2.2963	45.94	-2.9022	-18.92	-3.1343
43.24	3.2055	-21.62	2.8987	43.24	-2.5019	-21.62	-2.9536
40.54	3.1393	-24.32	3.0407	40.54	-2.0831	-24.32	-2.5528
37.83	3.1642	-27.02	3.0531	37.83	-1.6507	-27.02	-1.9401
35.13	3.3206	-29.73	3.3817	35.13	-2.4821	-29.73	-1.5408
32.43	6.0159	-32.43	3.5828	32.43	-3.8084	-32.43	-3.1281
29.73	1.7549	-35.13	4.4698	29.73	-3.4037	-35.13	-3.6943
27.02	2.2382	-37.83	1.9635	27.02	-3.2993	-37.83	-3.1782
24.32	2.7601	-40.54	2.3296	24.32	-3.1417	-40.54	-2.9730
21.62	2.9706	-43.24	2.8765	21.62	-2.8494	-43.24	-2.9627
18.92	3.1266	-45.94	3.5486	18.92	-2.4438	-45.94	-2.6068
16.21	3.1499	-48.64	3.6497	16.21	-2.0119	-48.64	-2.1786
13.51	3.1935	-51.35	3.4376	13.51	-1.6116	-51.35	-1.6884
10.81	5.1827	-54.05	3.7734	10.81	-3.9051	-54.05	-1.3951
8.11	2.8629	-56.75	4.8065	8.11	-3.7042	-56.75	-3.7940
5.40	2.0507	-59.45	3.3943	5.40	-3.4001	-59.45	-2.3109
2.70	2.4953	-62.16	2.6070	2.70	-3.2387	-62.16	-1.4226
0	2.7985	-64.86	3.0393	0	-2.9853	-64.86	-0.9735
		-67.56	2.1268			-67.56	-0.8641

Table B.7(d) Local Nusselt numbers for $s = 2$mm, $\phi = 45°$, top section
$p = 752.642$mmHg, $Ra = 4.451 \times 10^4$

Hot Plate				Cold Plate			
y (mm)	Nu	y (mm)	Nu	y (mm)	Nu	y (mm)	Nu
72.84	0.1667	0	2.6165	72.84	-4.5229	0	-1.8201
70.14	0.1897	-2.70	2.3218	70.14	-5.5257	-2.70	-1.9285
67.45	0.2241	-5.40	2.2784	67.45	-3.9996	-5.40	-2.0873
64.75	0.1510	-8.09	2.0756	64.75	-3.3751	-8.09	-2.1672
62.05	0.5102	-10.79	1.8633	62.05	-3.1331	-10.79	-2.1402
59.35	0.6973	-13.49	1.6315	59.35	-3.2095	-13.49	-2.2810
56.65	0.7935	-16.19	1.4602	56.65	-3.3102	-16.19	-1.9779
53.96	0.8577	-18.88	1.5529	53.96	-3.1661	-18.88	-1.7721
51.26	0.6940	-21.58	2.0957	51.26	-3.0530	-21.58	-1.8594
48.56	0.7316	-24.28	2.4282	48.56	-2.9973	-24.28	-2.0269
45.86	0.9609	-26.98	2.4379	45.86	-2.8695	-26.98	-2.3131
43.16	1.1600	-29.68	2.3316	43.16	-2.5378	-29.68	-2.3453
40.47	1.2453	-32.37	2.0021	40.47	-2.3670	-32.37	-2.4533
37.77	1.2482	-35.07	1.7593	37.77	-2.5396	-35.07	-2.2840
35.07	1.0407	-37.77	1.6723	35.07	-2.6250	-37.77	-1.8108
32.37	1.2248	-40.47	1.9332	32.37	-2.5157	-40.47	-1.5649
29.68	1.4260	-43.16	2.4089	29.68	-2.2175	-43.16	-1.7953
26.98	1.7976	-45.86	2.7299	26.98	-2.2104	-45.86	-1.9526
24.28	2.0062	-48.56	2.8316	24.28	-2.1704	-48.56	-2.0888
21.58	2.1170	-51.26	2.6073	21.58	-1.9161	-51.26	-2.1547
18.88	2.0393	-53.96	2.2755	18.88	-2.0330	-53.96	-2.2099
16.19	1.9051			16.19	-2.5230		
13.49	1.6401			13.49	-2.5674		
10.79	1.5314			10.79	-2.5354		
8.09	1.4987			8.09	-2.2323		
5.40	1.6731			5.40	-1.6978		
2.70	2.1512			2.70	-1.6132		

Table B.7(e) Local Nusselt numbers for $s = 2$mm, $\phi = 45°$, middle section
$p = 760.076$mmHg, $Ra = 4.548 \times 10^4$

Hot Plate				Cold Plate			
y (mm)	Nu	y (mm)	Nu	y (mm)	Nu	y (mm)	Nu
67.12	1.7751	-2.68	1.9367	67.12	-2.2384	-2.68	-2.2734
64.44	1.7280	-5.37	1.6519	64.44	-2.3269	-5.37	-2.2121
61.75	1.8036	-8.05	1.5744	61.75	-2.0001	-8.05	-2.2520
59.07	2.0986	-10.74	2.0402	59.07	-1.5818	-10.74	-2.1860
56.38	2.4492	-13.42	2.0512	56.38	-1.9576	-13.42	-2.0005
53.70	2.6490	-16.11	2.2877	53.70	-2.0776	-16.11	-1.9397
51.01	2.6572	-18.79	2.1550	51.01	-2.3522	-18.79	-2.0105
48.33	2.5507	-21.48	1.8961	48.33	-2.6978	-21.48	-2.0553
45.64	2.1529	-24.16	1.8640	45.64	-2.7683	-24.16	-2.1334
42.96	1.8805	-26.85	1.9881	42.96	-2.6433	-26.85	-1.9146
40.27	1.7741	-29.53	2.3412	40.27	-2.4464	-29.53	-1.5430
37.59	1.6362	-32.22	2.6762	37.59	-2.1054	-32.22	-1.7336
34.90	1.5190	-34.90	3.0843	34.90	-1.8772	-34.90	-1.8976
32.22	2.0603	-37.59	2.6624	32.22	-2.1782	-37.59	-1.9677
29.53	2.3532	-40.27	2.5235	29.53	-2.1881	-40.27	-2.0341
26.85	2.4062	-42.96	2.1405	26.85	-2.1542	-42.96	-2.1908
24.16	2.2269	-45.64	1.9249	24.16	-2.3123	-45.64	-2.2278
21.48	1.9986	-48.33	1.9099	21.48	-2.3240	-48.33	-2.0405
18.79	1.7249	-51.01	1.8378	18.79	-2.1893	-51.01	-1.7939
16.11	1.7779	-53.70	2.0754	16.11	-2.2000	-53.70	-1.3964
13.42	2.1169	-56.38	2.5902	13.42	-1.8415	-56.38	-1.9185
10.74	2.8470	-59.07	2.5865	10.74	-1.7996	-59.07	-2.1417
8.05	2.7039	-61.75	2.6297	8.05	-1.9265	-61.75	-2.2983
5.37	2.8174	-64.44	2.2927	5.37	-2.0237	-64.44	-2.5220
2.68	2.6619	-67.12	1.9806	2.68	-2.2506	-67.12	-2.8194
0	2.0892	-69.80	1.7103	0	-2.2928	-69.80	-2.7124
		-72.49	1.4330			-72.49	-2.4938
		-75.17	1.3421			-75.17	-2.2466
		-77.86	1.7863			-77.86	-2.2341

Table B.7(f) Local Nusselt numbers for $s = 2$mm, $\phi = 45°$, bottom section
$p = 760.076$mmHg, $Ra = 4.589\times10^4$

Hot Plate				Cold Plate			
y (mm)	Nu	y (mm)	Nu	y (mm)	Nu	y (mm)	Nu
61.73	2.6951	-2.68	2.5608	61.73	-1.8906	-2.68	-1.9807
59.05	2.7180	-5.37	2.6152	59.05	-2.0061	-5.37	-1.9534
56.36	2.4989	-8.05	2.5165	56.36	-2.3010	-8.05	-1.6352
53.68	2.0803	-10.74	2.4383	53.68	-2.3886	-10.74	-1.5972
51.00	1.9652	-13.42	2.1129	51.00	-2.4671	-13.42	-1.6983
48.31	1.7838	-16.10	2.1394	48.31	-1.9658	-16.10	-1.6552
45.63	1.8295	-18.79	2.3403	45.63	-1.7854	-18.79	-1.7767
42.94	2.1059	-21.47	2.5990	42.94	-1.6834	-21.47	-1.7376
40.26	2.5704	-24.16	2.8036	40.26	-2.0032	-24.16	-1.9788
37.58	2.5480	-26.84	2.6995	37.58	-2.1753	-26.84	-1.9613
34.89	2.3896	-29.52	2.6935	34.89	-2.4752	-29.52	-1.3017
32.21	2.3101	-32.21	2.7245	32.21	-2.3468	-32.21	-1.2091
29.52	1.9272	-34.89	2.6083	29.52	-2.4803	-34.89	-1.0464
26.84	1.7826	-37.58	2.6873	26.84	-2.4059	-37.58	-1.0119
24.16	1.7502	-40.26	2.8112	24.16	-2.2365	-40.26	-0.9276
21.47	2.0378	-42.94	3.1753	21.47	-2.0359	-42.94	-0.7965
18.79	2.4328	-45.63	3.7203	18.79	-2.0037	-45.63	-0.7882
16.10	2.6820	-48.31	3.7062	16.10	-1.9318	-48.31	-1.2722
13.42	2.4995	-51.00	3.3205	13.42	-1.9335	-51.00	-1.0333
10.74	2.5035	-53.68	3.4875	10.74	-1.9049	-53.68	-0.7608
8.05	2.1735	-56.36	3.5740	8.05	-2.0300	-56.36	-0.5822
5.37	1.9370	-59.05	3.6056	5.37	-2.0641	-59.05	-0.3405
2.68	1.9174	-61.73	3.9594	2.68	-1.9598	-61.73	-0.1323
0	2.0107	-64.42	4.1248	0	-2.0039	-64.42	-0.2721

Table B.7(g) Local Nusselt numbers for $s = 2$mm, $\phi = 90°$, top section
$p = 752.642$mmHg, $Ra = 4.489 \times 10^4$

Hot Plate				Cold Plate			
y (mm)	Nu	y (mm)	Nu	y (mm)	Nu	y (mm)	Nu
72.92	0.4572	0	0.6300	72.92	-2.7998	0	-2.0653
70.22	0.4479	-2.70	0.5933	70.22	-3.3066	-2.70	-2.1004
67.52	0.4421	-5.40	0.5808	67.52	-3.2568	-5.40	-2.1210
64.81	0.4610	-8.10	0.6028	64.81	-3.0064	-8.10	-2.1556
62.11	0.5539	-10.80	0.5995	62.11	-3.3107	-10.80	-2.1388
59.41	0.6129	-13.50	0.6294	59.41	-3.8005	-13.50	-2.0410
56.71	0.6150	-16.20	0.6493	56.71	-4.1286	-16.20	-2.1662
54.01	0.6110	-18.90	0.7189	54.01	-4.1640	-18.90	-2.1754
51.31	0.1620	-21.60	0.6326	51.31	-4.0079	-21.60	-2.0294
48.61	0.1614	-24.31	0.7103	48.61	-3.5568	-24.31	-2.0998
45.91	0.1652	-27.01	0.7125	45.91	-3.3781	-27.01	-2.0555
43.21	0.5060	-29.71	0.6971	43.21	-3.0464	-29.71	-2.0283
40.51	0.5565	-32.41	0.6963	40.51	-2.8984	-32.41	-2.1249
37.81	0.5883	-35.11	0.6974	37.81	-2.6964	-35.11	-2.0538
35.11	0.5621	-37.81	0.7417	35.11	-2.5343	-37.81	-2.0300
32.41	0.5729	-40.51	0.7579	32.41	-2.3521	-40.51	-1.9274
29.71	0.5978	-43.21	0.7965	29.71	-2.3451	-43.21	-1.9435
27.01	0.5876	-45.91	0.8108	27.01	-2.1529	-45.91	-1.9475
24.31	0.6074	-48.61	0.8414	24.31	-2.1200	-48.61	-1.9138
21.60	0.5855	-51.31	0.8649	21.60	-1.9908	-51.31	-1.8664
18.90	0.5724	-54.01	0.8891	18.90	-2.0443	-54.01	-1.7757
16.20	0.5511	-56.71	0.8990	16.20	-2.1936	-56.71	-1.8620
13.50	0.5069			13.50	-2.2585		
10.80	0.4980			10.80	-2.2214		
8.10	0.5174			8.10	-2.2469		
5.40	0.5284			5.40	-2.2012		
2.70	0.5934			2.70	-2.1331		

Table B.7(h) Local Nusselt numbers for $s = 2$mm, $\phi = 90°$, middle section
$p = 760.076$mmHg, $Ra = 4.574 \times 10^4$

Hot Plate				Cold Plate			
y (mm)	Nu	y (mm)	Nu	y (mm)	Nu	y (mm)	Nu
64.29	0.7806	-2.68	1.1350	64.29	-1.6764	-2.68	-1.0822
61.61	0.7880	-5.36	1.2185	61.61	-1.5883	-5.36	-0.9704
58.93	0.4759	-8.04	1.2907	58.93	-1.6318	-8.04	-1.2844
56.25	0.5949	-10.72	1.3014	56.25	-1.5614	-10.72	-1.2147
53.58	0.6576	-13.39	1.3897	53.58	-1.3999	-13.39	-1.1044
50.90	0.7191	-16.07	1.1868	50.90	-1.3334	-16.07	-1.0674
48.22	0.7262	-18.75	1.2448	48.22	-1.6117	-18.75	-0.9520
45.54	0.7916	-21.43	1.3261	45.54	-1.5859	-21.43	-0.9084
42.86	0.8497	-24.11	1.3937	42.86	-1.4938	-24.11	-1.0469
40.18	0.8789	-26.79	1.5043	40.18	-1.4474	-26.79	-1.0352
37.50	0.6163	-29.47	1.5149	37.50	-1.4193	-29.47	-0.9589
34.82	0.7443	-32.15	1.2792	34.82	-1.3199	-32.15	-0.9059
32.15	0.8533	-34.82	1.3367	32.15	-1.3194	-34.82	-0.8545
29.47	0.9572	-37.50	1.3680	29.47	-1.2860	-37.50	-0.7792
26.79	0.9994	-40.18	1.4391	26.79	-1.4373	-40.18	-1.0140
24.11	1.0112	-42.86	1.5921	24.11	-1.3548	-42.86	-0.9297
21.43	1.0562	-45.54	1.6789	21.43	-1.2563	-45.54	-0.8943
18.75	1.1423	-48.22	1.4239	18.75	-1.2199	-48.22	-0.8148
16.07	0.9013	-50.90	1.4242	16.07	-1.1746	-50.90	-0.7513
13.39	1.0351	-53.58	1.5181	13.39	-1.1398	-53.58	-0.7251
10.72	1.0539	-56.25	1.6056	10.72	-1.0468	-56.25	-0.6764
8.04	1.0962	-58.93	1.6158	8.04	-1.2769	-58.93	-0.6213
5.36	1.1752	-61.61	1.6536	5.36	-1.1786	-61.61	-0.8429
2.68	1.2756	-64.29	1.4879	2.68	-1.1186	-64.29	-0.8033
0	0.9953	-66.97	1.6012	0	-1.0518	-66.97	-0.7705
		-69.65	1.6686			-69.65	-0.7329
		-72.33	1.7783			-72.33	-0.6587
		-75.01	1.8316			-75.01	-0.6093
		-77.69	1.8255			-77.69	-0.5488
		-80.36	1.6670			-80.36	-0.5066

Table B.7(i) Local Nusselt numbers for s = 2mm, ϕ = 90°, bottom section
p = 760.076mmHg, $Ra = 4.578\times10^4$

Hot Plate				Cold Plate			
y (mm)	Nu	y (mm)	Nu	y (mm)	Nu	y (mm)	Nu
61.83	1.9233	-2.69	2.2665	61.83	-1.0452	-2.69	-0.6769
59.14	1.7499	-5.38	2.2114	59.14	-1.1021	-5.38	-0.6979
56.46	1.7429	-8.07	2.1433	56.46	-0.9783	-8.07	-0.7394
53.77	2.0581	-10.75	2.6517	53.77	-1.0716	-10.75	-0.7107
51.08	1.9460	-13.44	2.4711	51.08	-1.0014	-13.44	-0.7153
48.39	1.9608	-16.13	2.5095	48.39	-0.9642	-16.13	-0.6326
45.70	1.8836	-18.82	2.3753	45.70	-0.8968	-18.82	-0.6017
43.01	2.0554	-21.51	2.3385	43.01	-0.8765	-21.51	-0.6221
40.33	2.1545	-24.20	2.6552	40.33	-0.9341	-24.20	-0.6389
37.64	2.0333	-26.88	2.8198	37.64	-0.9321	-26.88	-0.6486
34.95	2.1400	-29.57	2.5633	34.95	-0.7933	-29.57	-0.6902
32.26	2.0705	-32.26	2.5971	32.26	-0.8333	-32.26	-0.7024
29.57	2.2886	-34.95	2.7433	29.57	-0.8092	-34.95	-0.6595
26.88	2.2330	-37.64	3.0994	26.88	-0.7683	-37.64	-0.6073
24.20	2.1104	-40.33	3.1258	24.20	-0.7438	-40.33	-0.5432
21.51	2.0628	-43.01	3.3011	21.51	-0.6214	-43.01	-0.4953
18.82	1.9881	-45.70	3.4734	18.82	-0.6232	-45.70	-0.5199
16.13	2.1801	-48.39	4.4981	16.13	-0.6720	-48.39	-0.5273
13.44	2.0227	-51.08	3.8361	13.44	-0.7081	-51.08	-0.5227
10.75	2.0848	-53.77	3.7547	10.75	-0.6605	-53.77	-0.5185
8.07	2.0860	-56.46	4.2712	8.07	-0.6633	-56.46	-0.4682
5.38	2.0199	-59.14	4.5699	5.38	-0.6642	-59.14	-0.4159
2.69	2.2735	-61.83	4.4413	2.69	-0.6868	-61.83	-0.3585
0	2.0370	-64.52	3.7498	0	-0.6739	-64.52	-0.2878

Table B.8(a) Local Nusselt numbers for $s = 4$mm, $\phi = 0°$, top section
$p = 753.403$mmHg, $Ra = 6.623\times10^4$

Hot Plate				Cold Plate			
y (mm)	Nu	y (mm)	Nu	y (mm)	Nu	y (mm)	Nu
72.56	0.4604	0	2.3657	72.56	-3.8194	0	-1.9527
69.87	0.3992	-2.69	2.4773	69.87	-4.2811	-2.69	-1.8405
67.19	0.7159	-5.37	2.8625	67.19	-4.1257	-5.37	-2.3620
64.50	1.3159	-8.06	2.7592	64.50	-4.2570	-8.06	-2.5760
61.81	1.9090	-10.75	1.8594	61.81	-4.4075	-10.75	-2.5665
59.12	1.7248	-13.44	2.1004	59.12	-3.8801	-13.44	-2.4580
56.44	1.3866	-16.12	2.2556	56.44	-3.3413	-16.12	-2.5134
53.75	1.6235	-18.81	2.3616	53.75	-3.4817	-18.81	-2.3820
51.06	1.7601	-21.50	2.3892	51.06	-3.2621	-21.50	-2.1728
48.37	1.8782	-24.19	2.5509	48.37	-3.0659	-24.19	-1.9463
45.69	1.9248	-26.87	2.7704	45.69	-2.8201	-26.87	-1.9752
43.00	2.0748	-29.56	2.3253	43.00	-2.4976	-29.56	-2.6130
40.31	2.4650	-32.25	2.0208	40.31	-2.5200	-32.25	-2.6251
37.62	2.5558	-34.94	2.1514	37.62	-2.8667	-34.94	-2.4614
34.94	1.9298	-37.62	2.2970	34.94	-2.8257	-37.62	-2.5197
32.25	1.8744	-40.31	2.3657	32.25	-2.7000	-40.31	-2.4092
29.56	2.1461	-43.00	2.3850	29.56	-2.7006	-43.00	-2.2393
26.87	2.2678	-45.69	2.3352	26.87	-2.6113	-45.69	-1.9740
24.19	2.1480	-48.37	2.6338	24.19	-2.4295	-48.37	-2.0538
21.50	2.1783	-51.06	3.1237	21.50	-2.1282	-51.06	-2.6243
18.81	2.4030	-53.75	2.0292	18.81	-2.2002	-53.75	-2.5440
16.12	2.6389			16.12	-2.6707		
13.44	1.9096			13.44	-2.8209		
10.75	2.0506			10.75	-2.6179		
8.06	2.1701			8.06	-2.5136		
5.37	2.2252			5.37	-2.4864		
2.69	2.2511			2.69	-2.3452		

Table B.8(b) Local Nusselt numbers for $s = 4$mm, $\phi = 0°$, middle section
$= 753.403$mmHg, $Ra = 6.605\times10^4$

Hot Plate				Cold Plate			
y (mm)	Nu	y (mm)	Nu	y (mm)	Nu	y (mm)	Nu
61.45	2.3370	-2.67	2.3026	61.45	-2.3935	-2.67	-2.6238
58.78	2.3342	-5.34	2.3875	58.78	-2.3997	-5.34	-2.3837
56.10	2.3902	-8.01	2.6927	56.10	-2.2650	-8.01	-2.2906
53.43	2.3796	-10.69	2.4938	53.43	-1.8932	-10.69	-2.2688
50.76	2.8219	-13.36	2.6735	50.76	-1.7111	-13.36	-1.8792
48.09	3.2317	-16.03	2.8636	48.09	-2.4810	-16.03	-1.8725
45.42	2.5499	-18.70	3.3442	45.42	-2.5379	-18.70	-2.0856
42.75	2.2157	-21.37	2.5693	42.75	-2.5535	-21.37	-2.5477
40.07	2.3631	-24.04	2.1964	40.07	-2.4850	-24.04	-2.4835
37.40	2.4483	-26.72	2.3495	37.40	-2.5474	-26.72	-2.4930
34.73	2.4423	-29.39	2.4572	34.73	-2.4562	-29.39	-2.2051
32.06	2.5685	-32.06	2.4971	32.06	-2.1635	-32.06	-2.3320
29.39	2.6234	-34.73	2.5000	29.39	-2.0671	-34.73	-2.2378
26.72	2.8926	-37.40	2.6971	26.72	-2.1812	-37.40	-2.0109
24.04	2.6885	-40.07	2.9741	24.04	-2.8598	-40.07	-2.0553
21.37	2.1033	-42.75	2.9908	21.37	-2.4760	-42.75	-2.5965
18.70	2.2996	-45.42	2.1433	18.70	-2.4827	-45.42	-2.5871
16.03	2.5368	-48.09	2.3193	16.03	-2.3672	-48.09	-2.4734
13.36	2.5602	-50.76	2.4102	13.36	-2.3353	-50.76	-2.4559
10.69	2.6100	-53.43	2.4540	10.69	-2.1340	-53.43	-2.2675
8.01	2.3987	-56.10	2.4338	8.01	-1.9188	-56.10	-2.0051
5.34	2.5877	-58.78	2.6997	5.34	-2.1056	-58.78	-1.8128
2.67	2.9331	-61.45	2.8896	2.67	-2.8786	-61.45	-1.9964
0	2.5342	-64.12	3.0618	0	-2.7209	-64.12	-2.3840
		-66.79	2.0071			-66.79	-2.5934
		-69.46	2.3033			-69.46	-2.4077
		-72.13	2.4215			-72.13	-2.5196
		-74.80	2.4996			-74.80	-2.5515

Table B.8(c) Local Nusselt numbers for $s = 4$mm, $\phi = 0°$, bottom section
$p = 759.593$mmHg, $Ra = 6.776\times10^4$

Hot Plate				Cold Plate			
y (mm)	Nu	y (mm)	Nu	y (mm)	Nu	y (mm)	Nu
61.53	2.2913	-2.68	2.3169	61.53	-1.4988	-2.68	-1.7534
58.85	2.5179	-5.35	2.4727	58.85	-1.9893	-5.35	-1.6119
56.18	2.7241	-8.03	2.6956	56.18	-2.4343	-8.03	-1.5980
53.50	2.0024	-10.70	2.9320	53.50	-2.2639	-10.70	-2.1502
50.83	2.0101	-13.38	2.1646	50.83	-2.2535	-13.38	-2.2825
48.15	2.0572	-16.05	2.2053	48.15	-2.0984	-16.05	-2.1861
45.48	2.2538	-18.73	2.4708	45.48	-2.0442	-18.73	-2.0782
42.80	2.2621	-21.40	2.5950	42.80	-1.9843	-21.40	-1.9004
40.13	2.2584	-24.08	2.5106	40.13	-1.7795	-24.08	-1.8922
37.45	2.3861	-26.75	2.5324	37.45	-1.8051	-26.75	-1.5120
34.78	2.8548	-29.43	2.6981	34.78	-2.3483	-29.43	-1.3986
32.10	2.1859	-32.10	3.1205	32.10	-2.5756	-32.10	-2.1460
29.43	2.0013	-34.78	2.9447	29.43	-2.3181	-34.78	-2.2690
26.75	2.0553	-37.45	2.8545	26.75	-2.3330	-37.45	-2.0927
24.08	2.1666	-40.13	3.0294	24.08	-2.2024	-40.13	-1.9418
21.40	2.2117	-42.80	3.2490	21.40	-2.0560	-42.80	-1.7995
18.73	2.1650	-45.48	3.3421	18.73	-1.8777	-45.48	-1.6387
16.05	2.3563	-48.15	3.5298	16.05	-1.7187	-48.15	-1.3734
13.38	2.7125	-50.83	3.5382	13.38	-1.9853	-50.83	-1.2316
10.70	2.6956	-53.50	4.1048	10.70	-2.5556	-53.50	-1.4950
8.03	1.7482	-56.18	4.5780	8.03	-2.3398	-56.18	-1.9140
5.35	2.1035	-58.85	4.4669	5.35	-2.2488	-58.85	-1.1046
2.68	2.2986	-61.53	4.1395	2.68	-2.2448	-61.53	-0.4525
0	2.1259	-64.20	3.7650	0	-2.1988	-64.20	-0.3872

Table B.8(d) Local Nusselt numbers for $s = 4$mm, $\phi = 45°$, top section
$p = 753.403$mmHg, $Ra = 6.623\times10^4$

Hot Plate				Cold Plate			
y (mm)	Nu	y (mm)	Nu	y (mm)	Nu	y (mm)	Nu
75.49	0.3714	0	2.5053	75.49	-3.1980	0	-2.0462
72.80	0.2052	-2.70	2.5530	72.80	-5.8795	-2.70	-2.0947
70.10	0.1815	-5.39	2.2192	70.10	-7.0633	-5.39	-2.2234
67.41	0.2188	-8.09	1.9832	67.41	-6.2660	-8.09	-2.3423
64.71	0.3607	-10.78	1.8683	64.71	-4.6107	-10.78	-2.8478
62.01	0.5717	-13.48	1.9620	62.01	-4.4343	-13.48	-2.5475
59.32	0.7220	-16.18	2.3391	59.32	-4.0269	-16.18	-2.0588
56.62	0.7974	-18.87	2.3759	56.62	-4.0913	-18.87	-1.7607
53.92	0.7357	-21.57	2.7402	53.92	-3.7684	-21.57	-1.7954
51.23	0.2322	-24.27	2.7821	51.23	-3.8782	-24.27	-2.3078
48.53	0.5596	-26.96	2.4560	48.53	-3.5145	-26.96	-2.6459
45.84	0.8634	-29.66	2.0474	45.84	-3.4483	-29.66	-3.1318
43.14	1.0296	-32.35	1.7766	43.14	-3.3558	-32.35	-2.9922
40.44	1.2308	-35.05	1.5548	40.44	-3.5126	-35.05	-2.6511
37.75	1.3158	-37.75	1.2990	37.75	-3.5296	-37.75	-2.3064
35.05	1.5398	-40.44	1.7094	35.05	-3.5290	-40.44	-1.8131
32.35	1.3135	-43.14	2.1077	32.35	-3.2879	-43.14	-2.0927
29.66	1.5782	-45.84	2.1880	29.66	-2.9661	-45.84	-2.3550
26.96	1.8322	-48.53	2.1401	26.96	-2.9166	-48.53	-2.7487
24.27	1.9223	-51.23	2.0059	24.27	-2.8511	-51.23	-3.0297
21.57	1.9133	-53.92	1.8844	21.57	-2.5794	-53.92	-2.8967
18.87	1.8393	-56.62	1.5436	18.87	-2.7170	-56.62	-2.7535
16.18	1.5819			16.18	-2.8165		
13.48	1.5713			13.48	-2.7952		
10.78	1.7577			10.78	-2.8486		
8.09	2.0609			8.09	-2.7129		
5.39	2.4707			5.39	-2.4486		
2.70	2.6771			2.70	-2.1060		

Table B.8(e) Local Nusselt numbers for $s = 4$mm, $\phi = 45°$, middle section
$p = 753.403$mmHg, $Ra = 6.694\times10^4$

Hot Plate				Cold Plate			
y (mm)	Nu	y (mm)	Nu	y (mm)	Nu	y (mm)	Nu
64.33	2.0618	-2.68	2.1104	64.33	-2.3381	-2.68	-2.1563
61.65	1.7646	-5.36	1.8465	61.65	-2.0741	-5.36	-2.0823
58.97	1.5362	-8.04	1.7829	58.97	-1.7392	-8.04	-1.8686
56.29	1.8751	-10.72	2.2230	56.29	-2.0079	-10.72	-1.7309
53.61	2.2672	-13.40	2.5985	53.61	-2.3227	-13.40	-1.9154
50.93	2.2377	-16.08	2.9092	50.93	-2.6763	-16.08	-2.3035
48.25	2.4076	-18.76	2.7544	48.25	-2.8410	-18.76	-2.4460
45.57	2.2701	-21.44	2.3687	45.57	-2.7837	-21.44	-2.4278
42.89	2.0645	-24.12	2.2029	42.89	-2.6114	-24.12	-2.3207
40.21	2.0613	-26.80	2.1264	40.21	-2.2172	-26.80	-1.8441
37.53	2.4274	-29.48	2.2509	37.53	-1.7791	-29.48	-1.5742
34.85	2.9701	-32.16	2.6397	34.85	-1.8566	-32.16	-1.5117
32.16	3.0635	-34.85	3.0623	32.16	-2.1925	-34.85	-1.8907
29.48	3.1651	-37.53	3.1642	29.48	-2.5074	-37.53	-2.1529
26.80	3.2307	-40.21	3.1894	26.80	-2.8118	-40.21	-2.3758
24.12	2.7889	-42.89	2.9300	24.12	-2.9406	-42.89	-2.4269
21.44	2.4315	-45.57	2.3842	21.44	-2.8185	-45.57	-2.3831
18.76	1.9985	-48.25	1.9737	18.76	-2.4556	-48.25	-2.1472
16.08	1.7466	-50.93	1.7432	16.08	-1.8299	-50.93	-1.8032
13.40	2.0423	-53.61	2.0449	13.40	-2.0463	-53.61	-1.5290
10.72	2.3925	-56.29	2.5045	10.72	-2.0797	-56.29	-1.6824
8.04	2.8150	-58.97	2.7796	8.04	-2.0613	-58.97	-1.9200
5.36	2.9821	-61.65	2.9051	5.36	-2.3288	-61.65	-2.2827
2.68	2.8166	-64.33	2.5484	2.68	-2.5999	-64.33	-2.4148
0	2.7179	-67.01	2.3422	0	-2.3968	-67.01	-2.3833
		-69.69	2.0493			-69.69	-2.2399
		-72.37	1.9307			-72.37	-1.9319
		-75.05	2.4787			-75.05	-1.6060
		-77.73	2.6670				

Table B.8(f) Local Nusselt numbers for $s = 4$mm, $\phi = 45°$, bottom section
$p = 759.593$mmHg, $Ra = 6.772 \times 10^4$

Hot Plate				Cold Plate			
y (mm)	Nu	y (mm)	Nu	y (mm)	Nu	y (mm)	Nu
61.30	2.7525	-2.67	2.9890	61.30	-2.3602	-2.67	-1.6668
58.64	2.8988	-5.33	2.9152	58.64	-2.2923	-5.33	-1.6469
55.97	2.4809	-8.00	2.9425	55.97	-2.5420	-8.00	-1.5256
53.31	2.2496	-10.66	2.7267	53.31	-2.6017	-10.66	-1.5185
50.64	2.0970	-13.33	2.7232	50.64	-2.4604	-13.33	-1.2213
47.98	2.3209	-15.99	2.9000	47.98	-2.1927	-15.99	-1.2719
45.31	2.4972	-18.66	3.0275	45.31	-1.6352	-18.66	-1.3244
42.65	2.8971	-21.32	3.1275	42.65	-1.7070	-21.32	-1.3775
39.98	3.1171	-23.99	3.3358	39.98	-2.0408	-23.99	-1.5277
37.32	3.0499	-26.65	3.4523	37.32	-2.3743	-26.65	-1.5083
34.65	3.5077	-29.32	3.3571	34.65	-2.3693	-29.32	-1.1082
31.98	3.0283	-31.98	3.3417	31.98	-2.4780	-31.98	-1.0508
29.32	2.5236	-34.65	3.6700	29.32	-2.3336	-34.65	-1.0327
26.65	2.0200	-37.32	3.8060	26.65	-2.5848	-37.32	-0.9210
23.99	1.6655	-39.98	3.8222	23.99	-2.1110	-39.98	-0.7833
21.32	2.0802	-42.65	3.9732	21.32	-2.0863	-42.65	-0.1302
18.66	2.3725	-45.31	4.3231	18.66	-1.9777	-45.31	-0.1254
15.99	2.5283	-47.98	4.0002	15.99	-1.9372	-47.98	-0.8378
13.33	2.5199	-50.64	3.9881	13.33	-1.9929	-50.64	-0.7682
10.66	2.4454	-53.31	4.1624	10.66	-1.9834	-53.31	-0.3277
8.00	2.5936	-55.97	4.2646	8.00	-2.0120	-55.97	-0.1723
5.33	2.5365	-58.64	4.6389	5.33	-1.9389	-58.64	-0.1220
2.67	2.6301	-61.30	5.1133	2.67	-2.0076	-61.30	-0.1841
0	2.9968	-63.97	4.6714	0	-2.1258	-63.97	-0.1213
		-66.64	2.9751			-66.64	-0.3666

Table B.8(g) Local Nusselt numbers for $s = 4$mm, $\phi = 90°$, top section
$p = 753.403$mmHg, $Ra = 6.745\times10^4$

Hot Plate				Cold Plate			
y (mm)	Nu	y (mm)	Nu	y (mm)	Nu	y (mm)	Nu
72.78	0.1688	0	0.1650	72.78	-2.7936	0	-2.0169
70.08	0.2678	-2.70	0.1656	70.08	-3.5394	-2.70	-1.9723
67.39	0.2925	-5.39	0.1696	67.39	-3.8901	-5.39	-1.9910
64.69	0.2741	-8.09	0.1649	64.69	-3.5296	-8.09	-1.9247
61.99	0.2654	-10.78	0.1584	61.99	-3.5336	-10.78	-1.8716
59.30	0.2654	-13.48	0.1568	59.30	-3.5957	-13.48	-1.8241
56.60	0.2781	-16.17	0.1816	56.60	-3.4204	-16.17	-1.7133
53.91	0.2626	-18.87	1.3418	53.91	-4.0072	-18.87	-1.7088
51.21	1.8505	-21.56	0.2127	51.21	-3.2841	-21.56	-1.7044
48.52	1.7193	-24.26	0.1992	48.52	-3.1222	-24.26	-1.6783
45.82	1.4088	-26.95	0.1922	45.82	-2.8982	-26.95	-1.9898
43.13	0.2265	-29.65	0.1830	43.13	-2.7503	-29.65	-1.9721
40.43	0.1982	-32.34	0.1819	40.43	-2.5722	-32.34	-1.9216
37.74	0.1796	-35.04	0.2149	37.74	-2.4006	-35.04	-2.0126
35.04	0.1925	-37.74	0.1620	35.04	-2.3718	-37.74	-1.9850
32.34	0.1985	-40.43	0.1552	32.34	-2.2418	-40.43	-1.8863
29.65	0.1332	-43.13	0.1500	29.65	-2.1145	-43.13	-1.9419
26.95	0.1297	-45.82	0.1483	26.95	-2.5205	-45.82	-1.9030
24.26	0.1298	-48.52	0.3399	24.26	-2.3589	-48.52	-1.8484
21.56	0.2307	-51.21	0.3745	21.56	-2.2957	-51.21	-1.8837
18.87	0.2277	-53.91	0.4980	18.87	-2.2912	-53.91	-1.8737
16.17	0.2243			16.17	-2.1408		
13.48	0.2279			13.48	-2.1896		
10.78	0.2283			10.78	-2.2810		
8.09	0.2293			8.09	-2.2081		
5.39	0.1755			5.39	-2.1651		
2.70	0.1710			2.70	-2.1540		

Table B.8(h) Local Nusselt numbers for $s = 4$mm, $\phi = 90°$, middle section
$p = 753.403$mmHg, $Ra = 6.633\times10^4$

Hot Plate				Cold Plate			
y (mm)	Nu	y (mm)	Nu	y (mm)	Nu	y (mm)	Nu
64.40	0.8502	-2.68	1.4335	64.40	-1.7448	-2.68	-1.2173
61.72	0.8489	-5.37	1.4774	61.72	-1.7393	-5.37	-1.1892
59.03	0.8508	-8.05	1.4996	59.03	-1.8354	-8.05	-1.1815
56.35	0.8858	-10.73	1.5498	56.35	-1.8700	-10.73	-1.1858
53.67	0.9217	-13.42	1.3134	53.67	-1.7585	-13.42	-1.1779
50.98	0.9659	-16.10	1.3866	50.98	-1.7911	-16.10	-1.0633
48.30	1.0214	-18.78	1.4035	48.30	-1.6905	-18.78	-1.0493
45.62	1.0154	-21.47	1.4283	45.62	-1.6523	-21.47	-1.0138
42.93	1.0016	-24.15	1.4765	42.93	-1.6328	-24.15	-0.9857
40.25	0.9974	-26.83	1.5874	40.25	-1.5511	-26.83	-0.9096
37.57	1.0600	-29.52	1.6053	37.57	-1.5496	-29.52	-0.9002
34.88	1.0702	-32.20	1.6156	34.88	-1.6046	-32.20	-0.8952
32.20	1.1388	-34.88	1.7381	32.20	-1.5487	-34.88	-1.0896
29.52	1.1486	-37.57	1.8215	29.52	-1.5123	-37.57	-1.0855
26.83	1.1343	-40.25	1.7953	26.83	-1.4389	-40.25	-1.0231
24.15	0.9441	-42.93	1.8033	24.15	-1.4533	-42.93	-0.9829
21.47	0.9838	-45.62	1.8768	21.47	-1.3530	-45.62	-0.9879
18.78	1.0406	-48.30	2.0044	18.78	-1.3229	-48.30	-0.9033
16.10	1.0828	-50.98	1.9965	16.10	-1.2836	-50.98	-0.8855
13.42	1.1177	-53.67	1.7204	13.42	-1.1978	-53.67	-0.8862
10.73	1.1917	-56.35	1.7206	10.73	-1.1380	-56.35	-0.8163
8.05	1.2294	-59.03	1.8354	8.05	-1.4228	-59.03	-0.8010
5.37	1.2743	-61.72	1.8997	5.37	-1.3635	-61.72	-0.7412
2.68	1.3454	-64.40	1.8613	2.68	-1.3757	-64.40	-0.7060
0	1.3142	-67.09	2.0079	0	-1.2634	-67.09	-0.6535
		-69.77	2.0738			-69.77	-0.5940
		-72.45	1.9983			-72.45	-0.5197
		-75.14	2.0713			-75.14	-0.8323
		-77.82	2.1947				

Table B.8(i) Local Nusselt numbers for $s = 4$mm, $\phi = 90°$, bottom section
$p = 759.593$mmHg, $Ra = 6.759\times10^4$

Hot Plate				Cold Plate			
y (mm)	Nu	y (mm)	Nu	y (mm)	Nu	y (mm)	Nu
61.43	2.0672	-2.67	2.9173	61.43	-1.0740	-2.67	-0.4591
58.76	2.1519	-5.34	2.7235	58.76	-1.0663	-5.34	-0.5288
56.09	2.0105	-8.01	2.6804	56.09	-0.8899	-8.01	-0.4955
53.42	2.2255	-10.68	3.0462	53.42	-0.9429	-10.68	-0.4888
50.75	2.2096	-13.36	2.8261	50.75	-0.9285	-13.36	-0.4981
48.08	2.2781	-16.03	2.8709	48.08	-0.9484	-16.03	-0.4999
45.41	2.1144	-18.70	2.8581	45.41	-0.7830	-18.70	-0.4022
42.74	2.4408	-21.37	2.7755	42.74	-0.8219	-21.37	-0.4496
40.07	2.4630	-24.04	2.7295	40.07	-0.8548	-24.04	-0.4914
37.39	2.2768	-26.71	3.1697	37.39	-0.8575	-26.71	-0.5323
34.72	2.2818	-29.38	3.1094	34.72	-0.9062	-29.38	-0.5596
32.05	2.4290	-32.05	3.0879	32.05	-0.7121	-32.05	-0.5057
29.38	2.5886	-34.72	3.0343	29.38	-0.7514	-34.72	-0.4407
26.71	2.4325	-37.39	3.0999	26.71	-0.7751	-37.39	-0.3645
24.04	2.4778	-40.07	3.3775	24.04	-0.7815	-40.07	-0.3544
21.37	2.4837	-42.74	3.4951	21.37	-0.8302	-42.74	-0.3984
18.70	2.8112	-45.41	3.5717	18.70	-0.6660	-45.41	-0.5596
16.03	2.7355	-48.08	3.7075	16.03	-0.6887	-48.08	-0.4851
13.36	2.6637	-50.75	3.9257	13.36	-0.7103	-50.75	-0.4347
10.68	2.6637	-53.42	4.1363	10.68	-0.6914	-53.42	-0.3645
8.01	2.7748	-56.09	4.7077	8.01	-0.6929	-56.09	-0.3070
5.34	2.8832	-58.76	4.5826	5.34	-0.4476	-58.76	-0.1752
2.67	3.0897	-61.43	4.5406	2.67	-0.4001	-61.43	-0.2090
0	3.1041	-64.10	3.7300	0	-0.4258	-64.10	-0.1509

Table B.9(a) Local Nusselt numbers for $s = 8$mm, $\phi = 0°$, top section
$p = 758.916$mmHg, $Ra = 12.978\times10^4$

Hot Plate				Cold Plate			
y (mm)	Nu	y (mm)	Nu	y (mm)	Nu	y (mm)	Nu
81.97	0.9697	0	1.5516	81.97	-4.1511	0	-3.3244
79.05	0.1720	-2.93	1.5586	79.05	-6.0669	-2.93	-3.2274
76.12	0.1624	-5.86	1.5572	76.12	-6.5247	-5.86	-3.1366
73.19	0.2519	-8.78	1.4084	73.19	-7.8669	-8.78	-3.1736
70.26	0.6933	-11.71	1.6222	70.26	-7.9378	-11.71	-2.9773
67.33	0.8746	-14.64	1.5908	67.33	-7.6075	-14.64	-3.1154
64.41	0.5103	-17.57	1.5307	64.41	-6.9350	-17.57	-3.0850
61.48	0.1397	-20.49	1.5552	61.48	-6.5903	-20.49	-3.0460
58.55	0.1416	-23.42	1.5573	58.55	-5.9441	-23.42	-2.9342
55.62	1.0259	-26.35	1.6532	55.62	-5.9349	-26.35	-3.0124
52.70	1.0724	-29.28	1.7495	52.70	-5.4004	-29.28	-3.0820
49.77	1.1015	-32.20	1.6511	49.77	-5.3073	-32.20	-3.1551
46.84	1.1636	-35.13	1.6647	46.84	-4.7764	-35.13	-3.1048
43.91	1.3015	-38.06	1.7667	43.91	-4.7046	-38.06	-2.9497
40.99	1.1670	-40.99	1.9263	40.99	-4.9664	-40.99	-2.9925
38.06	1.1808	-43.91	1.8249	38.06	-4.5750	-43.91	-2.9128
35.13	1.1779	-46.84	1.9485	35.13	-4.2358	-46.84	-2.8660
32.20	1.1939	-49.77	1.9074	32.20	-4.2667	-49.77	-2.6024
29.28	1.2321	-52.70	1.8781	29.28	-3.9638	-52.70	-2.5057
26.35	1.3780	-55.62	1.8828	26.35	-3.9597	-55.62	-2.5476
23.42	1.3693	-58.55	1.7711	23.42	-4.0851	-58.55	-2.3530
20.49	1.3700			20.49	-3.9042		
17.57	1.2985			17.57	-4.0277		
14.64	1.1572			14.64	-3.6827		
11.71	1.4772			11.71	-3.7816		
8.78	1.4834			8.78	-3.8439		
5.86	1.5257			5.86	-3.5332		
2.93	1.5682			2.93	-3.5157		

Table B.9(b) Local Nusselt numbers for s = 8mm, ϕ = 0°, middle section
p = 761.258mmHg, Ra = 13.280×10^4

Hot Plate				Cold Plate			
y (mm)	Nu	y (mm)	Nu	y (mm)	Nu	y (mm)	Nu
-90.58	3.0153	0	1.9489	-87.91	-1.5040	0	-2.1407
-87.91	3.0575	2.66	1.9560	-85.25	-1.6331	2.66	-2.0298
-85.25	2.9314	5.33	2.0825	-82.58	-1.6102	5.33	-1.9852
-82.58	2.8964	7.99	2.0566	-79.92	-1.5425	7.99	-2.1476
-79.92	2.7588	10.66	1.8947	-77.26	-1.7322	10.66	-2.1569
-77.26	2.6838	13.32	1.9743	-74.59	-1.6588	13.32	-2.0450
-74.59	2.7709	15.98	2.1495	-71.93	-1.6025	15.98	-1.9846
-71.93	2.7204	18.65	2.0316	-69.26	-1.6076	18.65	-2.2235
-69.26	2.8483	21.31	2.0506	-66.60	-1.7674	21.31	-2.2522
-66.60	2.6460	23.98	2.1205	-63.94	-1.7507	23.98	-2.1848
-63.94	2.7322	26.64	2.0874	-61.27	-1.7497	26.64	-2.2854
-61.27	2.7423	29.30	1.9766	-58.61	-1.8432	29.30	-2.3939
-58.61	2.4128	31.97	1.9530	-55.94	-1.7894	31.97	-2.3419
-55.94	2.4055	34.63	1.9631	-53.28	-1.7240	34.63	-2.2430
-53.28	2.5390	37.30	1.8646	-50.62	-1.7243	37.30	-2.4450
-50.62	2.7765	39.96	1.8770	-47.95	-1.8677	39.96	-2.4360
-47.95	2.5467	42.62	2.0023	-45.29	-1.8310	42.62	-2.2847
-45.29	2.4999	45.29	1.8302	-42.62	-1.9118	45.29	-2.5035
-42.62	2.5141	47.95	1.9338	-39.96	-1.8378	47.95	-2.5431
-39.96	2.3569	50.62	1.9628	-37.30	-2.0478	50.62	-2.4057
-37.30	2.4161	53.28	2.0273	-34.63	-1.9500		
-34.63	2.4613			-31.97	-1.8662		
-31.97	2.2721			-29.30	-2.0095		
-29.30	2.3578			-26.64	-1.9771		
-26.64	2.4420			-23.98	-1.9611		
-23.98	2.3941			-21.31	-2.1033		
-21.31	2.2961			-18.65	-2.0413		
-18.65	2.3277			-15.98	-2.0926		
-15.98	2.2179			-13.32	-2.1247		
-13.32	2.1816			-10.66	-2.1426		
-10.66	2.0161			-7.99	-2.1484		
-7.99	2.1192			-5.33	-1.9922		
-5.33	2.1256			-2.66	-1.9786		
-2.66	2.1343						

Table B.9(c) Local Nusselt numbers for s = 8mm, ϕ = 0°, bottom section
p = 761.258mmHg, Ra = 13.047×10^4

Hot Plate				Cold Plate			
y (mm)	Nu	y (mm)	Nu	y (mm)	Nu	y (mm)	Nu
61.69	3.1644	-2.68	4.1324	64.37	-1.6145	0	-1.4400
59.00	2.9321	-5.36	4.3174	61.69	-1.7902	-2.68	-1.4010
56.32	3.0130	-8.05	4.3564	59.00	-1.7891	-5.36	-1.3087
53.64	3.1801	-10.73	4.4736	56.32	-1.6449	-8.05	-1.1415
50.96	3.2093	-13.41	4.2238	53.64	-1.7356	-10.73	-1.2129
48.28	3.0120	-16.09	4.6092	50.96	-1.9242	-13.41	-1.3493
45.59	3.2581	-18.77	4.6391	48.28	-1.7559	-16.09	-1.2872
42.91	3.2428	-21.46	4.6519	45.59	-1.7395	-18.77	-1.2922
40.23	3.5682	-24.14	4.8920	42.91	-1.6334	-21.46	-1.3028
37.55	3.3510	-26.82	5.1405	40.23	-1.6386	-24.14	-1.1622
34.87	3.2489	-29.50	4.9785	37.55	-1.6688	-26.82	-1.1736
32.18	3.5396	-32.18	5.6346	34.87	-1.4853	-29.50	-0.8139
29.50	3.3757	-34.87	5.4610	32.18	-1.6533	-32.18	-1.1197
26.82	3.3980	-37.55	5.5535	29.50	-1.6078	-34.87	-1.1006
24.14	3.8628	-40.23	6.1193	26.82	-1.6752	-37.55	-1.1055
21.46	3.5571	-42.91	5.9490	24.14	-1.6826	-40.23	-1.0872
18.77	3.7765	-45.59	6.0473	21.46	-1.5748	-42.91	-0.8882
16.09	3.9728	-48.28	6.9341	18.77	-1.5522	-45.59	-0.8521
13.41	3.9195	-50.96	7.2758	16.09	-1.5888	-48.28	-0.1259
10.73	3.7414	-53.64	7.8682	13.41	-1.3455	-50.96	-0.7935
8.05	3.9921	-56.32	8.0901	10.73	-1.4254	-53.64	-0.8046
5.36	4.0021	-59.00	7.8922	8.05	-1.5500	-56.32	-0.1226
2.68	3.7769	-61.69	6.5719	5.36	-1.4756	-59.00	-0.1444
0	4.1703	-64.37	4.6017	2.68	-1.4457	-61.69	-0.3047

Table B.9(d) Local Nusselt numbers for $s = 8$mm, $\phi = 45°$, top section
$p = 758.916$mmHg, $Ra = 13.033\times10^4$

Hot Plate				Cold Plate			
y (mm)	Nu	y (mm)	Nu	y (mm)	Nu	y (mm)	Nu
74.83	1.0982	0	1.5240	74.83	-4.3287	0	-3.2295
72.15	0.1262	-2.67	1.8876	72.15	-7.1050	-2.67	-3.4697
69.48	0.5233	-5.34	1.7817	69.48	-7.9478	-5.34	-3.3512
66.81	0.2031	-8.02	1.5854	66.81	-8.0865	-8.02	-3.3915
64.14	0.2892	-10.69	1.7578	64.14	-7.2507	-10.69	-3.4425
61.47	0.2171	-13.36	1.6750	61.47	-6.2035	-13.36	-3.0551
58.79	0.3965	-16.03	1.5691	58.79	-5.9802	-16.03	-2.8440
56.12	0.6376	-18.71	1.4285	56.12	-6.1318	-18.71	-2.8025
53.45	0.2212	-21.38	2.1420	53.45	-5.7972	-21.38	-2.5351
50.78	0.3406	-24.05	2.0263	50.78	-5.3868	-24.05	-2.9603
48.10	0.1746	-26.72	1.8315	48.10	-5.4135	-26.72	-3.3861
45.43	0.2088	-29.40	1.9486	45.43	-5.5376	-29.40	-3.1410
42.76	0.1679	-32.07	1.8680	42.76	-5.1939	-32.07	-3.2851
40.09	0.3637	-34.74	1.5661	40.09	-4.7651	-34.74	-3.2348
37.41	0.3997	-37.41	1.6874	37.41	-4.9275	-37.41	-3.0628
34.74	0.4679	-40.09	1.7263	34.74	-4.9703	-40.09	-2.7287
32.07	0.8624	-42.76	1.7424	32.07	-4.3953	-42.76	-2.8010
29.40	0.8413	-45.43	2.4927	29.40	-4.3680	-45.43	-2.5657
26.72	0.7122	-48.10	2.3305	26.72	-4.5500	-48.10	-2.7003
24.05	0.5502	-50.78	2.3689	24.05	-4.3329	-50.78	-2.8485
21.38	1.2292	-53.45	2.4964	21.38	-4.1261	-53.45	-2.5745
18.71	1.1724			18.71	-4.0593		
16.03	0.9958			16.03	-4.0930		
13.36	1.4372			13.36	-3.7869		
10.69	1.3238			10.69	-3.5552		
8.02	1.1888			8.02	-3.5140		
5.34	1.7403			5.34	-3.1890		
2.67	1.6487			2.67	-3.1701		

Table B.9(e) Local Nusselt numbers for s = 8mm, $\phi = 45°$, middle section
p = 758.916mmHg, $Ra = 12.963\times10^4$

Hot Plate				Cold Plate			
y (mm)	Nu	y (mm)	Nu	y (mm)	Nu	y (mm)	Nu
61.34	2.0112	-2.67	2.8451	61.34	-2.2411	-2.67	-2.1017
58.67	1.8172	-5.33	2.5789	58.67	-2.5284	-5.33	-2.0363
56.00	2.0804	-8.00	2.5685	56.00	-2.7901	-8.00	-1.9920
53.34	2.2379	-10.67	2.5330	53.34	-2.6112	-10.67	-2.3599
50.67	2.3243	-13.33	2.6402	50.67	-2.9278	-13.33	-2.6547
48.00	2.7011	-16.00	3.0201	48.00	-3.0162	-16.00	-2.3003
45.34	2.6176	-18.67	3.0440	45.34	-2.5610	-18.67	-2.4035
42.67	2.3029	-21.33	2.9623	42.67	-2.3707	-21.33	-2.4399
40.00	2.4257	-24.00	3.0560	40.00	-2.4117	-24.00	-1.7413
37.34	2.2374	-26.67	2.7285	37.34	-2.4863	-26.67	-1.8061
34.67	2.6888	-29.33	2.4978	34.67	-2.7643	-29.33	-2.1338
32.00	2.5173	-32.00	2.8869	32.00	-2.5130	-32.00	-2.0062
29.33	2.6967	-34.67	2.9406	29.33	-2.9120	-34.67	-2.3780
26.67	3.0247	-37.34	2.9245	26.67	-2.8389	-37.34	-2.6626
24.00	2.8643	-40.00	3.4867	24.00	-2.3457	-40.00	-2.1796
21.33	2.6212	-42.67	3.2368	21.33	-2.3215	-42.67	-2.3992
18.67	2.3944	-45.34	3.1476	18.67	-2.2336	-45.34	-2.2626
16.00	2.4233	-48.00	2.9354	16.00	-2.4383	-48.00	-1.7463
13.33	2.3433	-50.67	2.8284	13.33	-2.4352	-50.67	-1.7917
10.67	2.5196	-53.34	2.7235	10.67	-2.8005	-53.34	-1.9210
8.00	2.8700	-56.00	3.2555	8.00	-2.3066	-56.00	-1.8311
5.33	3.0928	-58.67	3.4420	5.33	-2.7359	-58.67	-2.0940
2.67	2.9557	-61.34	3.3986	2.67	-2.5713	-61.34	-2.4012
0	2.8278	-64.00	3.4804	0	-2.0831	-64.00	-1.9271
		-66.67	3.2129			-66.67	-2.1104
		-69.34	2.9427			-69.34	-2.0983
		-72.00	3.4156			-72.00	-1.6100
		-74.67	3.3109			-74.67	-1.6331
		-77.34	3.4881			-77.34	-1.4322

Table B.9(f) Local Nusselt numbers for s = 8mm, ϕ = 45°, bottom section
p = 761.258mmHg, Ra = 13.286×10^4

Hot Plate				Cold Plate			
y (mm)	Nu	y (mm)	Nu	y (mm)	Nu	y (mm)	Nu
64.32	2.9646	-2.68	4.1947	61.64	-2.0060	-2.68	-1.2977
61.64	2.8726	-5.36	4.3263	58.96	-2.2022	-5.36	-1.4318
58.96	3.0459	-8.04	4.4783	56.28	-2.0802	-8.04	-1.0843
56.28	2.8206	-10.72	4.4087	53.60	-2.2058	-10.72	-1.1872
53.60	2.8180	-13.40	4.7387	50.92	-1.8918	-13.40	-0.9196
50.92	3.0412	-16.08	4.8097	48.24	-1.9213	-16.08	-1.0575
48.24	3.0686	-18.76	4.9141	45.56	-1.9180	-18.76	-1.0472
45.56	3.3569	-21.44	5.0971	42.88	-1.5823	-21.44	-0.6608
42.88	3.3681	-24.12	5.2257	40.20	-1.7432	-24.12	-0.8053
40.20	3.1792	-26.80	5.1048	37.52	-1.6007	-26.80	-0.8674
37.52	3.3688	-29.48	5.4377	34.84	-1.8457	-29.48	-0.4699
34.84	3.0766	-32.16	5.5075	32.16	-1.9704	-32.16	-0.5230
32.16	2.9984	-34.84	6.0730	29.48	-1.6703	-34.84	-0.5429
29.48	3.3825	-37.52	6.8605	26.80	-1.7897	-37.52	-0.1761
26.80	3.4309	-40.20	6.6882	24.12	-1.8780	-40.20	-0.1480
24.12	4.0690	-42.88	7.0018	21.44	-1.4466	-42.88	-0.1306
21.44	3.6447	-45.56	6.6809	18.76	-1.5733	-45.56	-0.5997
18.76	3.5165	-48.24	6.4994	16.08	-1.5866	-48.24	-0.1334
16.08	3.8328	-50.92	6.2535	13.40	-1.4241	-50.92	-0.4046
13.40	3.6496	-53.60	6.1972	10.72	-1.5252	-53.60	-0.3144
10.72	3.6925	-56.28	5.8802	8.04	-1.2768	-56.28	-0.2121
8.04	3.8719	-58.96	6.8737	5.36	-1.4489	-58.96	-0.2157
5.36	3.9747	-61.64	6.1065	2.68	-1.6180	-61.64	-0.3332
2.68	4.0937	-64.32	4.5645	0	-1.1439	-64.32	-0.1373
0	4.3052						

Table B.9(g) Local Nusselt numbers for $s = 8$mm, $\phi = 90°$, top section
$p = 758.916$mmHg, $Ra = 13.007\times10^4$

Hot Plate				Cold Plate			
y (mm)	Nu	y (mm)	Nu	y (mm)	Nu	y (mm)	Nu
74.47	0.5336	0	0.4525	74.47	-3.1182	0	-3.0097
71.81	0.3231	-2.66	0.2001	71.81	-4.3799	-2.66	-3.0996
69.15	0.3030	-5.32	0.1535	69.15	-5.6158	-5.32	-2.7497
66.50	0.1875	-7.98	0.1560	66.50	-6.5218	-7.98	-2.7722
63.84	0.2305	-10.64	0.7101	63.84	-6.8146	-10.64	-2.8449
61.18	0.3215	-13.30	0.5022	61.18	-6.5378	-13.30	-2.8250
58.52	0.4594	-15.96	0.1839	58.52	-6.2555	-15.96	-2.8320
55.86	0.2216	-18.62	0.2272	55.86	-6.2665	-18.62	-2.4837
53.20	0.4506	-21.28	0.8221	53.20	-6.1603	-21.28	-2.6219
50.54	2.0501	-23.94	0.7829	50.54	-5.4024	-23.94	-2.6006
47.88	1.1021	-26.60	0.6062	47.88	-5.1575	-26.60	-2.6498
45.22	0.6783	-29.26	0.3625	45.22	-4.7026	-29.26	-2.3175
42.56	0.5523	-31.92	0.1653	42.56	-4.3959	-31.92	-2.3162
39.90	0.1996	-34.58	0.9273	39.90	-4.5791	-34.58	-2.3891
37.24	0.1395	-37.24	0.8148	37.24	-4.4539	-37.24	-2.4331
34.58	0.1522	-39.90	0.7144	34.58	-3.8888	-39.90	-2.1406
31.92	0.8091	-42.56	0.5428	31.92	-3.7488	-42.56	-2.0731
29.26	0.3531	-45.22	0.1620	29.26	-3.8128	-45.22	-2.1987
26.60	0.1658	-47.88	1.0293	26.60	-3.4803	-47.88	-2.2965
23.94	0.1909	-50.54	0.9365	23.94	-3.6730	-50.54	-1.8696
21.28	0.2376	-53.20	0.7303	21.28	-3.4775	-53.20	-1.9735
18.62	0.1536			18.62	-3.1840		
15.96	0.9316			15.96	-3.1685		
13.30	0.2815			13.30	-3.2652		
10.64	0.1924			10.64	-3.4033		
7.98	0.1492			7.98	-3.3345		
5.32	0.1548			5.32	-2.9459		
2.66	0.4417			2.66	-3.0391		

Table B.9(h) Local Nusselt numbers for $s = 8$mm, $\phi = 90°$, middle section
$p = 758.916$mmHg, $Ra = 13.165\times10^4$

Hot Plate				Cold Plate			
y (mm)	Nu	y (mm)	Nu	y (mm)	Nu	y (mm)	Nu
64.06	1.6014	-2.67	2.3284	64.06	-2.8625	-2.67	-1.9453
61.39	1.5782	-5.34	2.4508	61.39	-2.8734	-5.34	-1.9946
58.72	1.5402	-8.01	2.4376	58.72	-2.7273	-8.01	-2.0078
56.05	1.7433	-10.68	2.3328	56.05	-2.5167	-10.68	-1.9785
53.38	1.6993	-13.35	2.3574	53.38	-2.5224	-13.35	-1.7976
50.71	1.7299	-16.02	2.2846	50.71	-2.4184	-16.02	-1.7861
48.05	1.7349	-18.68	2.6280	48.05	-2.6156	-18.68	-1.7123
45.38	1.7045	-21.35	2.4598	45.38	-2.5520	-21.35	-1.7497
42.71	1.7103	-24.02	2.4906	42.71	-2.4982	-24.02	-1.8331
40.04	1.9248	-26.69	2.5336	40.04	-2.2940	-26.69	-1.7910
37.37	1.9121	-29.36	2.5844	37.37	-2.4473	-29.36	-1.6814
34.70	1.9339	-32.03	2.5443	34.70	-2.3624	-32.03	-1.6127
32.03	1.9710	-34.70	2.5702	32.03	-2.3482	-34.70	-1.6128
29.36	1.9212	-37.37	2.5230	29.36	-2.4676	-37.37	-1.5771
26.69	1.9497	-40.04	2.8261	26.69	-2.3895	-40.04	-1.6175
24.02	1.8775	-42.71	2.8364	24.02	-2.4011	-42.71	-1.5694
21.35	1.9369	-45.38	2.7221	21.35	-2.1595	-45.38	-1.6142
18.68	2.1171	-48.05	2.7603	18.68	-2.1123	-48.05	-1.6399
16.02	2.1073	-50.71	2.9535	16.02	-2.0833	-50.71	-1.5999
13.35	2.1503	-53.38	2.8006	13.35	-2.2258	-53.38	-1.3932
10.68	2.1017	-56.05	2.8507	10.68	-1.8136	-56.05	-1.3645
8.01	2.1486	-58.72	3.0533	8.01	-2.2092	-58.72	-1.4049
5.34	2.2009	-61.39	2.8422	5.34	-2.1874	-61.39	-1.3635
2.67	2.0951	-64.06	3.1645	2.67	-1.8803	-64.06	-1.4111
0	1.9430	-66.73	3.0408	0	-1.9399	-66.73	-1.4440
		-69.40	2.9654			-69.40	-1.1425
		-72.07	3.1122			-72.07	-1.1724
		-74.74	3.1662			-74.74	-1.2548
		-77.41	3.6802			-77.41	-1.2861

Table B.9(i) Local Nusselt numbers for $s = 8$mm, $\phi = 90°$, bottom section
$p = 761.258$mmHg, $Ra = 13.038\times10^4$

Hot Plate				Cold Plate			
y (mm)	Nu	y (mm)	Nu	y (mm)	Nu	y (mm)	Nu
61.55	2.3455	-2.68	3.7225	61.55	-0.0906	-2.68	-0.2209
58.87	2.7460	-5.35	3.7567	58.87	-0.9045	-5.35	-0.2219
56.20	2.5753	-8.03	3.4164	56.20	-1.0460	-8.03	-0.1927
53.52	2.4506	-10.70	3.5925	53.52	-0.6887	-10.70	-0.1341
50.84	2.7461	-13.38	3.4453	50.84	-0.8673	-13.38	-0.3505
48.17	2.6821	-16.06	3.4389	48.17	-0.2702	-16.06	-0.3872
45.49	2.6300	-18.73	3.7911	45.49	-0.6771	-18.73	-0.2607
42.82	2.9277	-21.41	3.5272	42.82	-0.8470	-21.41	-0.2660
40.14	2.6876	-24.08	4.0360	40.14	-0.2650	-24.08	-0.1368
37.46	3.0662	-26.76	3.7975	37.46	-0.6399	-26.76	-0.1973
34.79	2.9172	-29.44	3.8238	34.79	-0.1658	-29.44	-0.1804
32.11	2.8980	-32.11	4.0520	32.11	-0.1142	-32.11	-0.6411
29.44	3.0995	-34.79	3.9333	29.44	-0.5970	-34.79	-0.2948
26.76	2.9706	-37.46	4.1742	26.76	-0.1735	-37.46	-0.4254
24.08	2.9586	-40.14	4.0341	24.08	-0.2670	-40.14	-1.5453
21.41	3.2724	-42.82	4.2153	21.41	-0.4954	-42.82	-0.4530
18.73	3.2400	-45.49	4.8364	18.73	-0.1832	-45.49	-0.6046
16.06	3.1217	-48.17	4.5655	16.06	-0.1479	-48.17	-1.0019
13.38	3.5546	-50.84	4.4374	13.38	-0.1738	-50.84	-0.3712
10.70	3.4813	-53.52	5.0850	10.70	-0.4175	-53.52	-0.1436
8.03	3.4742	-56.20	4.8702	8.03	-0.2329	-56.20	-0.4891
5.35	3.7539	-58.87	4.7766	5.35	-0.1760	-58.87	-0.2735
2.68	3.8320	-61.55	4.3304	2.68	-0.4271	-61.55	-0.3050
0	3.4960	-64.22	2.7325	0	-0.1778		

Appendix C

SAMPLE CALCULATIONS

A typical set of experimental calculations is provided to demonstrate how the heat transfer results were obtained. The local Nusselt number calculations are for the finite fringe interferogram shown in Figure 4.1(a), for s = 2mm and $\phi = 0°$ at y = 100.0mm on the hot plate.

C.1 Given Data

Average hot plate surface temperature ($T_{s,h}$)	307.95K
Average cold plate surface temperature ($T_{s,c}$)	288.06K
Ambient pressure (p)	101310.2Pa
Plate length in beam direction (Z)	0.3556m
Actual width of cavity block (W_{actual})	0.0287m
Width of cavity on scale photo (W_{photo})	0.0213m
Distance from plate surface to first fringe ($x_{1,photo}$)	0.308mm
Distance from plate surface to second fringe ($x_{2,photo}$)	0.689mm
Gravitational acceleration (g)	9.81m/s^2
Ideal gas constant for air (R)	287J/kg·K
Wavelength of He-Ne laser (λ)	6.328×10^{-7}m
Gladstone-Dale constant for air with He-Ne laser (G)	0.226×10^{-3}m^3/kg

C.2 Air Properties

Film temperature (T_f)

$$T_f = \frac{T_{s,h} + T_{s,c}}{2}$$

$$= \frac{307.95 + 288.06}{2}$$

$$= 298.01\text{K}$$

Volumetric Expansion Coefficient (β)

$$\beta = \frac{1}{T_f}$$

$$= \frac{1}{298.01}$$

$$= 3.356\times10^{-3}\text{K}^{-1}$$

Density (ρ)

From the ideal gas law:

$$\rho = \frac{p}{RT_f}$$

$$= \frac{101310.2}{(287)(298.01)}$$

$$= 1.185\text{kg/m}^3$$

Dynamic Viscosity (μ)

By linear interpolation [74] evaluated at $T_f = 298.01$K:

$$\mu = 18.4343\times10^{-6}\text{kg/m·s}$$

Thermal Conductivity at Surface Temperature (k_s)

By linear interpolation [75] evaluated at $T_{s,h} = 307.95$K:

$$k_s = 26.72\times10^{-3}\text{W/m·K}$$

Thermal Conductivity at Film temperature (k_f)

By linear interpolation [76] evaluated at $T_f = 298.01$K:

$$k_f = 25.99\times10^{-3}\text{W/m·K}$$

Specific Heat (C_p)

From equation (A.1) where $T_f = 298.01$K:

$$C_p = 1044.66 - 3.15967\times10^{-1}T_f + 7.07908\times10^{-4}T_f^{\,2} - 2.7034\times10^{-7}T_f^{\,3}$$

$$C_p = 1044.66 - 3.15967\times10^{-1}(298.01) + 7.07908\times10^{-4}(298.01)^2 - 2.7034\times10^{-7}(298.01)^3$$

$$= 1006.2\text{J/kg·K}$$

C.3 Rayleigh Number Based On Cavity Width

From equation (3.2):

$$Ra = \frac{g\beta(T_{s,h} - T_{s,c})W^3\rho^2C_p}{\mu k}$$

$$Ra = \frac{(9.81)(3.356\times10^{-3})(307.95 - 288.06)(0.0287)^3(1.185)^2(1006.2)}{(18.4343\times10^{-6})(25.99\times10^{-3})}$$

$$= 4.560\times10^4$$

C.4 Local Heat Transfer Coefficient

Scale Factor (SF_x)

$$SF_x = \frac{W_{actual}}{W_{photo}}$$

$$= \frac{0.0287}{0.0213}$$

$$= 1.345$$

Fringe Shift (ε)

$$x_{1,actual} = SF_x(x_{1,photo})$$

$$= 1.345(0.308)$$

$$= 0.414\text{mm}$$

$$x_{2,actual} = SF_x(x_{2,photo})$$

$$= 1.345(0.689)$$

$$= 0.927\text{mm}$$

By linear extrapolation:

$$\frac{\varepsilon_1}{\Delta\varepsilon} = \frac{x_1}{\Delta x}$$

$$\frac{\varepsilon_1}{1} = \frac{0.414}{0.927 - 0.414}$$

$$\varepsilon_1 = 0.808$$

$$\varepsilon_2 = \varepsilon_1 + 1 = 1.808$$

Fringe Temperature (T)

From equation (3.18):

$$T = \frac{T_{s,h}}{\frac{\varepsilon R \lambda T_{s,h}}{GpZ} + 1}$$

$$T_1 = \frac{307.95}{\frac{(0.808)(287)(6.328\times10^{-7})(307.95)}{(0.226\times10^{-3})(101310.2)(0.3556)} + 1}$$

$$= 306.25\text{K}$$

$$T_2 = \frac{307.95}{\frac{(1.808)(287)(6.328\times10^{-7})(307.95)}{(0.226\times10^{-3})(101310.2)(0.3556)} + 1}$$

$$= 304.17\text{K}$$

Temperature Gradient (dT/dx)

$$\left.\frac{dT}{dx}\right|_{x=0} = \frac{T_2 - T_1}{x_2 - x_1}$$

$$= \frac{304.17 - 306.25}{(0.927 - 0.414)\times10^{-3}}$$

$$= -4054\text{K/m}$$

Local Convection Coefficient (h)

From equation (3.20):

$$h = \frac{-k_s \left.\frac{dT}{dx}\right|_{x=0}}{(T_{s,h} - T_{s,c})}$$

$$h = \frac{-(26.72\times10^{-3})(-4054)}{307.95 - 288.06}$$

$$= 5.45\text{W/m}^2\cdot\text{K}$$

C.5 Local Nusselt Number

From equation (3.21):

$$Nu = \frac{hW}{k_f}$$

$$Nu = \frac{(5.45)(0.0287)}{25.99\times10^{-3}}$$

$$= 6.02$$

C.6 Average Nusselt Number

The average Nusselt number (Nu_{avg}) was calculated by numerically integrating the local values over the span of the plate using the trapezoidal rule. For the case of the interferogram in this sample calculation, i.e. for s = 2mm and ϕ = 0° on the hot plate:

$$Nu_{avg} = \frac{1}{Y}\left[\left(\frac{\Delta Y}{2}\right)_1 (Nu_1 + Nu_0) + \left(\frac{\Delta Y}{2}\right)_2 (Nu_2 + Nu_1) + \cdots + \left(\frac{\Delta Y}{2}\right)_n (Nu_n + Nu_{n-1})\right]$$

$$Nu_{avg} = \frac{1}{380.3}\left[\left(\frac{2.7031}{2}\right)(3.0393 + 2.1268) + \left(\frac{2.7031}{2}\right)(2.6070 + 3.0393) + \cdots + \left(\frac{2.6911}{2}\right)(0.7561 + 0.8741)\right]$$

$$Nu_{avg} = 2.89$$

Appendix D

ERROR ANALYSIS

Just like any other experiment, this study with a Mach-Zehnder interferometer had a certain degree of uncertainty. A thorough discussion of the probable sources of error pertaining to heat transfer measurements can be found in Machin's thesis [35]. The relevant sources of error and the amount of uncertainty associated with each are summarized in Table D.1.

Table D.1 Summary of sources of uncertainty

Quantity	Absolute Uncertainty	Percent Uncertainty
Ambient pressure (p)	± 66.64 Pa	±0.06%
Plate surface temperature ($T_{s,h}$, $T_{s,c}$)	± 0.6 K	±1.7%, ±4%
Optical length of plate (Z)	± 0.005 m	±1.5%
Fringe distance (Δx)	± 0.1(Δx) m	
Fringe shift (ε)	± 0.1($\Delta x/W$)	
Film temperature (T_f)	± 0.6 K	±0.2%
Temperature difference (ΔT)	± 0.6 K	±3%
Cavity width (W)	± 0.0002 m	±0.05%
Specific heat (C_p)		±0.25%
Dynamic Viscosity (μ)		±0.5%
Thermal Conductivity (k)		±1%

The uncertainty in fringe shift error accounts for the slight misalignments that may have occurred in the finite fringe mode. When setting the finite fringe pattern with the model at ambient temperature, the optics were aligned such that horizontal fringes, equally spaced at a distance d, appeared perpendicular with the plate surfaces. In this

way, there will be no fringe shifts as the temperature remains unchanged across the cavity. If the beam became slightly misaligned at the time the interferogram was taken, there would be artificial fringe crossings that would result in a fringe shift error.

In a preliminary study, it was found that for a fringe spacing of d = 1mm, there would be a maximum fringe offset of 0.1mm across the width of the cavity, W. Thus, the uncertainty in fringe shift error, $\delta\varepsilon$, associated with a fringe distance measurement, Δx, can be determined by the following relationship:

$$\frac{\delta\varepsilon}{\Delta x} = \frac{0.1/d}{W} \tag{D.1}$$

where d, Δx, and W are in [mm].

The error analysis for this study was conducted based on the Kline and McClintock method [77]. Consider an experimental result, R, calculated from n independent variables, x_1, x_2,... , x_n, with random uncertainties of δx_1, δx_2,... δx_n, respectively. If each of the parameters were assumed to have the same odds, then the uncertainty in the result, δR, is given as follows:

$$\delta R = \sqrt{\left(\frac{\partial R}{\partial x_1}\delta x_1\right)^2 + \left(\frac{\partial R}{\partial x_2}\delta x_2\right)^2 + \ldots + \left(\frac{\partial R}{\partial x_n}\delta x_n\right)^2} \tag{D.2}$$

For the case where R can be expressed as a product of the variables, each raised to some power, so that:

$$R = x_1^a x_2^b \ldots x_n^z \tag{D.3}$$

Then, the relative uncertainty can be calculated as:

$$\frac{\delta R}{R} = \sqrt{\left(a\frac{\delta x_1}{x_1}\right)^2 + \left(b\frac{\delta x_2}{x_2}\right)^2 + \ldots + \left(z\frac{\delta x_n}{x_n}\right)^2} \tag{D.4}$$

D.1 Uncertainty in Local Nusselt Number

Based on the method described above, for the local Nusselt number given in equation (3.21), the uncertainty in the heat transfer result would be given as follows:

$$\partial Nu = \sqrt{\left(\frac{\partial Nu}{\partial p}\delta p\right)^2 + \left(\frac{\partial Nu}{\partial T_{s,h}}\delta T_{s,h}\right)^2 + \left(\frac{\partial Nu}{\partial Z}\delta Z\right)^2 + \left(\frac{\partial Nu}{\partial(\Delta x)}\delta(\Delta x)\right)^2 + \left(\frac{\partial Nu}{\partial \varepsilon}\delta\varepsilon\right)^2 + \left(\frac{\partial h}{\partial T_{s,c}}\delta T_{s,c}\right)^2 + \left(\frac{\partial Nu}{\partial W}\delta W\right)^2} \tag{D.5}$$

The fringe temperature difference is optically determined by:

$$T_1 - T_2 = \frac{T_{s,h}}{\frac{2\varepsilon_1 R\lambda T_{s,h}}{3GLp}+1} - \frac{T_{s,h}}{\frac{2(\varepsilon_1+\Delta\varepsilon)R\lambda T_{s,h}}{3GLp}+1} \tag{D.6}$$

where ε_1 is the fractional fringe shift from the plate surface to the first measured fringe, and $\Delta\varepsilon$ is the fringe shift between the first and second fringes. From fringe centre to fringe centre, $\Delta\varepsilon = 1$. The value of ε_1 normally lies between 0 and 1. For convenience, let $\varepsilon_1 = 0$. Equation (D.6) simplifies to:

$$T_1 - T_2 = T_{s,h} - \frac{T_{s,h}}{\frac{2\varepsilon R\lambda T_{s,h}}{3GLp}+1} \tag{D.7}$$

Therefore, the experimental temperature gradient is calculated as:

$$\left.\frac{dT}{dx}\right|_{x=0} = \frac{T_{s,h} - \frac{T_{s,h}}{\frac{2\varepsilon R\lambda T_{s,h}}{3GLp}+1}}{\Delta x} \tag{D.8}$$

Combining equations (3.21) and (D.8), the local Nusselt number can be expressed as:

$$Nu = \frac{k_s\left(T_{s,h} - \dfrac{T_{s,h}}{\dfrac{2\varepsilon R\lambda T_{s,h}}{3GLp}+1}\right)W}{k_f \Delta x(T_{s,h} - T_{s,c})} \tag{D.9}$$

From equation (D.9), the following partial derivatives were obtained using mathematics software Maple [78]. Note that the uncertainty in the conductivity ratio of air at the surface and film temperatures (k_s/k_f) is assumed to be negligible, and has been omitted from the differential equation.

$$\frac{\partial Nu}{\partial p} = \frac{2\varepsilon R\lambda T_{s,h}^2 W}{3\left(\dfrac{2\varepsilon R\lambda T_{s,h}}{3GLp}+1\right)^2 GLp^2 \Delta x(T_{s,h} - T_{s,c})} \tag{D.10}$$

$$\frac{\partial Nu}{\partial T_{s,h}} = \frac{\left(1 - \dfrac{1}{\dfrac{2\varepsilon R\lambda T_{s,h}}{3GLp}+1} + \dfrac{2\varepsilon R\lambda T_{s,h}}{3\left(\dfrac{2\varepsilon R\lambda T_{s,h}}{3GLp}+1\right)^2 GLp}\right)W}{\Delta x(T_{s,h} - T_{s,c})} - \frac{\left(T_{s,h} - \dfrac{T_{s,h}}{\dfrac{2\varepsilon R\lambda T_{s,h}}{3GLp}+1}\right)W}{\Delta x(T_{s,h} - T_{s,c})^2} \tag{D.11}$$

$$\frac{\partial Nu}{\partial L} = \frac{2\varepsilon R\lambda T_{s,h}^2 W}{3\left(\dfrac{2\varepsilon R\lambda T_{s,h}}{3GLp}+1\right)^2 GL^2 p\Delta x(T_{s,h} - T_{s,c})} \tag{D.12}$$

$$\frac{\partial Nu}{\partial(\Delta x)} = -\frac{\left(T_{s,h} - \dfrac{T_{s,h}}{\dfrac{2\varepsilon R\lambda T_{s,h}}{3GLp}+1}\right)W}{\Delta x^2(T_{s,h} - T_{s,c})} \tag{D.13}$$

$$\frac{\partial Nu}{\partial \varepsilon} = \frac{2R\lambda T_{s,h}^2 W}{3\left(\dfrac{2\varepsilon R\lambda T_{s,h}}{3GLp}+1\right)^2 GLp\Delta x(T_{s,h} - T_{s,c})} \tag{D.14}$$

$$\frac{\partial h}{\partial T_{s,c}} = \frac{\left(T_{s,h} - \frac{T_{s,h}}{\frac{2\varepsilon R\lambda T_{s,h}}{3GLp}+1} \right) W}{\Delta x (T_{s,h} - T_{s,c})^2} \tag{D.15}$$

$$\frac{\partial Nu}{\partial W} = -\frac{\left(T_{s,h} - \frac{T_{s,h}}{\frac{2\varepsilon R\lambda T_{s,h}}{3GLp}+1} \right)}{\Delta x (T_{s,h} - T_{s,c})} \tag{D.16}$$

The error for each heat transfer result was calculated by substituting equations (D.10) to (D.16) into equation (D.5) and using the numbers specified in Table D.1. In general, the average uncertainty in local Nusselt number was about 7%.

D.2 Uncertainty in Rayleigh number

The Rayleigh number based on cavity width can be written as follows:

$$Ra = \frac{g\Delta T W^3 p^2 C_p}{T_f^3 R^2 \mu k} \tag{D.17}$$

Applying equation (D.17) to equation (D.4), the relative uncertainty in Rayleigh number can be defined as:

$$\frac{\delta Ra}{Ra} = \sqrt{\left(\frac{\delta(\Delta T)}{\Delta T}\right)^2 + \left(3\frac{\delta W}{W}\right)^2 + \left(2\frac{\delta p}{p}\right)^2 + \left(\frac{\delta C_p}{C_p}\right)^2 + \left(3\frac{\delta T_f}{T_f}\right)^2 + \left(\frac{\delta \mu}{\mu}\right)^2 + \left(\frac{\delta k}{k}\right)^2} \tag{D.18}$$

Substituting the values from Table D.1 into equation (D.18) gives an uncertainty in Rayleigh number of ±3.6%.

References

1. Wright, J.L., 1992, "Glazing System Thermal Analysis," *CANMET, Advanced Glazing System Laboratory,* VISION3, Minister of Supply and Services Canada, University of Waterloo.

2. Finlayson, E.U., Arasteh, D.K., Huizenga, C., Rubin, M.D., and Reilly, M.S., "WINDOW 4.0: Documentation of Calculation Procedures," Energy and Environmental Division, Lawrence Berkeley Laboratory, Berkeley, California.

3. Ostrach, S., 1952, "Natural Convection in Enclosures," *Advances in Heat Transfer,* Vol. 8, pp. 161–227.

4. Wright, J.L. and Sullivan, H.F., 1989, "Natural Convection in Sealed Glazing Units: A Review," *ASHRAE Transactions: Technical and Symposium Papers,* Vol. 95, Part 1, pp. 592–603.

5. Batchelor, G.K., 1954, "Heat Transfer by Free Convection across a Closed Cavity between Vertical Boundaries at Different Temperatures," *Quarterly of Applied Mathematics,* Vol. 12, no. 3, pp. 209–233.

6. Eckert, E.R.G. and Carlson, W.O., 1961, "Natural Convection in an Air Layer Enclosed Between Two Vertical Plates with Different Temperatures," *International Jounral of Heat and Mass Transfer,* Vol. 2, pp. 106–120.

7. Elder, J.W., 1965, "Laminar Free Convection in a Vertical Slot," *Journal of Fluid Mechanics,* Vol. 23, Part 1, pp. 77–98.

8. Elder, J.W., 1965, "Turbulent Free Convection in a Vertical Slot," *Journal of Fluid Mechanics,* Vol. 23, Part 1, pp. 99–111.

9. Vest, C.M. and Arpaci, V.S., 1969, "Stability of Natural Convection in a Vertical Slot," *Journal of Fluid Mechanics,* Vol. 36, Part 1, pp. 1–15.

10. Seki, N., Fukusako, S., and Inaba, H., 1978, "Visual Observation of Natural Convective Flow in a Narrow Vertical Cavity," *Journal of Fluid Mechanics,* Vol. 84, Part 4, pp. 695–704.

11. Yin, S.H., Wung, T.Y., and Chen, K., 1978, "Natural Convection in an Air Layer Enclosed within Rectangular Cavities," *International Journal of Heat and Mass Transfer,* Vol. 21, pp. 307–315.

12. Papple, M.L.C., Tarasuk, J.D., 1987, "An Interferometric Study of Developing Natural Convective Flow in Inclined Isothermal Ducts," *Proceedings of the AIAA 22nd Thermophysics Conference,* AIAA-87–1589.

13. Randall, K.R., Mitchell, J.W., and El-Wakil, M.M., 1979, "Natural Convection Heat Transfer Characteristics of Flat Plate Enclosure," *Transactions of the ASME Journal of Heat Transfer,* Vol. 101, pp.120–125.

14. ElSherbiny, S.M., Raithby, G.D., and Hollands, K.G.T., 1982, "Heat Transfer by Natural Convection across Vertical and Inclined Air Layers," *Transactions of the ASME Journal of Heat Transfer,* Vol. 104, pp. 96–102.

15. ElSherbiny, S.M., Hollands, K.G.T., and Raithby, G., 1982, "Effect of Thermal Boundary Conditions on Natural Convection in Vertical and Inclined Air Layers." *Transactions of the ASME Journal of Heat Transfer,* Vol. 104, pp. 515–520.

16. Shewen, E., Hollands, K.G.T., and Raithby, G.D., 1996, "Heat Transfer by Natural Convection across a Vertical Air Cavity of Large Aspect Ratio," *Transactions of the ASME Journal of Heat Transfer,* Vol. 118, pp. 993–995.

17. Gill, A.E., 1966, "The Boundary-Layer Regime for Convection in a Rectangular Cavity," *Journal of Fluid Mechanics,* Vol. 26, Part 3, pp. 515–536.

18. Bejan, A., 1979, "Note on Gill's Solution for Free Convection in a Vertical Enclosure," *Journal of Fluid Mechanics,* Vol. 90, Part 3, pp. 561–568.

19. Raithby, G.D., Hollands, K.G.T., and Unny, T.E., 1977, "Analysis of Heat Transfer by Natural Convection Across Vertical Fluid Layers," *Transactions of the ASME Journal of Heat Transfer,* Vol. 99, pp. 287–293.

20. Zenouzi, M. and Yener, Y., 1992, "Simultaneous Radiation and Natural Convection in Vertical Slots," *Developments in Radiative Heat Transfer, Proceedings of the 28th National Heat Transfer Conference,* Vol. 203, pp. 179–186.

21. Newell, M.E. and Schmidt, F.W., 1970, "Heat Transfer by Natural Convection within Rectangular Enclosures," *Journal of Heat Transfer,* Series C, Vol. 92, pp. 159–168.

22. Bergholz, R.F., 1978, "Instability of Steady Natural Convection in a Vertical Fluid Layer," *Journal of Fluid Mechanics,* Vol. 84, Part 4, pp. 743–768.

23. Jones, I.P., 1979, "A Numerical Study of Natural Convection in an Air-Filled Cavity: Comparison with Experiment," *Numerical Heat Transfer,* Vol. 2, pp. 193–213.

24. Raithby, G.D. and Wong, H.H., 1981, "Heat Transfer by Natural Convection across Vertical Air Layers," *Numerical Heat Transfer,* Vol. 4, pp. 447–457.

25. Lee, Y. and Korpela, S.A., 1983, "Multi-cellular natural convection in a vertical slot," *Journal of Fluid Mechanics,* vol. 126, pp. 99-121.

26. Chait, A. and Korpela, S.A., 1989, "The Secondary Flow and Its Stability for Natural Convection in a Tall Vertical Enclosure," *Journal of Fluid Mechanics,* vol. 200, pp. 189-216.

27. Ramanan, N. and Korpela, S.A., 1989, "Multigrid Solution of Natural Convection in a Vertical Slot," *Numerical Heat Transfer,* Vol. 15, Part A, pp. 323–339.

28. Jin, Y.Y., Chen, C.F., 1996, "Natural Convection of High Prandtl Number Fluids with Variable Viscosity in a Vertical Slot," *International Journal of Heat and Mass Transfer,* Vol 39, No. 13, pp. 2663–2670.

29. Jin, Y.Y. and Chen, C.F., 1996, "Instability of Convection and Heat Transfer of High Prandtl Number Fluids in a Vertical Slot" *Transactions of the ASME Journal of Heat Transfer,* vol. 118, pp. 359-365.

30. Korpela, S.A., Lee, Y., and Drummond, J.E., 1982, "Heat Transfer through a Double Pane Windows," *Transactions of the ASME Journal of Heat Transfer,* Vol. 104, pp. 539–544.

31. Curcija, D. and Goss, W., 1994, "Two-Dimensional Finite-Element Model of Heat Transfer in Complete Fenestration Systems," *ASHRAE Transactions: Technical and Symposium Papers,* Vol. 100, Part 2, pp. 1207–1221.

32. Wright, J.L. and Sullivan, H.F., 1994, "A Two-Dimensional Numerical Model for Natural Convection in a Vertical, Rectangular Window Cavity," *ASHRAE Transactions: Technical and Symposium Papers,* Vol. 100, Part 2, pp. 1193–1206.

33. Wright, J.L. and Sullivan, H.F., 1995, "A Two-Dimensional Numerical Model for Glazing System Thermal Analysis," *ASHRAE Transactions,* Vol. 101, Part 1, pp. 819–831.

34. Wright, J.L., 1996, "A Correlation to Quantify Convective Heat Transfer between Vertical Window Glazings," *ASHRAE Transactions: Technical and Symposium Papers,* pp. 940-946.

35. Machin, A.D., 1997, "An Experimental Study of Free Convective Heat Transfer from a Vertical Flat Plate in the Presence of Louvers," M.E.Sc. Thesis, University of Western Ontario.

36. Machin, A.D., 1998, "Experimental Study of Free Convective Heat Transfer at an Indoor Glazing Surface with a Venetian Blind," *ASHRAE Internation Journal of HVAC&R Research,* Vol. 4, No. 2, pp. 153–166.

37. Ye, P., 1997, "Effect of Venetian Blinds on Overall Heat Transfer through Window Systems: A Finite Element Numerical Solution," M.E.Sc. Thesis, Queen's University.

38. Phillips, J., 1999, "A Numerical Study of the Effects of Venetian Blinds on Radiation and Convection Heat Transfer from a Window Glazing," M.E.Sc. Thesis, University of Western Ontario.

39. Phillips, J., Naylor, D., Harrison, S.J., Oosthuizen, P.H., 1999, "Free Convection from a Window Glazing with a Venetian Blind: Numerical Model Development," *Transactions of the CSME,* vol. 23, no. 1B, pp. 159–172.

40. Phillips, J., Naylor, D., Oosthuizen, P.H., and Harrison, S.J., "Modeling of the Conjugate Heat Transfer from a Window Adjacent to a Louvered Shade," *Advanced Computational Methods in Heat Transfer VI,* Wit press, Boston, pp. 127–136.

41. Duarte, N., 2000, "An Experimental Study of Free Convective Heat Transfer from a Vertical Plate in the Presence of Heated Venetian Blinds," M.E.Sc. Thesis, University of Western Ontario.

42. Naylor, D. and Duarte, N., 1999, "Direct Temperature Gradient Measurement Using Interferometry," *Experimental Heat Transfer,* vol. 12, pp. 279–294.

43. Collins, M., Harrison, S.J., Naylor, D., and Ooosthuizen, P.H., 2001, "An Interferometric Study of Convective Heat Transfer from an Irradiated Complex Window Assembly," *Proceedings of IMECE 2001,* 2001 International Mechanical Engineering Congress and Exposition, New York.

44. Collins, M., Harrison, S.H., Naylor, D., and Ooosthuizen, P.H., 2002, "Heat Transfer from an Isothermal Vertical Surface with Adjacent Heated Horizontal Louvers: Numerical Analysis," *Transactions of the ASME Journal of Heat Transfer,* vol. 124, pp. 1072–1077.

45. Collins, M., Harrison, S.H., Naylor, D., and Ooosthuizen, P.H., 2002, "Heat Transfer from an Isothermal Vertical Surface with Adjacent Heated Horizontal Louvers: Validation," *Transactions of the ASME Journal of Heat Transfer,* vol. 124, pp. 1078–1087.

46. Oosthuizen, P.H., Sun, L. and Naylor, D., 2002, "A Numerical Study of the Effect of Normal Adiabatic Surfaces on Natural Convective Heat Transfer from a Vertical Isothermal Plate," *Progress in Transport Phenomena, Proceedings of the 13th International Symposium on Transport Phenomena,* pp. 327–331.

47. Oosthuizen, P.H., Sun, L., and Naylor, D., 2002, "The Effect of Inclined Vertical Slats on Natural Convective Heat Transfer from an Isothermal Heated Vertical Plate," *Proceedings of the 10th Annual meeting of CFA Society of Canada 2002,* pp. 515–519.

48. Shahid, H., Naylor, D., and Lai, B.Y., 2003, "A Finite Volume Study of a Single Glazed Window with a Venetian Blind Attachment," *Proceedings of the 19th Canadian Congress of Applied Mechanics*, pp. 386–387.

49. Shahid, H. and Naylor, D., 2003, "Thermal Simulations of a Fenestration with Horizontal Venetian Blind," *Proceedings of APM2002,* 3rd International Conference on Computational Heat and Mass Transfer, Banff.

50. Kelkar, K.M., and Patankar, S.V., 1990, "Numerical Prediction of Natural Convection in Square Partitioned Enclosures," *Numerical Heat Transfer,* Vol. 1, Part A, pp. 269–285.

51. Mezrhab, A., Bchir, L., 1999, "Radiation-Natural Convection Interactions in Partitioned Cavities," *International Journal of Numerical Methods for Heat and Fluid Flow,* Vol. 9, No. 1, pp. 186–203.

52. Smith, T.F., Beckermann, C., and Adams, C.C., 1993, "A Numerical Simulation Model for Studying the Thermal Performance of Windows," *ASHRAE Transactions: Technical and Symposium Papers,* Vol. 99, Part 2, pp. 585–596.

53. Fang, X.D., 2000, "A Study of the U-factor of the Window with a High-Reflectivity Venetian Blind," *Solar Energy,* Vol. 68, No. 2, pp. 207–214.

54. Garnet, J.M., Fraser, R.A., Sullivan, H.F., and Wright, J.L., 1995, "Effect of Internal Venetian Blinds on Window Center-Glass U-Values," *Proceedings of the Window Innovations 95.*

55. Rheault, S. and Bilgen, E., 1989, "Heat Transfer Analysis in an Automated Venetian Blind Window System," *Transactions of the ASME Journal of Solar Energy Engineering,* Vol. 111, pp. 89–95.

56. Zhang, Z., Bejan, A., and Lage, J.L., 1991, "Natural Convection in a Vertical Enclosure with Internal Permeable Screen," *Transactions of the ASME Journal of Heat Transfer,* Vol. 113, pp. 337–383.

57. Cho, S.H., Shin, K.S., and Zaheer-Uddin, M., 1995, "The effect of Slat Angle of Windows with Venetian Blinds on Heating and Cooling Loads of Buildings in South Korea," *Energy*, Vol. 20, No. 12, pp. 1225–1236.

58. Breitenbach, J., Lart, S., Längle, I., and Rosenfeld, J.L.J., 2001, "Optical and thermal performance of glazing with integral Venetian blinds," *Energy and Buildings,* Vol. 33, pp. 433–442.

59. Naylor, D. and Collins, M., 2004, "Evaluation of an Approximate Method for Predicting the U-Value of a Window with a Between-Panes Louvered Shade," *Proceedings of CHT-04,* International Symposium on Advances in Computational Heat Transfer, Norway.

60. Eckert, E.R.G. and Goldstein, R.J., 1976, *Measurements in Heat Transfer,* Hemisphere Publishing Corp.

61. Naylor, D., 2003, "Recent Developments in the Measurement of Convective Heat Transfer Rates by Laser Interferometry," *International Journal of Heat and Mass Transfer,* Vol. 24, pp. 345–355.

62. Hauf, W., and Grigull, U., 1970, "Optical Methods in Heat Transfer," *Advances in Heat Transfer,* Vol. 6, pp. 133–366, Academic Press Inc., New York.

63. Tarasuk, J.D., 1968, "The Theory, Design and Operation of the University of Saskatchewan 8-Inch Mirror Mach-Zehnder Interferometer," Technical Report C-3, Mechanical Engineering Department, University of Saskatchewan.

64. Von Bistram, P., 1995, "The Design, Development and Preliminary Testing of the Ryerson Mach-Zehnder Interferometer," B.Eng. Thesis, Ryerson Polytechnic University.

65. "FEHT Finite Element Analysis", Version 7.161, F-Chart Software, 2001.

66. "SolidWorks 2003 Personal Edition," SP2.1, SolidWorks Corp., 2003.

67. Naylor, D., 2001, "Laser Interferometry," *Development in Heat Transfer Series: Measurement of Heat Flux*, Wessex Institute of Technology Press, Ashurst Southampton, U.K., Vol. 12.

68. "FIDAP Fluid Dynamics Analysis Package", Release 8.6.2, Fluent Inc., 2001.

69. Lai, B.Y. and Naylor, D., 2003, "A Numerical Study of Free Convective Heat Transfer from a Between-the-Glazing Venetian Blind Window Assembly," *Proceedings of the 19th Canadian Congress of Applied Mechanics*, pp. 384–385.

70. Oosthuizen, P.H. and Naylor, D., 1999, *Introduction to Convective Heat Transfer Analysis*, McGraw-Hill, London.

71. Zienkiewicz, O.C., 1971, *The Finite Element Method in Engineering Science,* McGraw-Hill, London.

72. Engelman, M.S., Sani, R.L., Gresho, P.M., and Bercovier, M., 1984, "Consistent vs. Reduced Quadrature Penalty Methods for Incompressible Media Using Several Old and New Elements," *International Journal of Numerical Methods for Fluids,* Vol. 2, p. 25.

73. Naylor, D., 1991, "A Numerical and Interferometric Study of Natural Convective Heat Transfer from Divided and Undivided Vertical Channels," Ph.D. Thesis, University of Western Ontario.

74. Touloukian, Y.S., Saxena, S.C., and Hestermans, P., 1975, "Viscosity: Nonmetallic Liquids and Gases," *Thermophysical Properties of Matter,* Vol. 11, Thermophysical Properties Research Center (TPRC), Purdue University, Plenum Publishing Corp.

75. Touloukian, Y.S., Liley, P.E., and Saxena, S.C., 1975, "Thermal Conductivity: Nonmetallic Liquids and Gases," *Thermophysical Properties of Matter,* Vol. 3, Thermophysical Properties Research Center (TPRC), Purdue University, Plenum Publishing Corp.

76. Touloukian, Y.S. and Makita, T., 1975, "Specific Heat: Nonmetallic Liquids and Gases," *Thermophysical Properties of Matter,* Vol. 6, Thermophysical Properties Research Center (TPRC), Purdue University, Plenum Publishing Corp.

77. Kline, S.J. and McClintock, F.A., 1953, "Describing Experimental Uncertainties in Single-Sample Experiments," *Mechanical Engineering,* Vol. 75, pp. 3–8.

78. "Maple," Release 9.03, Waterloo Maple Inc., 2003.